

Galaxy Classification in the UBC/NASA Multi-Narrowband
Survey

by

Tyron Tsui

B.Sc., The University of British Columbia, 2000

A THESIS SUBMITTED IN PARTIAL FULFILMENT OF
THE REQUIREMENTS FOR THE DEGREE OF

MASTER OF SCIENCE

in

THE FACULTY OF GRADUATE STUDIES

(Department of Physics and Astronomy)

We accept this thesis as conforming
to the required standard

THE UNIVERSITY OF BRITISH COLUMBIA

October 3, 2002

© Tyron Tsui, 2002

In presenting this thesis in partial fulfilment of the requirements for an advanced degree at the University of British Columbia, I agree that the Library shall make it freely available for reference and study. I further agree that permission for extensive copying of this thesis for scholarly purposes may be granted by the head of my department or by his or her representatives. It is understood that copying or publication of this thesis for financial gain shall not be allowed without my written permission.

Department of Physics and Astronomy

The University Of British Columbia
Vancouver, Canada

Date Oct 3/2002

Abstract

The main goals of this thesis are to classify, catalog and extract a redshift distribution of galaxies in the UBC/NASA Multi-Narrowband Survey (UNMS), conducted at the NASA Orbital Debris Observatory (NODO). We aim to classify sources using a maximum of 39 photometric bands for any source observed. Two independent classification schemes were implemented and compared. One used the photometric information from all the filters available (χ^2 fitting routine) and the other employed a neural network, which based classification on isophotal shape parameters as input (SExtractor). The classification efficiency of galaxies, based on independent confirmations were 80% and 90% for the χ^2 routine and SExtractor stellerity index respectively, even though the comparison between the two methods was poor. The fitted redshifts were compared with spectroscopically determined redshifts from the NASA/IPAC Extra-Galactic Database (NED) for 19 galaxies. More than half of the sources had seriously discrepant photometric redshifts. The spectral energy distributions (SEDs) of the galaxies with redshifts that did match showed a smooth flux distribution (low noise) that contained 1 or 2 emission features. Spectra that showed a somewhat scattered distribution of flux points resulted in uncertain redshift estimates. Failure of the photometric redshift estimation technique prevented us from pursuing more detailed statistical analyses, such as the galaxy luminosity function. We discuss possible interpretations for the apparent photometric/spectroscopic redshift discrepancy.

Contents

| | |
|---|-----|
| Abstract | ii |
| Contents | iii |
| List of Tables | v |
| List of Figures | vi |
| Acknowledgements | ix |
| 1 Introduction | 1 |
| 1.1 Liquid Mirror Telescopes | 1 |
| 1.1.1 Technological Development | 2 |
| 1.1.2 Technological Design | 4 |
| 1.2 Source Classification Methods | 7 |
| 1.2.1 Distinguishing Parameters | 8 |
| 1.2.2 Combining Parameters | 12 |
| 1.3 Galaxy Distributions | 15 |
| 1.3.1 Galaxy Luminosity Functions | 16 |
| 2 Observations and Data Reduction | 26 |
| 2.1 Telescope and Detector | 26 |
| 2.2 Drift-Scanning and Time-Delay Integration | 33 |

| | |
|--|-----------|
| 2.3 Data | 34 |
| 2.4 <i>Tdi</i> Photometry and SExtractor | 36 |
| 3 Analysis | 44 |
| 3.1 Spectral Energy Distribution Fitting | 44 |
| 3.2 Stellarity | 50 |
| 3.3 Cataloging and Final Classification | 54 |
| 4 Results and Discussion | 57 |
| 5 Conclusions and Future Work | 90 |
| Bibliography | 92 |

List of Tables

| | | |
|-----|--|----|
| 1.1 | Luminosity Function Parameters of Recent Redshift Surveys [10] . . . | 17 |
| 2.1 | Filter Specifications | 28 |
| 2.1 | Filter Specifications Continued | 29 |
| 2.1 | Filter Specifications Continued | 30 |
| 3.1 | Galaxies Used in Producing Templates | 45 |
| 3.2 | Description of Equations 3.5 and 3.6 | 54 |
| 4.1 | NED Sources with Redshift Information | 66 |
| 4.1 | NED Sources with Redshift Information Continued | 67 |

List of Figures

| | | |
|------|--|----|
| 1.1 | A schematic diagram of a LMT dish and drive system | 5 |
| 1.2 | A schematic diagram of the NODO LMT from [32] | 6 |
| 1.3 | Histograms of $\delta FWHM$ | 10 |
| 1.4 | Histogram of $m_{PSF} - m_{model}$ | 11 |
| 1.5 | Histogram of Δm | 13 |
| 1.6 | CNO2 luminosity functions | 18 |
| 1.7 | CFRS luminosity functions | 20 |
| 1.8 | LCRS luminosity functions | 21 |
| 1.9 | Galaxy redshift distribution from CNO2 data | 23 |
| 1.10 | Galaxy redshift distribution from CFRS data | 24 |
| 1.11 | Galaxy redshift distribution from LCRS data | 25 |
| 2.1 | Filter transmission curves | 31 |
| 2.2 | System throughput | 32 |
| 2.3 | Histogram of sources observed in N filters | 35 |
| 2.4 | A schematic diagram of a neural network from Firth et al. [14] | 43 |
| 3.1 | Galaxy spectral templates | 46 |
| 3.2 | Spectrum reduction | 47 |
| 3.3 | Classification efficiency | 49 |
| 3.4 | Stellar SED | 51 |

| | | |
|------|--|----|
| 3.5 | Galaxy SED | 52 |
| 3.6 | <i>Tdi</i> Image | 53 |
| 3.7 | <i>Tdi</i> image of a bright star | 56 |
| 4.1 | Histogram of $\chi_{s/g}^2$ | 58 |
| 4.2 | Ellipticity versus stellarity | 60 |
| 4.3 | m_R versus stellarity | 61 |
| 4.4 | $\chi_{s/g}^2$ versus stellarity | 62 |
| 4.5 | Confirmed galaxies plotted with $\chi_{s/g}^2$ | 64 |
| 4.6 | Confirmed galaxies plotted with stellarity | 65 |
| 4.7 | Comparison of redshifts | 68 |
| 4.8 | Redshift distribution of galaxies in the final catalog | 70 |
| 4.9 | Spectral energy distribution of NED confirmed galaxy 10831 | 71 |
| 4.10 | Spectral energy distribution of NED confirmed galaxy 11290 | 72 |
| 4.11 | Spectral energy distribution of NED confirmed galaxy 11578 | 73 |
| 4.12 | Spectral energy distribution of NED confirmed galaxy 13369 | 74 |
| 4.13 | Spectral energy distribution of NED confirmed galaxy 13511 | 75 |
| 4.14 | Spectral energy distribution of NED confirmed galaxy 14736 | 76 |
| 4.15 | Spectral energy distribution of NED confirmed galaxy 15496 | 77 |
| 4.16 | Spectral energy distribution of NED confirmed galaxy 19066 | 78 |
| 4.17 | Spectral energy distribution of NED confirmed galaxy 21916 | 79 |
| 4.18 | Spectral energy distribution of NED confirmed galaxy 29298 | 80 |
| 4.19 | Spectral energy distribution of NED confirmed galaxy 29628 | 81 |
| 4.20 | Spectral energy distribution of NED confirmed galaxy 30480 | 82 |
| 4.21 | Spectral energy distribution of NED confirmed galaxy 31711 | 83 |
| 4.22 | Spectral energy distribution of NED confirmed galaxy 58428 | 84 |

| | |
|--|----|
| 4.23 Spectral energy distribution of NED confirmed galaxy 60542 | 85 |
| 4.24 Spectral energy distribution of NED confirmed galaxy 71899 | 86 |
| 4.25 Spectral energy distribution of NED confirmed galaxy 90682 | 87 |
| 4.26 Spectral energy distribution of NED confirmed galaxy 111720 | 88 |
| 4.27 Spectral energy distribution of NED confirmed galaxy 113145 | 89 |

Acknowledgements

This work has been completed with thanks to a number of people. I would like to take this chance to thank my supervisors, Stéphane Courteau and Paul Hickson for their guidance and suggestions as well as fellow graduate students, family and friends. Stéphane's attention to detail and experience along with Paul's knowledge of the data have greatly helped my efforts in piecing this project together. After wearing out the drawing board, my final project owes to Stéphane's input and persistence.

In regards to brainstorming and quick questions, the astronomy graduate students at UBC deserve my thanks and appreciation. There are only a few things more helpful than a fresh mind on a stale problem or another person working in the office at strange hours of the night.

My gratitude also goes to my family, in particular my mother, whose love and light always guided my path and my sister who has been my life-long friend. I want to thank my closest friends, Anthony and Brandon for helping to develop my academic attributes early-on in high school and their friendship over the years. I would especially like to thank Bonnie for all her help, support and tolerance.

This research has made use of the NASA/IPAC Extra-Galactic Database (NED), which is operated by the jet propulsion laboratory, Caltech, under contract with the National Aeronautics and Space Administration and much appreciation goes to the staff supporting NED.

Chapter 1

Introduction

Surveys of the sky have always been a crucial part of astronomical research, whether the survey is of local Milky Way stars, the interstellar medium or extra-galactic sources. The goal here is to compile a catalog of galaxies from liquid mirror telescope (LMT) survey data and extract a redshift distribution. One of the main steps in analyzing astronomical images of any type and especially survey data is to confidently classify sources. While this shows to be a non-trivial task for regular pointing telescopes, the job becomes even more subtle when dealing with LMT data. The unique design and use of liquid mirror telescopes will be described first and then followed by details on a number of different source classification methods. Finally, introductory information on redshift surveys and galaxy luminosity functions will be given.

1.1 Liquid Mirror Telescopes

The implementation and technical challenges of using a spinning liquid to focus light and produce an image are intriguing in their own right, but to use a liquid mirror to achieve detailed and precise astronomical images greatly furthers the interest. The functionality of LMTs in astronomy as scientific tools has only been recently appreciated. This section introduces LMTs by first detailing the chronological path the development of LMTs has taken and then describing the current design and usage.

1.1.1 Technological Development

The concept of a liquid mirror is not a novel one; the basic principle is trivial, but the actual implementation for scientific purposes has only occurred recently. The surface shape of a spinning liquid in a gravitational field is a parabola and therefore, a spinning dish filled with a reflecting liquid could be used as the primary mirror of a telescope. This theoretically simple idea was never seriously investigated for a number of reasons that questioned its effectiveness in astronomy. While the primary concern was that the mirror is not steerable, technical difficulties added to the challenge. The speed of rotation and the leveling of the mirror have to be very strictly controlled in order keep optically degrading effects like a drifting focus, varying focal length and ripples in the reflecting liquid to a minimum. While these conditions were understood early on, pre-18th century technology was limited and simply inadequate to ensure precise operation. In 1872, Skey [41] constructed a 35-cm LMT and published the first detailed calculations of a liquid mirror telescope verifying the relationship between the angular velocity, ω , and the focal length of the telescope, f ($f = g/2\omega^2$, see [16] for a derivation). Even though Skey managed to construct and test the first LMT, astronomical implementations were still decades away due to complications with the reflecting liquid (mercury). It was not until 1909 that Wood [43] wrote a number of papers on the use of LMTs as suitable tools in astronomical research. With a 51-cm LMT, he pinpointed three major sources of ripples and image degradation, the bearing surface grinding (the bearing holds the dish containing the reflecting liquid and allows the dish to rotate), waves in the mirror caused by inaccurate leveling of the mirror and fluctuations in the angular velocity of the telescope. His precise work allowed for the first astronomical observations made with a LMT and even resolved double stars having separations as small as 2.3 arcseconds. Contrary to the momentum he

built from the success over the course of a few years, Wood abandoned liquid mirrors because he could not think of any useful application for a telescope that only points directly upwards. As many contributions to the development of LMTs as his work provided, it also marked the beginning of a 70 year void in liquid mirror research.

Seen as the one who revived the concept Borra, in 1982 [5], systematically investigated the 3 optically degrading effects originally identified by Wood. With 70 years of technological advancement, Borra was better equipped to tackle the problems. He implemented an air bearing that removed vibrations from bearing grinding, more accurately leveled the mirror and most importantly drove the dish with a synchronous motor, which provided an angular velocity constant to a few parts per million - the required stability for diffraction-limited performance. This led independent groups of researchers to further investigate the performance of a LMT [6, 17, 34]. In addition to performance tests, deep-sky imagery was obtained with the UBC-Laval 2.7-m LMT [19] and the 3-m NASA Orbital Debris Observatory (NODO) from which the data for this work have been taken.

Two future LMT projects are the 6-m Large Zenith Telescope (LZT) and the Large Aperture Mirror Array (LAMA). The LZT, constructed by Paul Hickson, is located near Vancouver, Canada and will be fully operational in 2003.

Large mirrors have even more stringent requirements on rotation stability and local wind speed. One important aspect of the telescope is the specialized air bearing. Existing bearings cannot adequately support mirrors larger than 4-m while the one designed for the LZT can support the 10 tonne load (mercury + mirror) of a 10-m LMT. While still in the planning stages, the LAMA project is an optical interferometry project with 18 10-m LMTs arranged over the area of a 60-m diameter circle, providing a 42-m effective aperture.

1.1.2 Technological Design

While the basic idea of a LMT has existed for many years, major technological challenges must be overcome. These details will now be briefly described. A more detailed account of the construction of a LMT is given by Hickson et al. [19]. These telescopes are comprised of two major components, a dish to hold the reflecting liquid and the support for the dish consisting of an air bearing and a drive system to spin the dish. The reflecting liquid used in most cases is mercury, but investigation into other, more viscous, reflecting liquids by Borra (2000) [7] is underway. A simple exploded view of the dish and drive system of a LMT is shown in Fig. 1.1.

The shape of the dish surface is made to match the required parabolic shape within 0.1 mm in order to keep the amount of mercury to a minimum. The advantage of using a minimal amount of mercury is to keep the weight of the dish plus mercury (~ 270 kg) as low as possible. The weight of the entire telescope is an important consideration as the key structural aspect is a high stiffness-to-weight ratio, allowing for more cost-efficient materials to be used and to minimize flexure and vibrations. The weight also dictates the type of motor and bearing needed to support and rotate the dish. The dish itself has an aluminum and Styrofoam core covered by a Kevlar skin, which is layered with a spin-casted polyurethane resin.

As already noted, vibrations and wobbling severely affect the optical quality of the liquid mirror, and as such, only air bearings provide the angular stiffness, low friction and precision needed to support the dish and allow for smooth rotation. The bearing sits on a three-point mount that allows the telescope to be leveled to the required precision (tenths of an arcsecond). The drive system has to be regular to 1 ppm and must not cause vibrations in the mirror. A crystal oscillator stabilizes the power supply of the DC synchronous motor in the NODO LMT to 0.01 ppm.

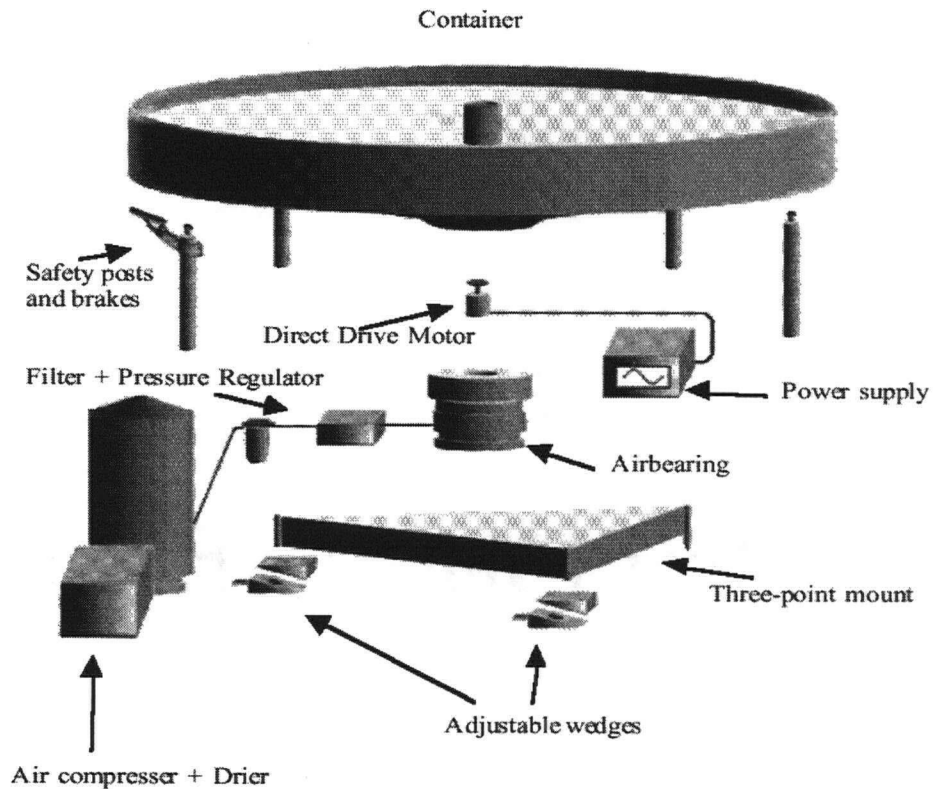


Figure 1.1 A schematic diagram of LMT dish and drive system.

The final component of the telescope is the charged coupled device (CCD) which sits atop a 5.8-m high tripod along with correcting lenses, filters, an alignment system and focusing mechanism. A more detailed figure of the complete apparatus from [32] is shown in Fig. 1.2.

As noted above the reflecting liquid is mercury where the reflectivity ranges from 70% to 80% in the optical. The hazards while working with mercury are from the fumes, but with the proper ventilation and suits in addition to the fact that a thin oxide layer forms on the surface, the evaporation is well within safety standards. The

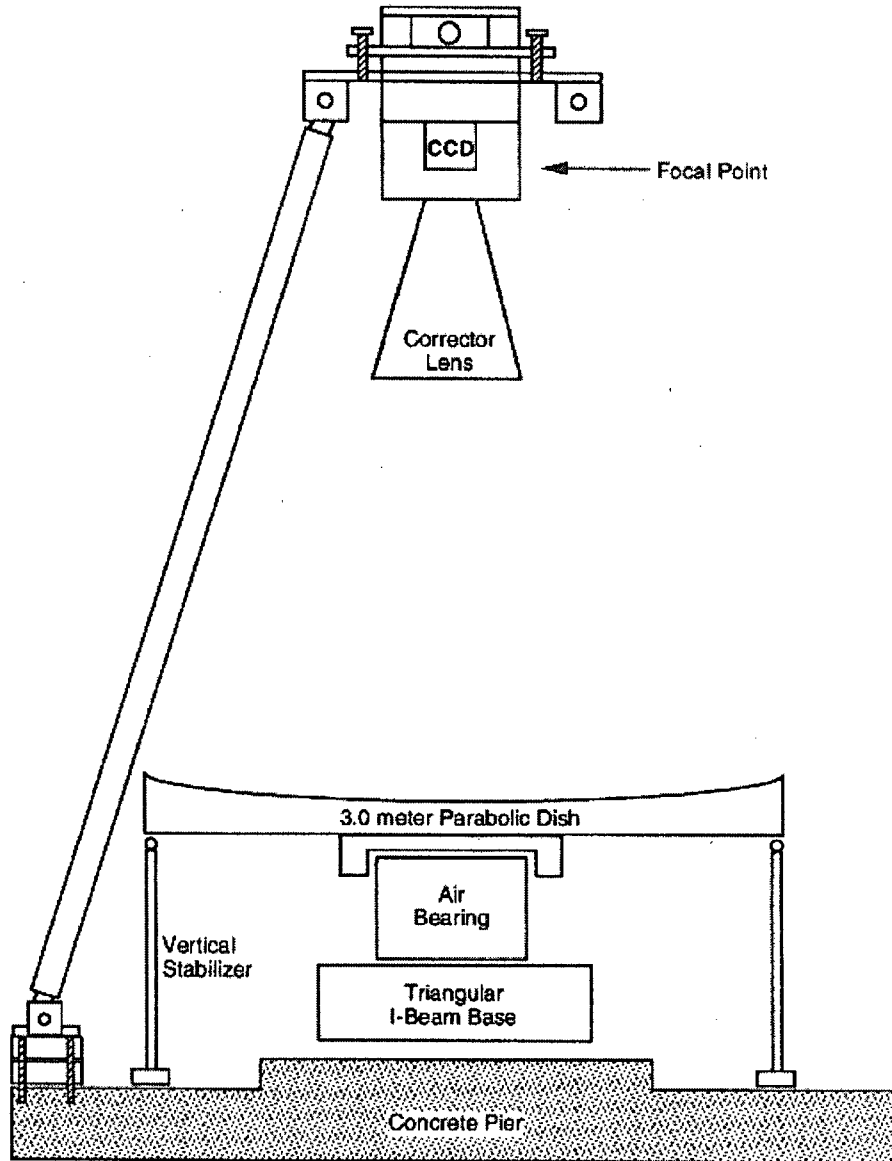


Figure 1.2 A schematic diagram of the NODO LMT from [32].

oxide layer also dampens surface waves. This is important in the real application of LMTs since the effect of wind must be considered more carefully than with conventional telescopes because the mirror is liquid. Fluctuations in the rotation period of the mirror are ~ 10 ppm when the wind is relatively calm and although the mirror is well shielded, observations are rendered useless when exterior winds exceed 12 m/s resulting in variations of order 30 ppm.

This unique design only allows for very specialized types of observations. Liquid mirrors are currently only able to point directly upwards. This results in two constraints; (i) the area of observation is severely limited to a strip of sky overhead and, (ii) sources in the area overhead cannot be tracked for extended periods of time. More recent CCD technology has allowed sources to be tracked by the CCD in the direction of motion of the sources. This mode of observation, drift-scan integration [31], will be described in more detail in §2.2.

While these limitations have hindered the development of LMTs for astronomical use, other aspects of a LMT make it ideally suited for certain fields of astronomical research. Specifically in surveys and other long-term studies where the cost of operation and maintenance hinder the extent and depth of the program, LMTs provide a simple and effective alternative. Both the construction and maintenance costs are roughly 1 to 2 orders of magnitude less than conventional telescopes.

1.2 Source Classification Methods

In surveys, an efficient, effective and automated classifying scheme is crucial as analyzing the large data sets becomes extremely time intensive. The basic eyeball classification method is not only scientifically unrobust, but in cases where the num-

ber of objects is large, this method becomes both inefficient and time consuming. Classification schemes are greatly simplified if a spectrum is available for the source, and we focus here on the less straightforward photometric classification. We first describe basic methods of using independent photometric parameters to quantifying differences between sources, then we shall explore more complex schemes where the parameters are combined to form a multi-dimensional parameter space.

1.2.1 Distinguishing Parameters

The first distinction between the images of galaxies and stars is that stars are unresolved point sources and galaxies are generally extended. Newberg et al. (1999) [33] take advantage of this property and calculate the fractional variation in the full width at half maximum (FWHM) of the image light profile, $\delta FWHM$, with Eq. 1.1; $\langle FWHM \rangle$ is the average FWHM of the sources in their sample. This value is calculated for each of their sources in a survey similar to the Sloan Digital Sky Survey (SDSS) in instrumentation and pointing, except with a smaller area of sky.

$$\delta FWHM = \frac{FWHM - \langle FWHM \rangle}{\langle FWHM \rangle} \quad (1.1)$$

Stars and stellar type objects will populate a region centred about the average FWHM whereas galaxies will form a more extended distribution. After simulating roughly 800 stars, Newberg et al. found that the distribution in $\delta FWHM$ is normal around 0 and has less than a 10% spread. If the variation is greater than 10% the source is considered extended and a galaxy. Their results are shown in Fig. 1.3. This ensures that all the stars are accounted for, but not the galaxies since they do not consider the population of galaxies that are faint and/or small that would have a $\delta FWHM$

close to 0 and hence be classified as a star.

Another distinction between stars and galaxies is a measure of the ellipticity of the source, $e = 1 - b/a$, where b is the semi-minor axis and a is the semi-major axis of the intensity distribution. All stars should have $e = 0$, and galaxies should have $0 < e < 1$ as their orientation in space is random, but there will be fewer higher ellipticity galaxies simply because it is harder to detect them.

Blanton et al. (2001) [4] classify sources in SDSS commissioning data based on the light profile of the sources in a more detailed manner. To get a proper measure of the light received from a source, a fitting routine must be implemented that fits the radial light profile of a source with a given function. This fit accounts for the light, which is below the level of noise, but is still attributed to the source. Using the fact that stellar light profiles are best fit with a Gaussian profile ($\propto e^{-x^2/\sigma^2}$) and galaxies are generally better fit by an exponential ($\propto e^{-x/x_e}$) or de Vaucouleurs profile ($\propto e^{-((x/x_e)^{1/4}-1)}$), Blanton et al. calculate the magnitudes using a point spread function (PSF) weighted aperture and the magnitude associated with the best fitting model (exponential or de Vaucouleurs) to the galaxy profile. The difference of the two magnitudes are computed and if most of the object's light is contained within an aperture weighted by the PSF, it is considered stellar. This method is tested with spectroscopically-confirmed galaxies and it was found that 1% of galaxies brighter than $m_R = 17.6$ are misclassified. Fig. 1.4 shows the distribution of stars and galaxies with their magnitude difference index.

The above method was not used because the software was not available, but a similar approach was investigated and was found to be inadequate for this data as shown in Fig. 1.5. The UBC-NASA Multi-band Survey (UNMS1) catalog [21] is the first catalog produced from data used in this thesis. The catalog provides total

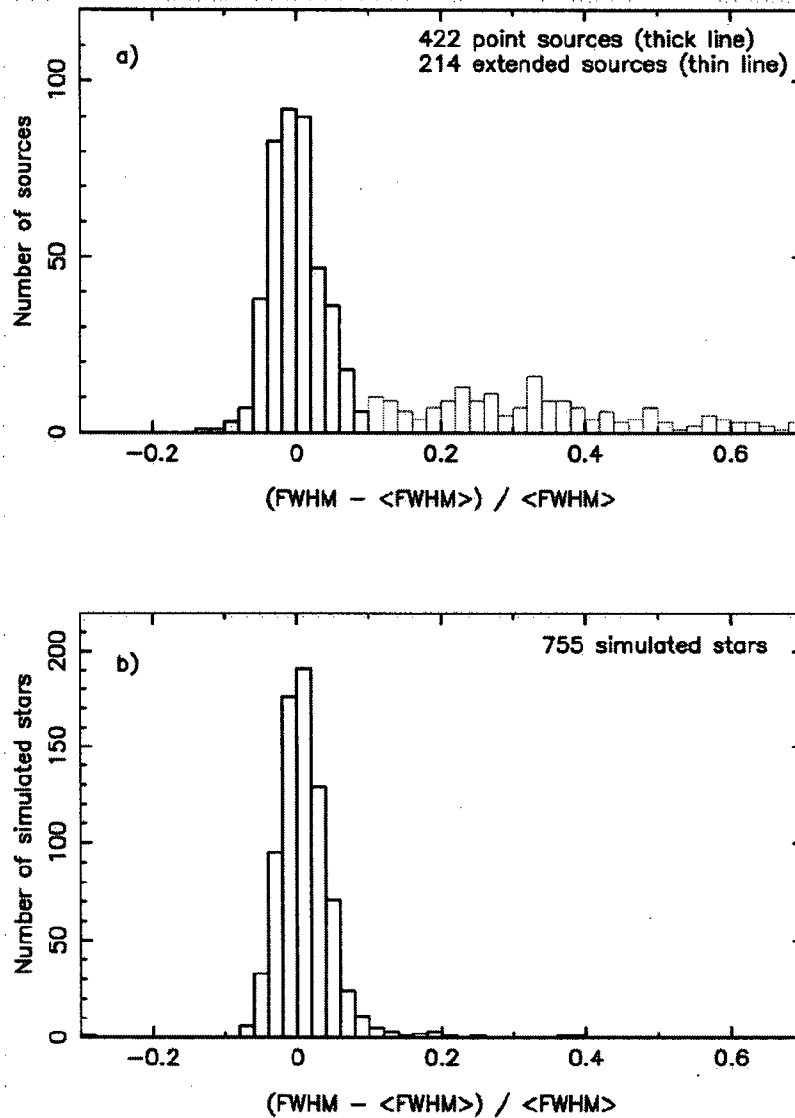


Figure 1.3 Histograms of $\delta FWHM$ from Newberg et al. (1999) [33]. The top figure shows the distribution of sources and the bottom figure shows the distribution of simulated data. The normal distribution of the point sources is apparent.

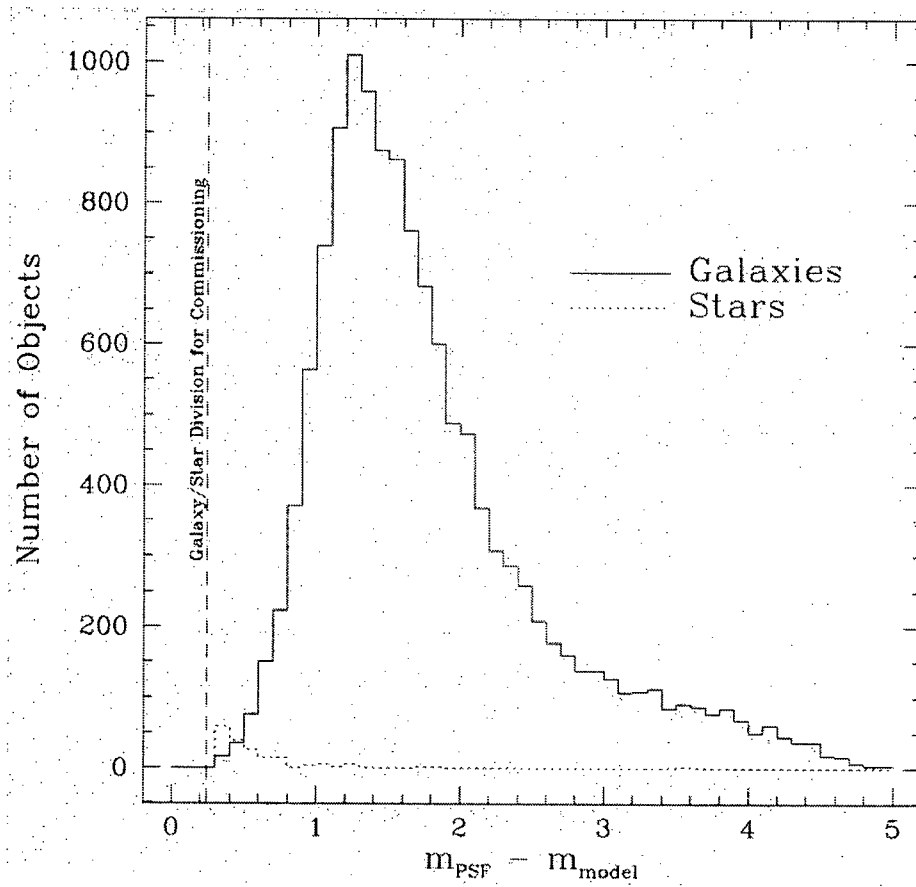


Figure 1.4 Histogram of $m_{\text{PSF}} - m_{\text{model}}$ from Blanton et al. (2001) [4] showing the distribution of galaxies in SDSS commissioning data and the spectroscopically confirmed stars.

magnitudes for sources derived by fitting Gaussian profiles to each of the sources. The data were reduced a second time to obtain total magnitudes by fitting an exponential profile to all of the sources. The magnitude difference for a given source provided a quantitative scheme similar to the one by Blanton et al. [4]. Fig. 1.5 shows a histogram of the magnitude differences where ellipticity information was used as well. The dotted curve contains sources with $e \geq 0.1$ and the dashed curve shows sources with $e < 0.1$. The bimodal distribution is evident, but misclassification is highly possible. Using Eq. 1.2, Δm is expected to be 0 for stars and significantly greater than 0 for galaxies.

$$\Delta m = m_{exp} - m_{gaussian} \quad (1.2)$$

This is because the more focused light of a stellar profile will be more easily fit by both functions and provide similar total magnitudes where as the light profile of a galaxy is only well fit by an exponential or de Vaucouleurs profile and therefore the difference between the two fits will be large.

1.2.2 Combining Parameters

Considering galaxies that are dimmer and more distant, these become progressively less resolved and appear to the eye almost indistinguishable from stars. In addition, most Quasi-Stellar Objects (QSOs), faint BL Lacertae objects and Seyfert galaxies are objects that have little or no apparent nebulosity and thus are stellar-like in appearance [23]. In attempts to correctly classify faint sources, more robust and detailed methods are needed. One such approach is to use as many independent parameters as possible to establish an n-dimensional parameter space. The parameters described above (ellipticity, $\delta FWHM$, Δm) are just a few that can be combined to form such a parameter space. Operationally, this is what galaxy-star separation is reduced

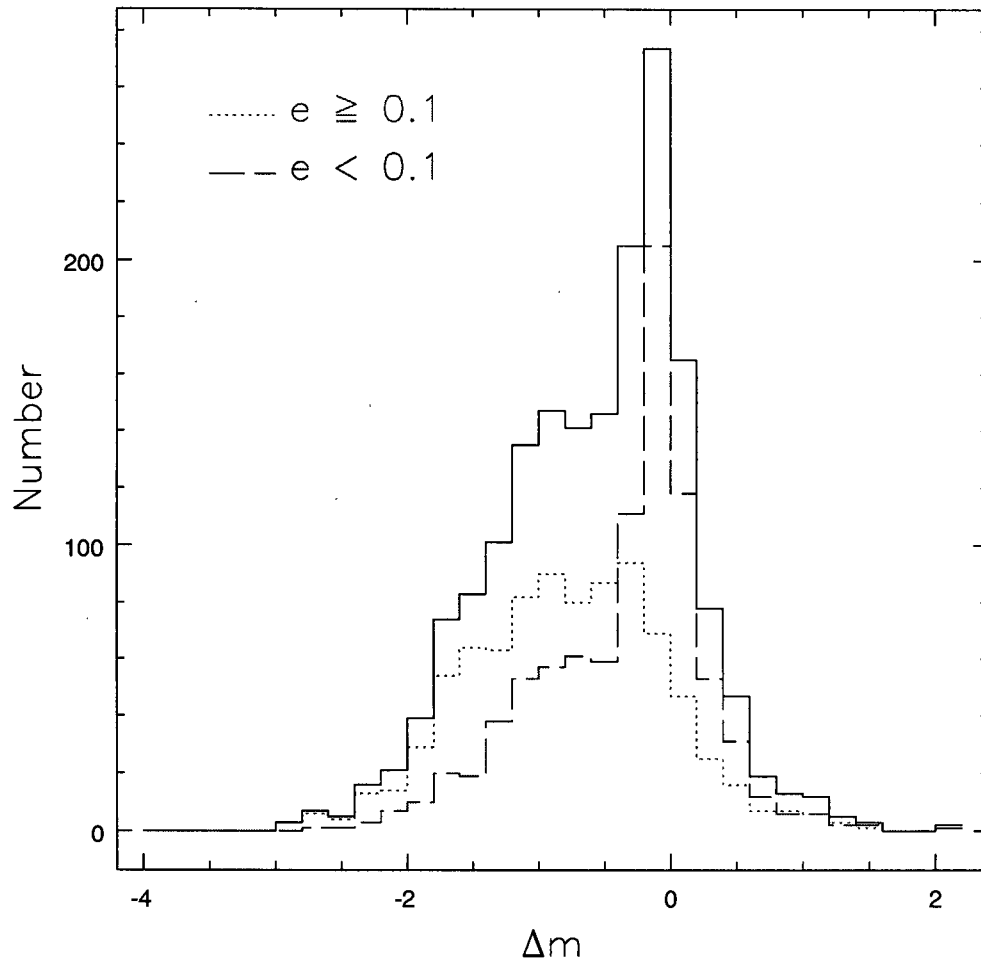


Figure 1.5 Histogram of Δm showing the distribution of sources in the UNMS1 survey (solid). Sources with an ellipticity greater than or equal to 0.1 are shown by the dotted histogram and those with ellipticity less than 0.1 are shown by the dashed histogram.

to - finding a hyper-surface in n-dimensional parameter space that will confidently distinguish sources.

Postman et al. (1996) [38] used this idea to classify sources in their distant cluster survey. They use a parameterization, which depends on the observed PSF, position of the source on the image, magnitude, effective radius of the light profile, and peak intensity. Each object is classified based upon the results of fitting a series of templates. An improvement over straightforward template fitting methods is the use of neural networks to apply these templates. Neural networks will be described in greater detail in the next chapter. For now, let us mention that the network is trained to recognize certain patterns and groupings in a given parameter space, interpolates between points and provides an output based upon the training set used. Odewahn et al. (1993) [35] conducted a two-colour survey of nine Palomar Sky Survey fields centred on the North Galactic Pole using the Minnesota Automated Plate Scanner. The input parameters used for their neural network are an average surface brightness within some isophotal level, diameter of the source, the RMS error in the diameter determination, the error in the Y-centroid determination and an index that quantifies the presence of diffraction spikes. They found that their neural network was at least 90% accurate down to $m_B = 20.0$.

While these methods rely on broadband photometric information when spectroscopy is unavailable or not yet acquired, our database is unique because of the narrowband photometry that resembles low-resolution spectroscopy. Cabanac et al. (2002) [10] have recently considered principal component analysis (PCA) to classify sources in this type of data. PCA assumes that a linear relation exists between all variables and corresponds to a simple rotation of the axes within the multi-dimensional space to a system where the new axes are orthogonal and aligned with the directions

of maximal variance. While they have yet to implement their technique to actual data, their simulations clearly show that it is an effective method. Their analysis considers the maximum amount of information available in a survey similar to ours. While 39 photometric bands of data are available, Cabanac et al. show that not all of them are required. In their simulations, 10 bands of information which are the first 10 eigencomponents of the Karhunen-Loève expansion, was sufficient to classify sources and estimate redshifts. With simulated data and a median signal-to-noise (S/N) ratio of 6, 98% of stars, 100% of galaxies and 93% of QSOs are correctly classified.

1.3 Galaxy Distributions

Galaxies are seen as the building blocks of the Universe, and as such, the study of their properties as well as their distribution through space is fundamental in understanding the structure of the Universe. There are a number of ways to describe the distribution of galaxies in space (number density, surface density, redshift distributions, etc.). The galaxy luminosity function, basically the number density of galaxies per unit luminosity interval, is the primary descriptor of galaxy distribution as it offers great insight into galaxy evolution and formation. A slightly dated, but thorough review of galaxy luminosity functions is provided by Bingelli et al. (1988) [2]. This section will briefly outline the current understanding of galaxy distributions, namely luminosity functions.

1.3.1 Galaxy Luminosity Functions

If we let $v(M, x, y, z)$ be the number of galaxies in a unit volume dV at (x, y, z) with absolute magnitudes between M and $M + dM$,

$$v(M, x, y, z)dM dV = \phi(M)D(x, y, z)dM dV \quad (1.3)$$

where

$$\int_{-\infty}^{+\infty} \phi(M)dM = 1 \quad (1.4)$$

$\phi(M)$ is the luminosity function and gives the fraction of galaxies per unit magnitude with absolute magnitudes in the interval $(M, M + dM)$. $D(x, y, z)$ is the density function and gives the number of galaxies per unit volume.

The luminosity function does not simply describe all galaxies and considerations must be made for morphological type and evolution. Determining the galaxy luminosity function would ideally involve observing all galaxies, but just as with most statistical measures, a sufficiently large sample should adequately describe the whole population. In the case of galaxies, luminosity functions vary with morphological type and evolve with redshift. Because of this, a proper study of galaxy luminosity functions requires a sample that includes several morphological types at a number of redshift intervals resulting in samples of $\sim 10^3 - 10^4$. Table 1.1 gives galaxy properties for three major redshift surveys compiled by Cabanac et al. (2002) [10]. The parameters provided in that table pertain to the Schechter parameterization [40] of the galaxy luminosity function given by the following,

$$\phi(M)dM = 0.4 \ln 10 \phi^* 10^{-0.4(M^*-M)(\alpha+1)}dM \times \exp(-10^{0.4(M^*-M)}) \quad (1.5)$$

Table 1.1. Luminosity Function Parameters of Recent Redshift Surveys [10]

| Survey | Limits (z) | N | $M_{R_c}^* - 5 \log h$ | α | ϕ^{*a} |
|--------------------|----------------|-------|------------------------|------------------|-------------|
| CNOC2 [29] | | | | | |
| (Earlier than Sbc) | 0.1 ~ 0.6 | 1128 | -20.61 ± 0.11 | -0.44 ± 0.10 | 0.023 |
| (Later than Sbc) | 0.1 ~ 0.6 | 1012 | -20.11 ± 0.18 | -1.34 ± 0.12 | 0.006 |
| CFRS [28] | | | | | |
| (Redder than Sbc) | 0.2 ~ 1.0 | 99 | -20.12 ± 0.25 | 0.00 | 0.030 |
| (Bluer than Sbc) | 0.2 ~ 1.0 | 110 | -20.01 ± 0.25 | -1.34 | 0.010 |
| LCRS [9] | | | | | |
| (Early type) | 0 ~ 0.2 | 16146 | -20.42 ± 0.02 | -0.13 ± 0.05 | 0.018 |
| (Late type) | 0 ~ 0.2 | 2132 | -20.38 ± 0.08 | -1.58 ± 0.07 | 0.002 |

^aErrors in ϕ^* are typically of order 0.005

where ϕ^* , M^* and α are the Schechter parameters. Figs. 1.6, 1.7 and 1.8 show the respective luminosity functions given in Table 1.1.

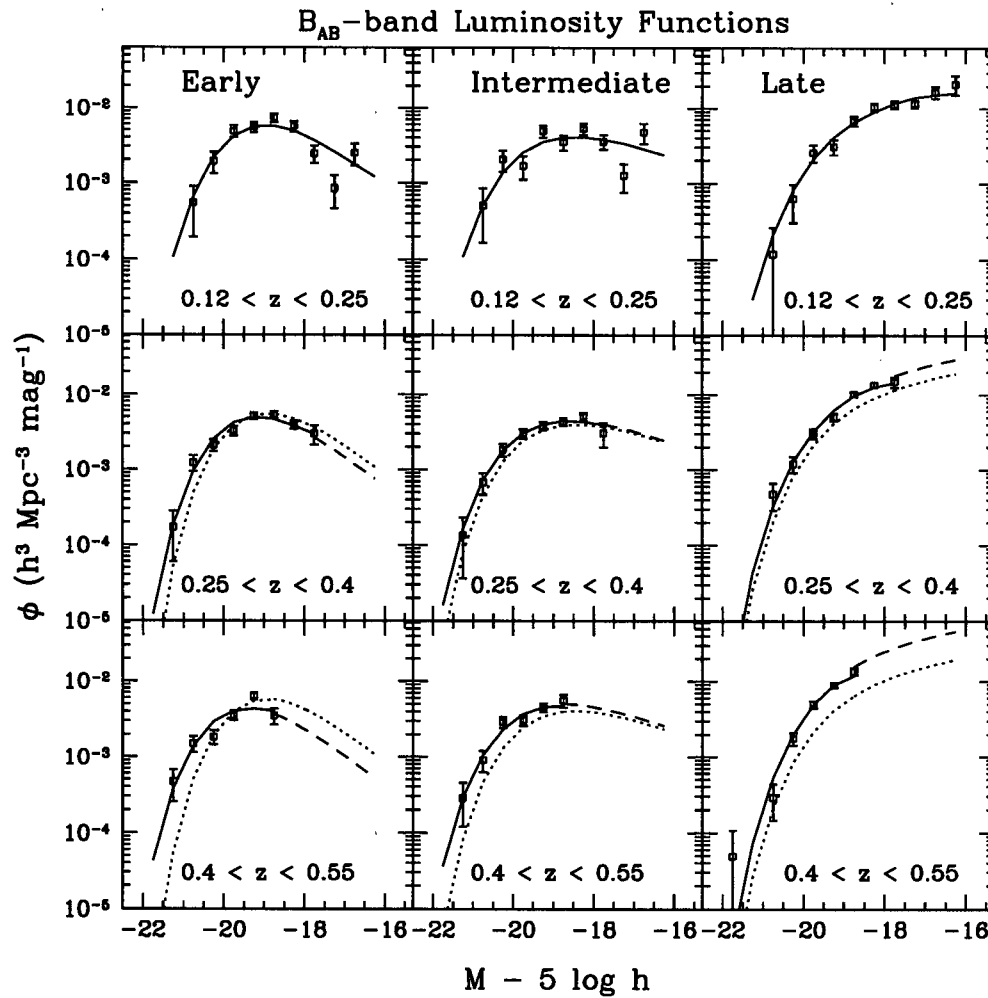


Figure 1.6 CNOC2 luminosity functions. B_{AB} -band luminosity functions. The solid curves show the best-fit parametric evolving models. Also shown are fiducial luminosity functions (dotted curves) from the lowest-redshift bin for each galaxy type.

The CNOC2 survey [29] divides galaxies into two classes, early+intermediate class and late class. The classification scheme is based on a least-squares fit of the spectral energy distributions [11]. Lilly et al. (1995) [28] separate the CFRS sample into those red galaxies having rest-frame $[U - V]_{AB} = 1.38$ and a blue population consisting of the remaining galaxies. The LCRS survey [9] classified sources by a PCA into 6 groups called clans, where roughly clans 1+2+3+4 are early-type galaxies and clans 5+6 are the late-type. The Schechter parameters agree well and all the luminosity functions show the same basic trend. At the bright end early-type galaxies (ellipticals and large spirals) dominate, but as one approaches the faint end, the number of late-type galaxies increase.

This increase in the luminosity function also shows limitations at the faint end of the luminosity function. The major contribution at these low magnitudes is low surface brightness (LSB) galaxies. The central surface brightness of a galaxy operationally characterizes it as a LSB or high surface brightness (HSB) galaxy, whether it is lower or higher than 23 B-mag/arcsec² respectively. Dalcanton et al. (1997) [12] calculated the number density of LSBs in the sample to be $\mathcal{N} = 0.01_{-0.005}^{+0.006}$ galaxies/Mpc³, roughly 2 times that of HSBs. The measurement of the absolute number density of LSBs probably represents a lower limit, due to very strong biases against LSBs with bulges or edge-on LSBs in their sample. Binggeli et al. (1990) [3] used deep Palomar plates to catalog several hundred dwarf LSBs and Davies et al. (1988) [13] and Bothun et al. (1991) [8] found new samples of extreme LSBs in Virgo and Fornax. The large Automated Plate Measuring machine (APM) LSB survey [42] selected LSBs both automatically and by eye using scanned plates from the APM galaxy survey [22]. Impey et al. (1996) [22] identified 693 galaxies that covered 786 square degrees. It is clear that a large fraction of the galaxy population lies at the faint-end and further

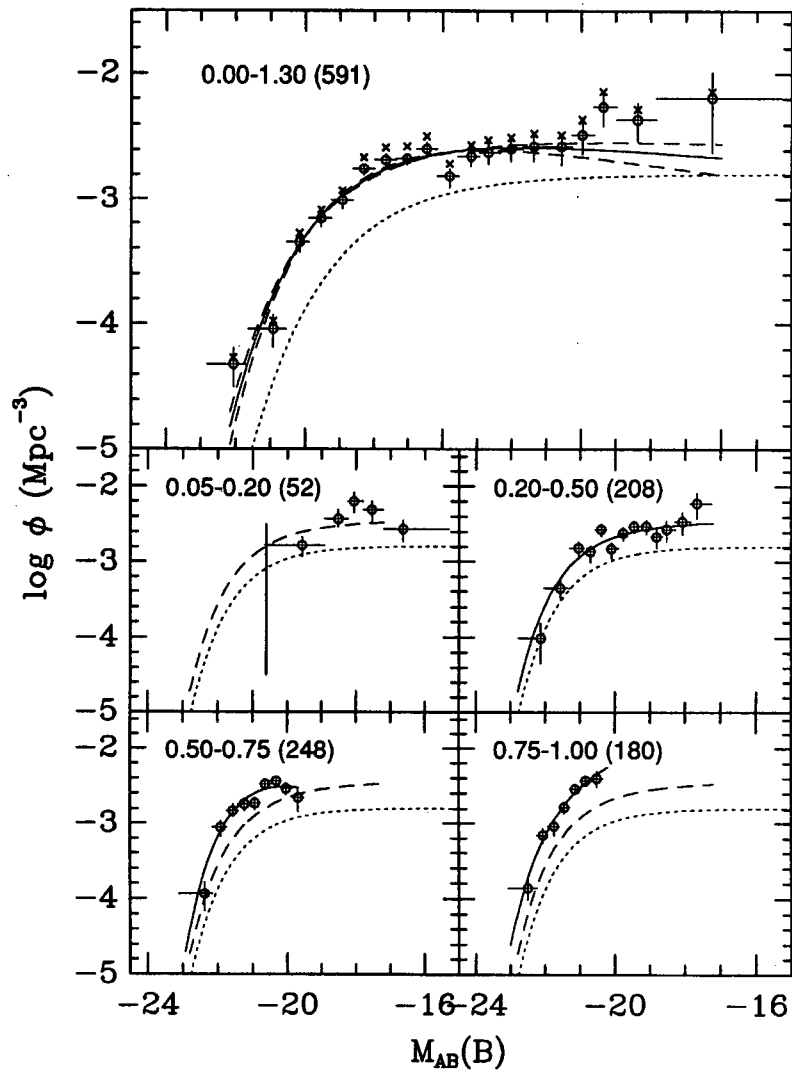


Figure 1.7 CFRS luminosity functions. The numbers in the top left of each panel give the redshift range of the sources and in parentheses the number of sources. The top panel is the combined general luminosity function of the bottom 4 panels. The solid and dashed curves show fitted Schechter functions (best fit and 1σ) and the dotted curves is a comparison luminosity function from The Stromlo-APM Redshift Survey [30].

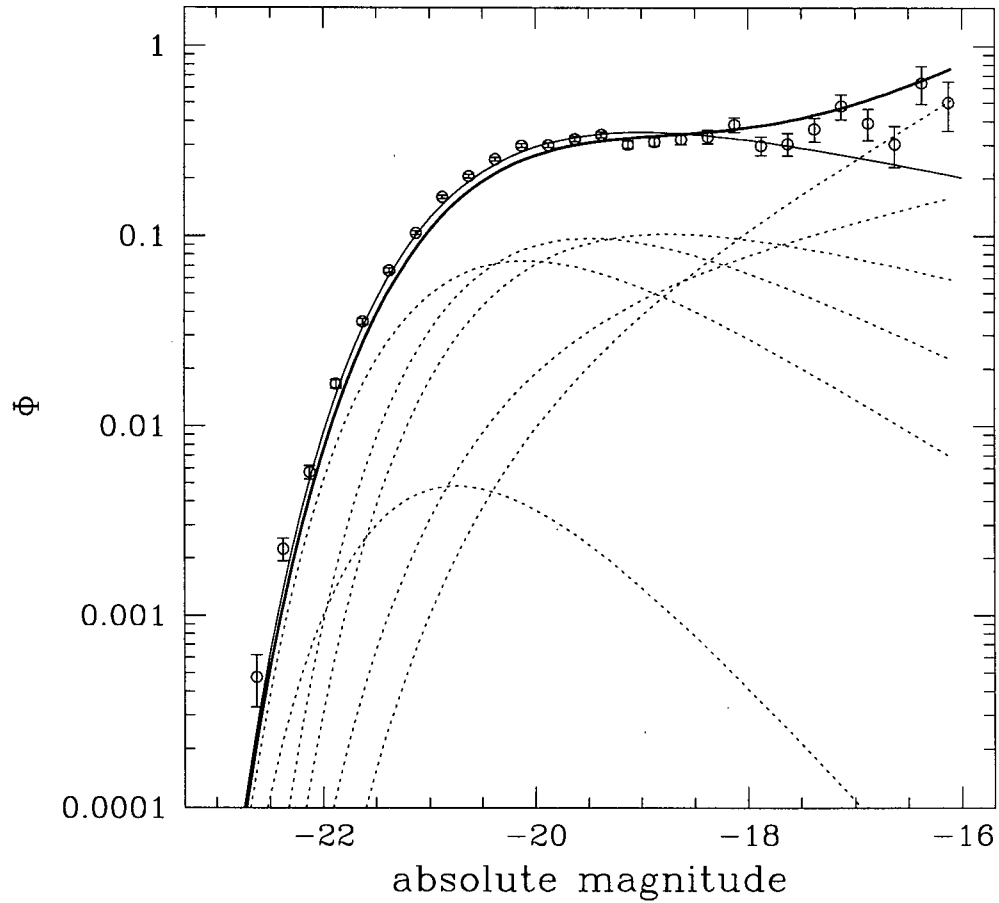


Figure 1.8 LCRS luminosity functions. The points give the luminosity function from the non-parametric fit for the full catalog and the light solid curve is the Schechter function fit to the data. The dotted lines are 6 spectra classes where the two groups with a positive faint-end slope are late-type galaxies and the other 4 are early-type galaxies. The heavy solid curve is the sum of the grouped luminosity functions.

surveys that will help constrain the tail of the luminosity function will deepen the understanding of the formation and evolution of all galaxies.

Another useful method of displaying the distribution of galaxies is a redshift histogram. Figs. 1.9, 1.10, and 1.11 from [10] show for each previous survey, the redshift distributions calculated from the Schechter parameters given in Table 1.1. The thin and thick lines show effect of evolution of the population on the luminosity function. Thin lines represent calculated distributions without evolution and the thick lines show the distribution with evolution. The peak of the late-type distribution is at smaller redshift than the early-type distribution because of the combination of fainter M^* and steeper slope α . This effect remains when evolution of the populations is introduced. The distributions are calculated in the case of a flat Universe with $\Lambda = 0$ and $H_0 = 100h \text{ km s}^{-1} \text{ Mpc}^{-1}$, over 40 deg^2 .

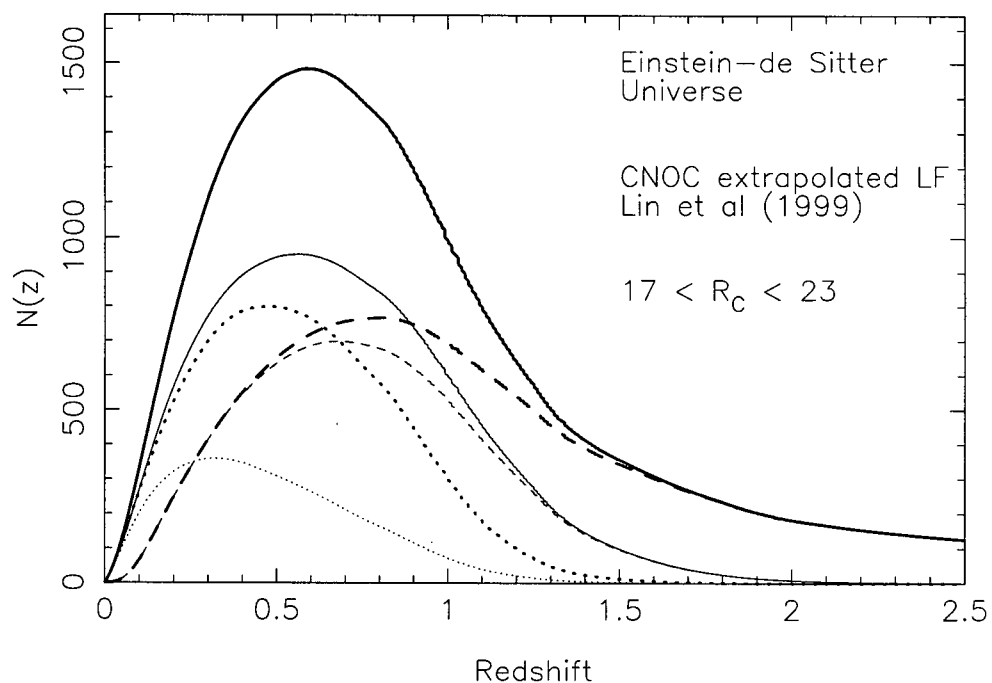


Figure 1.9 Galaxy redshift distribution from CNOC2 data. Cabanac et al. [10] provide a simulated galaxy redshift distribution in 40 deg^2 of the sky to $17 \leq R_c \leq 23$ in an Einstein-de Sitter Universe. The thin lines show the non-evolving distributions and the thick lines show the evolving distributions. The solid lines show the total distribution while the dotted lines show the distribution for late-type galaxies and the dashed lines for early+intermediate galaxies for the CNOC2 sample.

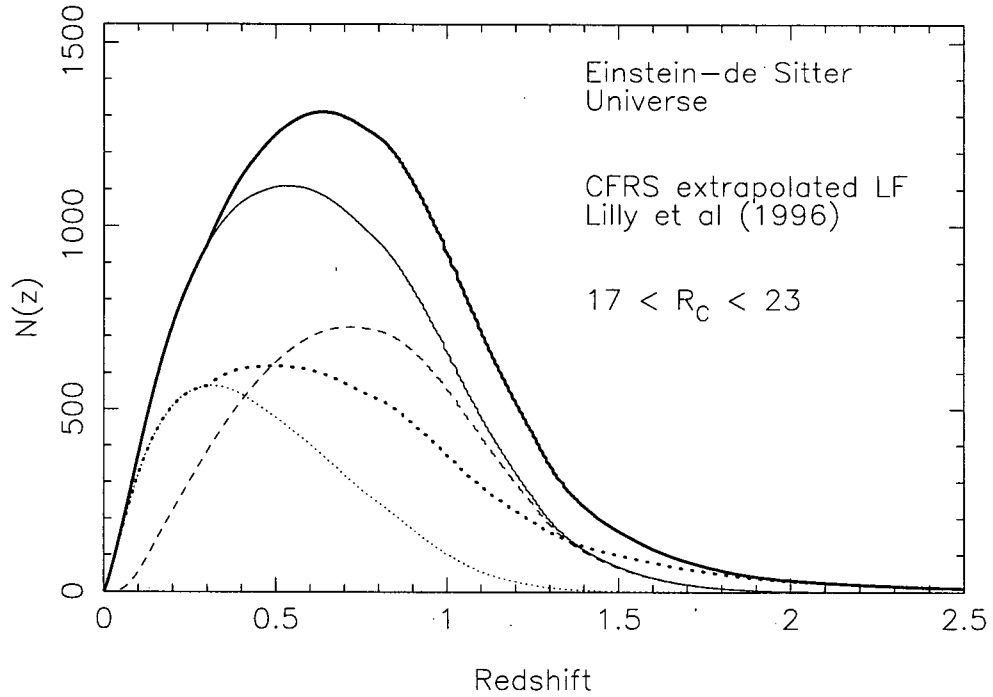


Figure 1.10 Galaxy redshift distribution from CFRS data. Cabanac et al. [10] provide a simulated galaxy redshift distribution in 40 deg^2 of the sky to $17 \leq R_c \leq 23$ in an Einstein-de Sitter Universe. The non-evolving distribution of red galaxies is shown by the thin dashed line and distribution of blue galaxies is given by the thin dotted line. The thick dotted line shows the evolving distribution for blue galaxies. The thin solid line shows the total non-evolving distribution and the thick solid line shows an evolving distribution for the CFRS sample.

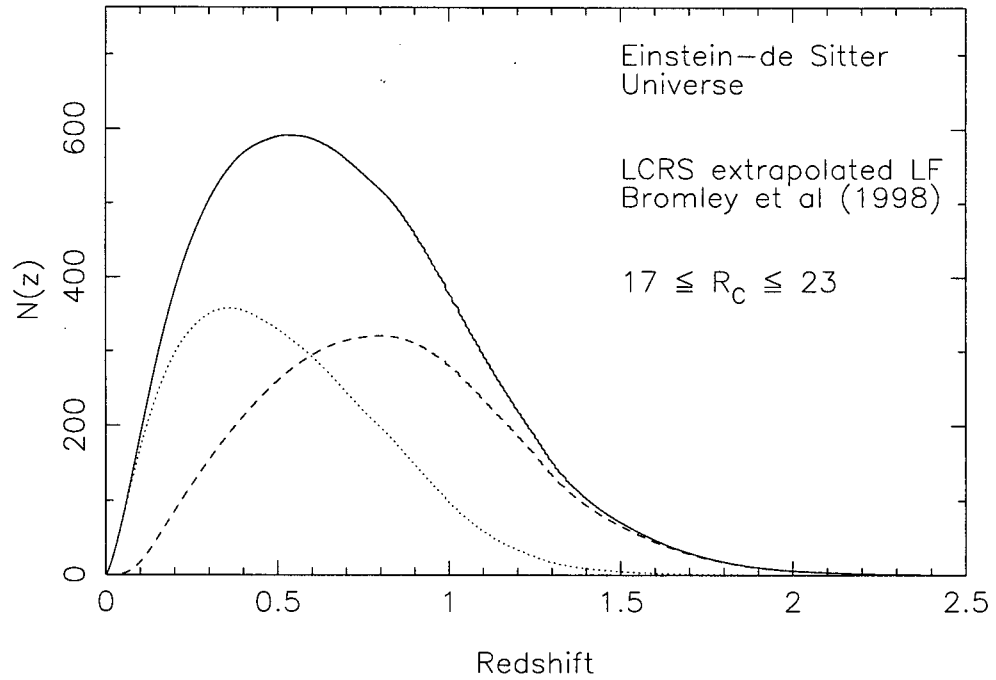


Figure 1.11 Galaxy redshift distribution from LCRS data. Cabanac et al. [10] provide a simulated galaxy redshift distribution in 40 deg^2 of the sky to $17 \leq R_c \leq 23$ in an Einstein-de Sitter Universe. The distribution of early-type galaxies is shown by the dashed line and distribution of late-type galaxies is given by the dotted line. The solid line shows the total distribution for the LCRS sample.

Chapter 2

Observations and Data Reduction

The general concept of a liquid mirror telescope and the method of data acquisition were reviewed in the previous section. Now the specifics of the LMT used in this work will be described as well as the data and reduction programs used.

2.1 Telescope and Detector

All of the data were collected with the LMT at the NASA Orbital Debris Observatory near Cloudcroft, New Mexico. The telescope site is dry and at $105^{\circ} 43' 59''$ West longitude, $32^{\circ} 58' 43.5''$ North latitude and an altitude of 2772-m. Seeing at this site is typically 1.4 arcseconds. The observatory's primary function was to track space debris. This is most efficiently accomplished roughly an hour after the sun has set or before the sun rises as the reflected light off the debris reaches a maximum at those times. This allows for the exclusive use of the telescope for astronomical observations at the darkest times of the night.

The telescope's mirror is 3-m parabolic dish covered by a 1.8-mm layer of liquid mercury and has a 4.5-m focal length. Off-axis aberrations are removed by a three-element optical corrector lens located near the prime focus. Since the mirror points directly upward and the ability of the telescope to track objects is severely limited, the images are acquired by time-delay integration or drift-scan mode. The charges in each of the pixels along a column of the CCD are shifted to the next pixel in the direction

opposite of rotation of the earth and at the sidereal rate. This provides an effective integration of each source equal to the time taken to cross the CCD. Hickson's *Tdi* software provides interactive control of data-acquisition parameters and a continuous display of image data. The software will be described in greater detail in the next chapter.

The detector used for survey observations in the 1996 and 1997 observing seasons is a thick, front-illuminated, 2048×2048 pixel Loral CCD. The pixels are $15\text{-}\mu\text{m}$ on a side, which gives an image scale of 0.598 arcseconds/pixel. The effective integration time or the transit time of the object across the CCD is 97.0s . The CCD sits in a thermo-electrically-cooled Dewar that keeps the operating temperature of the CCD at -30° Celsius. The camera used in 1999 and 2000 is a thin 1048×1048 pixel SITE CCD with $24\text{-}\mu\text{m}$ pixels corresponding to 0.96 arcsecond/pixel and is more sensitive than the original Loral CCD. The integration time for sources observed with the newer CCD is 78.0s . The original CCD was designed for high-speed operation necessary for debris tracking and therefore suffered from high read noise, $28e^-$, while the newer CCD has a lower read noise, $11e^-$.

The resulting image from a night's observation is a long narrow strip of sky. To ensure uniformity in an observation only one filter of 39 is typically used for the entire night. The filters have central wavelengths at a uniform logarithmic spacing of 0.01 , constant bandwidth of 0.02 in $\log \lambda$ and span the range $455 - 948$ nm. As shown in Table 2.1 the individual filter bandwidths increase in proportion to the central wavelength, and are set at twice the sampling interval in order to prevent aliasing effects when observing emission-line objects. The respective transmission curves are shown in Fig. 2.1. The total system throughput (Fig. 2.2) is 18% between 650 and 800nm determined from the observed flux of standard stars.

Table 2.1. Filter Specifications

| Filter ID | λ^a | $\Delta\lambda^b$ | $\log(\nu)^c$ | $\Delta\log(\nu)^d$ | t^e | W^f |
|-----------|-------------|-------------------|---------------|---------------------|-------|-------|
| I | 959.0 | 327.5 | 14.4950 | 0.148 | 0.509 | 166.7 |
| R | 700.0 | 193.0 | 14.6317 | 0.120 | 0.758 | 146.3 |
| V | 557.5 | 104.8 | 14.7306 | 0.081 | 0.522 | 54.70 |
| B | 420.5 | 115.4 | 14.8531 | 0.119 | 0.541 | 62.45 |
| 990 | 990.5 | 42.19 | 14.4810 | 0.018 | 0.930 | 39.24 |
| 965 | 965.0 | 43.22 | 14.4923 | 0.019 | 0.906 | 39.16 |
| 948 | 947.7 | 39.08 | 14.5003 | 0.019 | 0.933 | 36.43 |
| 925 | 924.5 | 40.04 | 14.5111 | 0.019 | 0.928 | 36.96 |
| 906 | 906.3 | 35.32 | 14.5198 | 0.018 | 0.900 | 31.71 |
| 883 | 883.1 | 41.28 | 14.5311 | 0.021 | 0.924 | 38.10 |
| 868 | 867.9 | 35.10 | 14.5388 | 0.018 | 0.952 | 33.38 |
| 844 | 843.8 | 35.58 | 14.5509 | 0.019 | 0.932 | 33.09 |
| 825 | 824.8 | 33.67 | 14.5608 | 0.018 | 0.950 | 31.96 |
| 806 | 805.9 | 34.62 | 14.5709 | 0.019 | 0.936 | 32.27 |
| 788 | 787.5 | 33.31 | 14.5809 | 0.019 | 0.927 | 30.85 |
| 770 | 769.6 | 31.86 | 14.5910 | 0.018 | 0.937 | 29.79 |

Note. — continued on next page

Table 2.1. Filter Specifications Continued

| Filter ID | λ^a | $\Delta\lambda^b$ | $\log(\nu)^c$ | $\Delta\log(\nu)^d$ | t^e | W^f |
|-----------|-------------|-------------------|---------------|---------------------|-------|-------|
| 752 | 752.4 | 33.25 | 14.6008 | 0.019 | 0.955 | 31.72 |
| 735 | 734.7 | 32.17 | 14.6111 | 0.019 | 0.940 | 30.17 |
| 719 | 718.7 | 30.54 | 14.6208 | 0.019 | 0.954 | 29.13 |
| 704 | 704.4 | 29.88 | 14.6293 | 0.019 | 0.930 | 27.78 |
| 688 | 688.0 | 29.20 | 14.6397 | 0.019 | 0.936 | 27.30 |
| 671 | 671.3 | 29.08 | 14.6503 | 0.019 | 0.933 | 27.10 |
| 655 | 654.6 | 27.99 | 14.6612 | 0.019 | 0.930 | 26.03 |
| 641 | 641.1 | 23.98 | 14.6705 | 0.016 | 0.919 | 21.99 |
| 629 | 628.7 | 26.39 | 14.6789 | 0.018 | 0.952 | 25.10 |
| 614 | 613.7 | 23.62 | 14.6893 | 0.018 | 0.910 | 21.45 |
| 598 | 597.6 | 24.31 | 14.7010 | 0.018 | 0.717 | 17.41 |
| 586 | 585.6 | 23.10 | 14.7099 | 0.018 | 0.720 | 16.63 |
| 571 | 571.1 | 21.71 | 14.7207 | 0.017 | 0.750 | 16.26 |
| 556 | 556.4 | 53.97 | 14.7303 | 0.042 | 0.697 | 37.62 |
| 545 | 545.1 | 21.00 | 14.7409 | 0.017 | 0.726 | 15.22 |
| 533 | 532.7 | 22.76 | 14.7505 | 0.019 | 0.730 | 16.59 |

Note. — continued on next page

Table 2.1. Filter Specifications Continued

| Filter ID | λ^a | $\Delta\lambda^b$ | $\log(\nu)^c$ | $\Delta\log(\nu)^d$ | t^e | W^f |
|-----------|-------------|-------------------|---------------|---------------------|-------|-------|
| 519 | 519.0 | 22.72 | 14.7609 | 0.022 | 0.679 | 15.38 |
| 510 | 510.2 | 22.36 | 14.7698 | 0.019 | 0.689 | 15.39 |
| 498 | 498.1 | 21.91 | 14.7798 | 0.019 | 0.670 | 14.66 |
| 486 | 486.0 | 20.22 | 14.7904 | 0.019 | 0.752 | 15.18 |
| 476 | 475.6 | 19.30 | 14.7998 | 0.018 | 0.690 | 13.31 |
| 466 | 465.9 | 18.48 | 14.8090 | 0.018 | 0.673 | 12.42 |
| 455 | 454.5 | 17.67 | 14.8196 | 0.018 | 0.632 | 11.17 |

^aMean Wavelength (nm)

^bBandwidth (nm): W/t

^clog of central frequency (Hz)

^dlog of $\Delta\nu$: $0.434 \times \text{bandwidth}/\text{mean wavelength}$

^eCentral transmission

^fEquivalent width (nm)

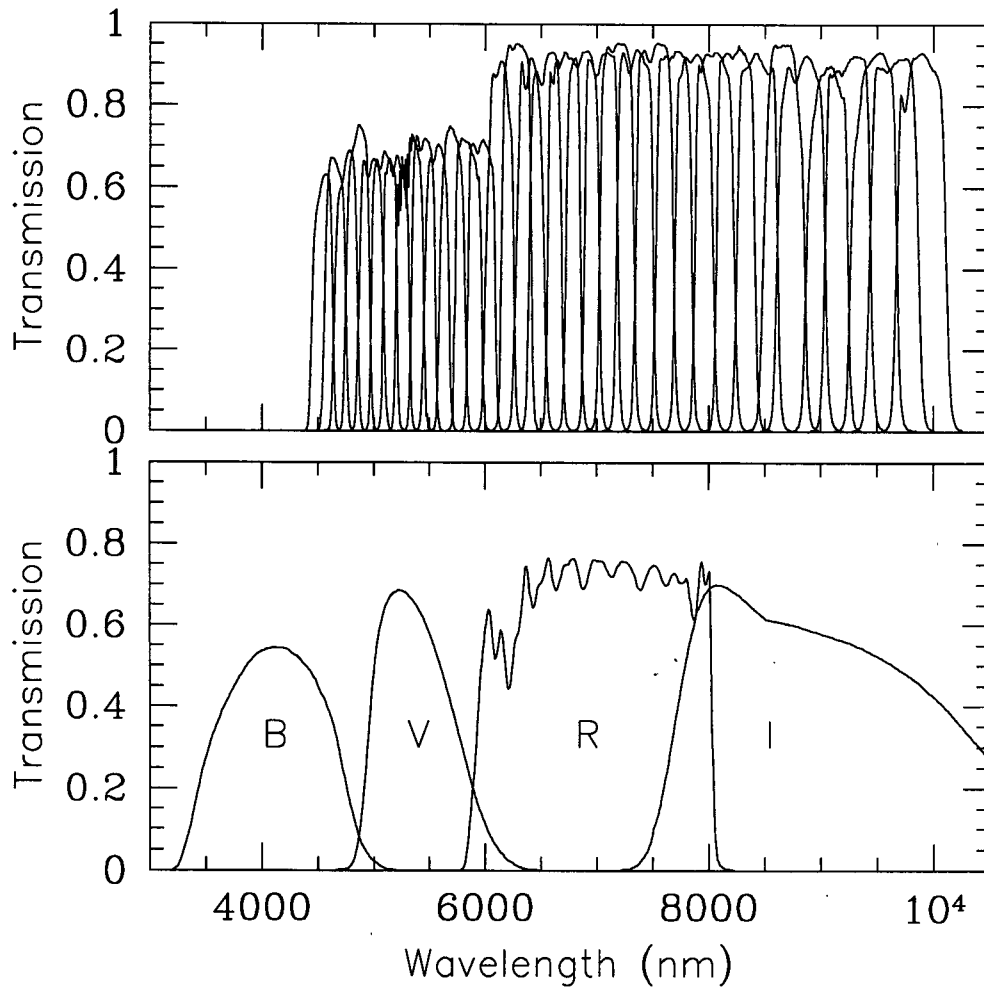


Figure 2.1 Filter transmission curves. The top panel shows the narrowband filters and the bottom shows the broadband filters.

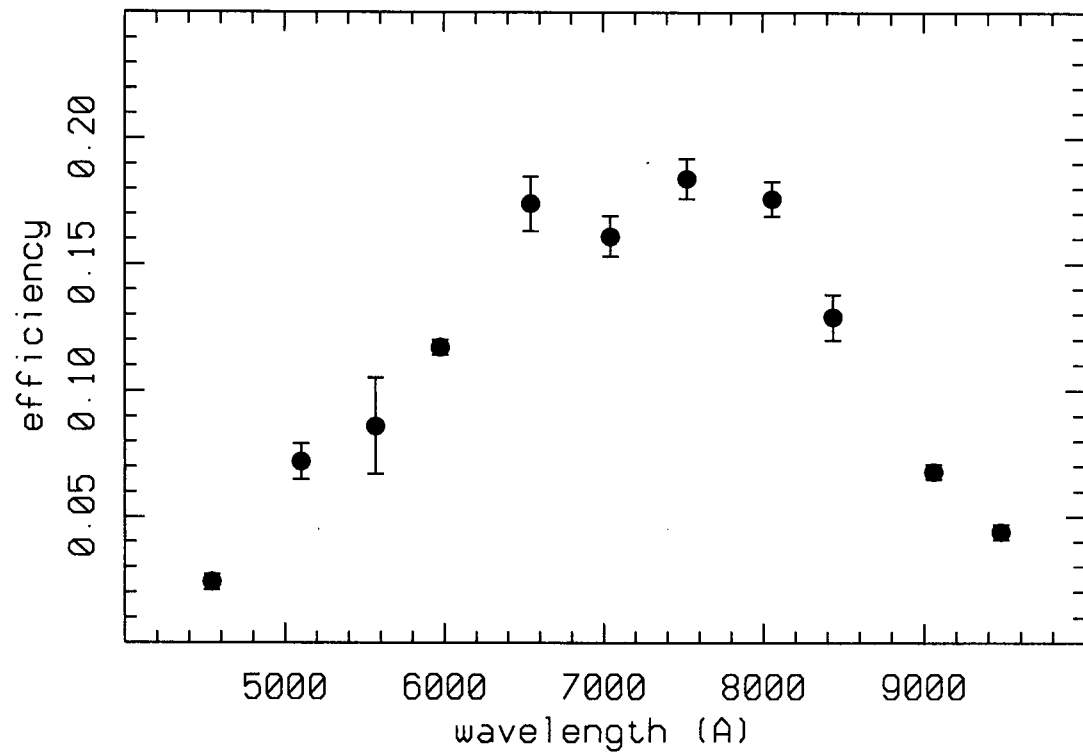


Figure 2.2 System throughput from [21]. The total effect of atmospheric transmission, primary-mirror reflectivity, corrector transmission, and CCD quantum efficiency is shown.

2.2 Drift-Scanning and Time-Delay Integration

The zenith pointing restriction renders conventional imaging useless for integration times of more than a few seconds. Time-delay integration mode is a method of collecting data in which the telescope and CCD stay fixed and the scan rate on the CCD is matched with the sidereal rate. The integration time of a source is the time it takes to move from one side of the CCD to the other. Once the images are acquired, conventional methods of co-adding observations on different nights is possible to increase the effective integration time. The main advantage this method has is the reduction of CCD non-uniformities which lead to noise. This is possible since objects or points on the image have been detected with the mean sensitivity of all the pixels in that column. While the increase in uniformity is along each column, column to column variations can be reduced by processing each column to determine a mean sky level that defines the relative sensitivity to light that has the exact spectrum of the sky at the time of exposure [18]. This reduction in noise leads to magnitude limits more than a magnitude fainter than with conventional integration.

There are two main difficulties in this type of data recording: the curved stellar paths across the focal plane and the discrete shifting of charge to match a continuously moving object. Since the images do not track in straight lines if observations are not made at the equator, an asymmetrical image deformation and shift of the peak of the intensity in the north-south direction occurs [15]. If a proper correcting lens is not applied, the smearing can be quite significant at the edges of the images (2 arc-seconds) [21], making source classification based on shape parameters difficult. The second difficulty becomes significant with under-sampled data (Gaussian PSF standard deviations ≤ 0.85 pixels) and leads to a symmetrical elongation of the objects east-west profile that results in a reduction in an observed object's peak intensity [15].

2.3 Data

Data taken in 1996, 1997 and 1999 were previously reduced and compiled into the UNMS1 catalog [21]. It consists of $\sim 600,000$ sources detected in at least 1 of the 39 filters mentioned above. Fig. 2.3 shows a histogram of the number of detected sources per band. Sources in the catalog were calibrated astrometrically and photometrically with data in the Hubble Space Telescope Guide Star Catalog (GSC) [27, 39, 24]. An iterative scheme is used to match stars in the catalog to those in the GSC. The brighter stars are matched first to obtain a rough positional calibration then the match is improved by looking at fainter and fainter stars. Once the stars are cross-correlated, the sources' positions and magnitudes are corrected. The corrected coordinates generally have RMS errors of < 1.0 arcseconds in both right ascension and declination.

Using 22 spectrophotometric standard stars in the survey field observed at Kitt Peak National Observatory (KPNO), a more accurate photometric calibration was made and discussed in [20]. These stars pass through the observed fields at intervals of roughly 30 minutes providing a sufficient sample to accurately calibrate sources.

Once the catalog sources were calibrated, photometry files obtained on different nights using the same filter were combined. The program used to extract the photometry files, *Tdi*, will be described in the next section. Sources were matched positionally to within 3.5 arcseconds and within 1 magnitude. Another requirement is that the source must have been detected on more than one night. This was done to remove cosmic rays and other spurious detections. The probability of finding a second object within 3.5 arcseconds of a given object is 2% and therefore the 3.5 arcsecond limit results in roughly comparable rates of dropouts and contamination in the most crowded area of the survey (see [21] for details).

The random error in the magnitude of a source is estimated from the number

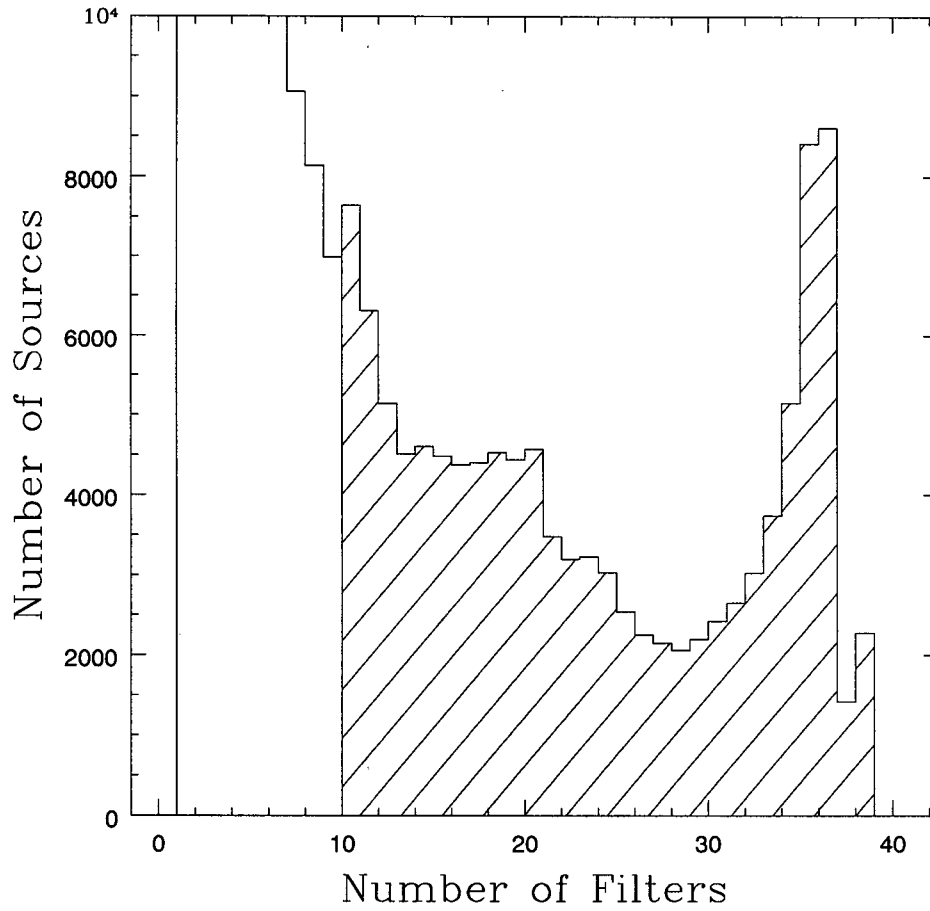


Figure 2.3 Histogram of sources observed in N filters. The shaded area shows the data used in this analysis.

of objects detected, the isophotal areas and the background variance. For each object, the variance of the mean is computed from the individual magnitude variances, providing an estimate of the random noise.

These steps produce a single photometry file for each wavelength band. These files are then merged to form a single file of SEDs for each object. The catalog provides semi-major and semi-minor axes measurements for each source as well as AB magnitudes [36] given by

$$m_\nu = -56.10 - 2.5 \log f_\nu \quad (2.1)$$

where f_ν is the specific flux, in $\text{W m}^{-2} \text{Hz}^{-1}$, averaged over the filter bandpass. Because of the narrow filter bandwidths, the AB magnitudes are a good approximation to the monochromatic flux at the central wavelengths of the filters.

Although some observations were made with right ascension as early as 9 hrs, the region of overlapping coverage extends approximately from 12-19 hrs and the survey range is 12-18 hrs ($10 \text{ deg} > b > 85 \text{ deg}$, where b is galactic latitude). The last hour was removed from the survey in order to avoid the high stellar density near the galactic plane. The 50% completeness limits for the various wavelength bands range from 19.0 to 21.1 mag; the median value is 20.4 mag [21].

2.4 *Tdi* Photometry and SExtractor

Two different software packages were used to extract sources and photometric information from the data. The first, *Tdi*, written by Hickson [21] was developed specifically for the time-delay integration data. The software is designed to read data from the CCD and display the image and/or write the recorded image to disk, line by line as the charges shift to the end of the CCD. This results in a continuous data stream of

90 Kbytes/s for the 2048×2048 Loral CCD. *Tdi* can also read a saved image file as if it were being read from CCD and can photometrically reduce the data. The interface is graphical and consists of various window areas for image display and parameter inputs. SExtractor was not designed to handle time-delay integration data files, but instead the more standard fits images. SExtractor is a source extraction program developed by Bertin and Arnouts (1996) [1]. The program is particularly suited to analyze large surveys as speed, flexibility and robustness in the extraction of sources is stressed in the design of the program. SExtractor can be easily run from a script as the program takes command-line arguments that define the detection parameters.

The first steps that *Tdi* makes when reducing data are bias subtraction, flat-field correction and sky subtraction. The bias correction is determined by covering the CCD and averaging the lines of an exposure. As mentioned above flat-fielding becomes a one-dimensional correction since any given source will be observed by every pixel in a column in the direction of shift and therefore variation in pixel response in that direction is greatly reduced. The only consideration is that of column-to-column variations. Images used for flat-fielding are of clouds lit by the moon. Sky subtraction is needed since the value of each pixel is the sum of a background or sky level and the light from the source. This is accomplished by keeping track of the pixel values along one column, taking the median value for each column and subtracting it from each source. Computed after the sky subtraction, the noise calculation is an iterative process that computes the standard deviation for each row and then rejects pixels that are 2σ or more from the mean.

Since SExtractor is strictly a source extraction program the images supplied to it are flat-fielded and bias subtracted. SExtractor first estimates the background level and produces a background map for the image. For this map, the background

is clipped iteratively until convergence occurs at $\pm 3\sigma$ around its median. If sigma is changed by less than 20% during that process, the field is considered uncrowded and the mean of the clipped histogram is taken as the value for the background. If the field is found to be crowded the background value is taken to be the mode ($mode = 2.5 \times median - 1.5 \times mean$).

Once these pre-processing steps are complete object detection and photometry are performed in each respective program. *Tdi* first smoothes over the entire image with an interactively chosen smoothing filter. The available filters include a simple box-car filter, a Gaussian function and a Sersic function. Eq. 2.2 gives the Sersic profile, where r_e is the radius within which the galaxy emits half of its brightness, Σ_e is the surface brightness at r_e , b_n is determined from a given shape parameter, n . Each of these filters have variable parameters: box size, FWHM and n respectively.

$$\Sigma(r) = \Sigma_e \exp \left(-b_n \left[\left(\frac{r}{r_e} \right)^{1/n} - 1 \right] \right) \quad (2.2)$$

Smoothing enhances faint objects in the image, by optimizing the S/N ratio as the resolution is reduced but smaller signals are accentuated above the pixel-to-pixel variations. The most effective filter to use should match the expected light profile of the sources. For example, a Gaussian profile filter should be used for stars where as for galaxies the observed light profile is more closely Sersic. All of the photometric parameters are calculated from the original, unsmoothed image.

For each connected set of pixels having intensities above 2.5σ in the smoothed image, the flux is retrieved for each corresponding pixel in the unsmoothed image. The detection isophote of each object is the boundary of each set of connected pixels and the sum of these is the isophotal flux for the object. These sets of pixels are then

checked for blended sources. The coordinates and fluxes of the sets are passed to the deblending algorithm that attempts to distinguish sources by raising the threshold in magnitude steps of 0.2 mag. When a separation is detected, a flux is assigned, in proportion to their respective maximum intensities, to each of the sources from the total flux calculated previously. The two separated sources are each sent back to the deblending algorithm to be checked for further blended sources. When a source can no longer be separated by the deblender (i.e. when the threshold steps above the maximum intensity of the source), it is sent to the photometry algorithm. The efficiency of deblending is limited mostly by seeing and sampling, but for these data, the fraction of objects affected by blending is roughly 1%.

Smoothing or simply convolving the image with a specifiable convolution mask is the next step for SExtractor as well. Eight connected contiguous pixels are extracted from a template frame, which is the convolution of the image with the mask. Just as in *Tdi* a detected source is simply a group of connected pixels that exceeds some threshold above the background. For each source thresholding methods must be used together with a deblending routine to separate sources that have been extracted as a single source. Each set of connected pixels is re-thresholded at 30 levels exponentially spaced between its primary extraction threshold and its peak value. At each junction any branch will be considered as a separate component if the integrated pixel intensity above the junction of the branch is greater than a certain fraction of the total intensity of the composite object and if this happens for at least one more branch at the same level.

The *Tdi* photometry algorithm takes the flux of the sources and computes the isophotal magnitude, $m_i = Const - 2.5 \log(flux)$, and the first and second moments of the flux distribution. Next, the first three moments of the intensity distribution

are determined for each object passed into the photometry program. The zero-order moment gives the isophotal flux, the first-order moments give the centroid of the image, and the second-order moments determine the major and minor axis values and position angle of the object through the moment-of-inertia tensor.

The total magnitude is then estimated by fitting a Gaussian or exponential profile to the source in order to account for the light that falls outside of the isophote. The flux in the outer pixels is then added to the isophotal flux to obtain the estimated total magnitude. The method was tested on artificial images designed to match the real data in terms of resolution and noise. The method was found to provide an unbiased estimate of the true total magnitude and to have lower noise than alternative estimators [21].

There are two final steps before the sources are added to the photometry file. The first is the checking of the minimum S/N ratio. If a source has an estimated S/N ratio that is smaller than this minimum, the source is rejected. The noise for each source is estimated by multiplying the RMS noise calculated in the above step by the square root of the number of pixels in the object. The last check serves to reject a source that only covers a small number of pixels (5). To summarize, the three photometric selection criteria are based on surface brightness (Eq. 2.3), intensity (Eq. 2.4), and S/N ratio (Eq. 2.5). The criterion described in Eq. 2.3 refers to the minimum area limit, A_m , where f is the flux within the detection isophote and \bar{i} is the mean intensity within the isophote. Eq. 2.4 describes the basic detection threshold where i_m is the detection threshold intensity. The last criterion arises from the minimum S/N ratio, ζ , where σ^2 is the background noise variance and g is the system gain. The photometry program then finally produces a list of all objects with magnitudes, positions, estimated errors, image parameters and the seeing FWHM,

determined from star images.

$$f/\bar{i} \geq A_m \quad (2.3)$$

$$\bar{i} > i_m \quad (2.4)$$

$$f > \zeta^2(g + \sigma^2/\bar{i}), \quad (2.5)$$

The photometry program then finally produces a list of all objects with magnitudes, positions, estimated errors, image parameters and the seeing FWHM, determined from star images.

The remaining steps of SExtractor is much the same. Low threshold detections are dealt with by subtracting the mean surrounding surface brightness from the source's surface brightness and if the mean surface brightness still falls above the detection threshold then it is passed into the catalog.

To calculate magnitudes, SExtractor uses both an adaptive aperture method and isophotal correction scheme (similar to *Tdi*) to estimate the total magnitude of an object. The total magnitude with the smallest error is chosen between the two. The adaptive aperture is taken except if a neighbour is suspected to bias the magnitude by more than 0.1 mag. The adaptive aperture method takes the second-order moments of the object's light distribution to define a Gaussian profile with a mean standard deviation. The profile is taken to set an elliptical aperture with an ellipticity and position angle scaled by 6 times the mean standard deviation. The calculated aperture defines the area and light which is considered to belong to the source.

SExtractor has one final step that *Tdi* does not take, source classification. Seeing an object as a vector of parameters, classifying stars and galaxies is essentially finding the best hyper-surface between the two classes in parameter space [1]. Employing neural networks to define this hyper-surface and classify sources has shown to be both efficient and accurate. A neural network is a group of connected units called

neurons whose behaviour is based upon real biological neurons. Neural networks that are used for classification usually consist of one input layer of nodes, a number of intermediate layers, and one final output layer. The input nodes are provided with a set of parameters and the output node offers an index to classify the input source. Neurons pass information from the input layer through the intermediate layers and onto the final layer since each node in a layer is connected to each node in the next layer, but within a layer the nodes are not connected. Fig. 2.4 shows schematically the structure of a neural network. One of the most interesting features of a neural network is their ability to learn and generalize in a given context. For example, dealing with confusing cases like merged objects or close neighbours is straightforward as long as the network has learned to recognize them. The structure of the network in SExtractor is 1 input layer, 1 hidden layer, both with 10 nodes and 1 output layer of 1 node. Choosing the best input parameters defines the effectiveness of the network. Bertin and Arnouts [1] summarize characteristic of ideal input parameters. First and foremost, the inputs should discriminate between stars and galaxies efficiently over all magnitudes detectable. In addition, invariance under translation and rotation are important. Parameters robust with respect to noise, image distortion and crowding should all be included and should be as independent as possible from the characteristics of the exposure.

Considering all these factors, Bertin and Arnouts [1] used 8 isophotal areas, the peak intensity and the seeing as their 10 input parameters for the classification network. The output is a real number from 0 to 1 where 0 corresponds to a confidently classified galaxy and 1 a star. They show that the index closely estimates Bayesian a posteriori probabilities.

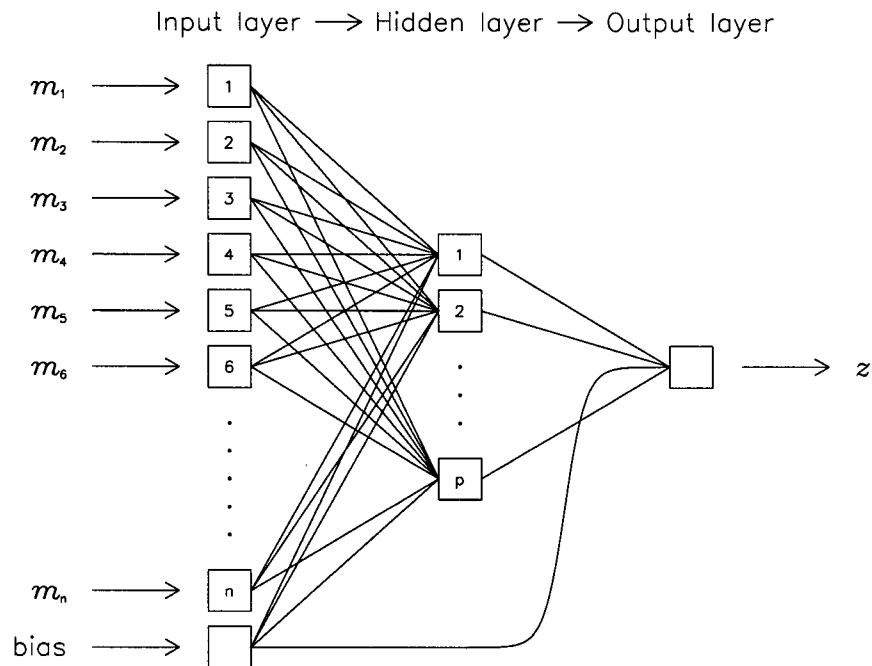


Figure 2.4 A schematic diagram of a neural network from Firth et al. [14]. For the SExtractor network $n = 10$, $p = 10$ and no bias input is used.

Chapter 3

Analysis

The previous chapter dealt with the telescope, data set and photometric software. This chapter describes how the photometric programs were applied and provides the steps taken in our data analysis. Our data are unique because of the extent of wavelength coverage, large number of filters and narrow bandwidths. A catalog was produced from data taken with the high-read noise CCD in the 1996 and 1997 observing seasons. The catalog was optimized to detect stars as the smoothing filter used was a 3×3 pixel filter and the total magnitudes were calculated by fitting Gaussian light profiles. Two independent methods of source classification were first applied to the data set, a template fitting routine and SExtractor's stellarity index. Sources that were classified as galaxies were subject to further classification into higher resolution redshift bins. While the advisability of using total magnitudes to estimate spectral energy distributions is debatable because the flux in different bands is not determined from exactly the same areas [26], it is investigated here.

3.1 Spectral Energy Distribution Fitting

The spectral energy distribution of sources in the UNMS1 catalog were fitted to stellar and galaxy spectral templates. A total of 261 templates were used in the initial classification. Pickels (1998) [37] provided 131 stellar templates, which include all normal spectral types and luminosity classes at solar abundance and metal-weak,

Table 3.1. Galaxies Used in Producing Templates

| Elliptical | S0 | Sa | Sb | Sc |
|------------|----------|----------|----------|----------|
| NGC 1399 | NGC 1023 | NGC 1433 | NGC 210 | NGC 598 |
| NGC 1404 | NGC 1553 | NGC 2681 | NGC 2841 | NGC 1058 |
| NGC 6868 | NGC 4350 | NGC 4314 | NGC 4102 | NGC 1637 |
| NGC 7196 | NGC 4382 | NGC 4594 | NGC 4826 | NGC 2403 |
| ... | NGC 6340 | NGC 4569 | NGC 7083 | NGC 3432 |
| ... | ... | NGC 4736 | ... | NGC 3994 |
| ... | ... | ... | ... | NGC 4259 |
| ... | ... | ... | ... | NGC 5194 |

metal-rich F-K dwarf and G-K giant components from 115 - 2500 nm in steps of 0.5-nm. Eleven galaxy templates from Kinney et al. (1996) [25] contain spectral information from 120 - 1000 nm and include 6 starburst galaxies and one of each major galaxy type (elliptical, S0, Sa, Sb, Sc). Each of the galaxy templates is the average spectra of at least 4 galaxies of their respective types. The average spectra are shown binned in Fig. 3.1. Table 3.1 shows the galaxies used in calculating each averaged template.

Each of the 11 galaxy templates were redshifted out to $z = 1.2$ at intervals of 0.1, producing 130 galaxy templates. The templates were first convolved with each of the 39 filter transmission curves in order to reduce the resolution of the templates and to

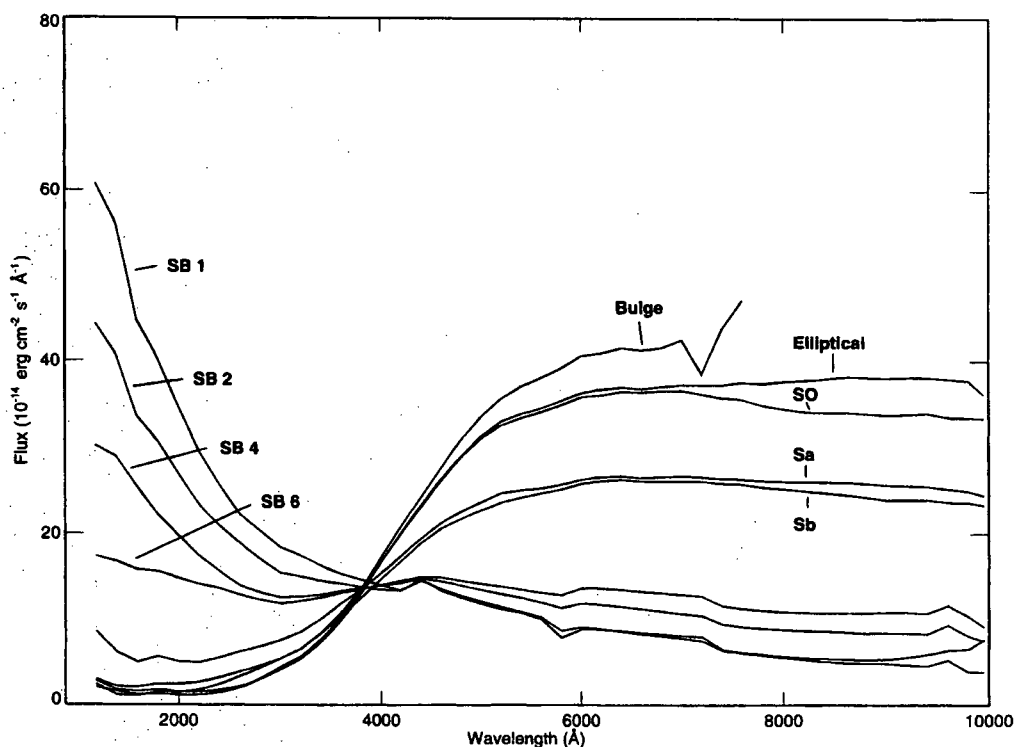


Figure 3.1 Galaxy spectral templates. The averaged and binned spectral templates from [25]

calculate from the spectra what relative flux will be observed through any of the 39 filters from each template source. The spectral templates were reduced to 39 spectral points corresponding to the 39 filters used in observations. Fig. 3.2 shows how the spectral templates were reduced to match the resolution and response of the filters used in the survey. The spectrum of an A5 V star is shown (solid) along with the transmission curve (dotted) centred on 545.5 nm and the solid dot is given by Eq. 3.1 where F_{λ} is the calculated flux, N is the number of points in a transmission filter and T is the transmission value at each respective point.

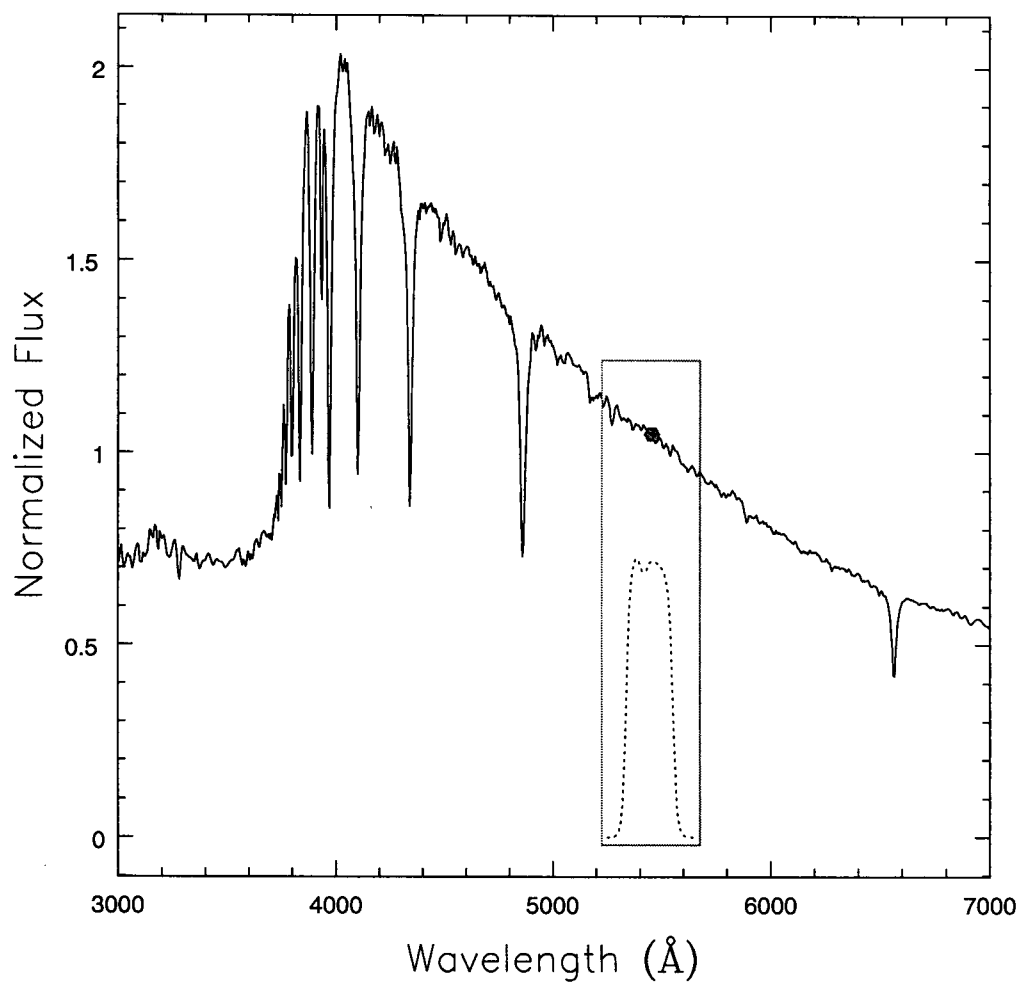


Figure 3.2 Spectrum reduction. The spectrum of an A5 V star is shown (solid) along with the transmission curve (dotted) centred on 545.5 nm and the solid dot is given by Eq. 3.1. Each template spectrum is reduced to 39 points with the above method.

$$F_\lambda = \frac{\sum_{i=1}^N F_{\lambda_i} T_i}{\sum_{i=1}^N T_i} \quad (3.1)$$

Once templates were produced, we tested for the minimum number of bands to get a reliable classification. The templates themselves acted as a set of test objects. Gaussian noise based on the uncertainties in the UNMS1 catalog was added to the templates and a random number of points were removed from each template (jack-knife sampling). Each template provided 1000 test sources. The distribution of sources detected in N bands was constructed to be uniform. The resulting 261,000 test sources were passed through the fitting routine outlined below; the resulting classification efficiency is shown in Fig. 3.3. The classification efficiency remains above roughly 90% until the number of filters is below 10, thus only sources detected in 10 or more bands were kept.

As mentioned in §2.3, the UNMS1 catalog provides AB magnitudes. The magnitudes and respective errors were straightforwardly converted into specific fluxes. If no magnitude error was given for a source, the average error of other sources detected in each respective filter was used. One correction applied to the fluxes accounted for a probable error in calibration of the KPNO observations and resulted in a brightening of sources at long (900nm) and short (500nm) wavelengths. The empirical corrections were best fit by the following function:

$$C(\lambda) = 2.7663 - (5 \times 10^{-4})\lambda + (3 \times 10^{-8})\lambda^2 + (4 \times 10^{-13})\lambda^3 \quad (3.2)$$

where $C(\lambda)$ is the correction factor applied to the fluxes in the following manner:

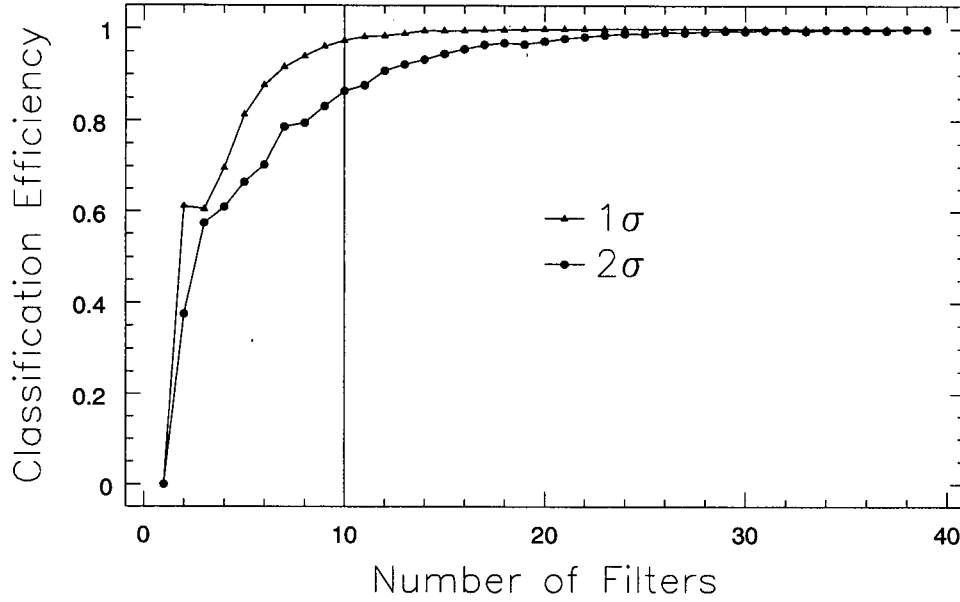


Figure 3.3 Classification efficiency as a function of the number of bands a source is detected in. Results from simulated data where the modeled noise is the 1σ of the actual data set and 2σ . The drop in classification efficiency at 10 filters is evident.

$$F_c(\lambda) = \frac{F_o(\lambda)}{C(\lambda)} \quad (3.3)$$

where $F_c(\lambda)$ is the corrected flux and $F_o(\lambda)$ is the original flux. The corrected fluxes were then fed through the χ^2 fitting routine and compared with each template in turn. Eq. 3.4 shows the value that was minimized when fitting the templates, where y_i is the flux value at a given wavelength for a source, y_{ti} is the matching template flux point and a is simply a scaling parameter.

$$\chi^2 = \sum_{i=1}^N \left(\frac{y_i - ay_{ti}}{\sigma(i)} \right)^2 \quad (3.4)$$

A χ^2 value for each template is calculated and the best matching star and galaxy template is flagged and written to output. A ratio ($\chi_{s/g}^2$) of the χ^2 value for best fitting stellar template (χ_{star}^2) to the that of the best fitting galaxy template (χ_{gal}^2) provides the basis for the classification, where a value < 1 implies the best fitting template was stellar and a value > 1 implies a galaxy. Figs. 3.4 and 3.5 shows the SEDs of two sources, one which was correctly classified as a star (Fig. 3.4) and the other correctly classified as a galaxy (Fig. 3.5). The dotted lines show the best fitting stellar template and the dashed lines show the best fitting galaxy template. The corresponding image of the sources is shown in Fig. 3.6, where the dotted line circles the star and the dashed line circles the galaxy.

3.2 Stellarity

SExtractor's stellerity index was used as the second method of source classification. The *Tdi* software program extracted fits images from four nights of observations. A different filter was used each night (*BVRI*). The images are 1024 pixels square and the centres of the extracted images were separated by 1 minute in right ascension. This resulted in roughly 400 images per night (band) and each image overlapped with the next by roughly 1.4 arcminutes. The extracted images were biased and sky corrected by *Tdi* and then analyzed by SExtractor. Each fits image was analyzed 5 times where each pass consisted of convolving the image with a different mask. The five convolution masks used were a Gaussian with a 3 pixel FWHM, and 4 top-hat

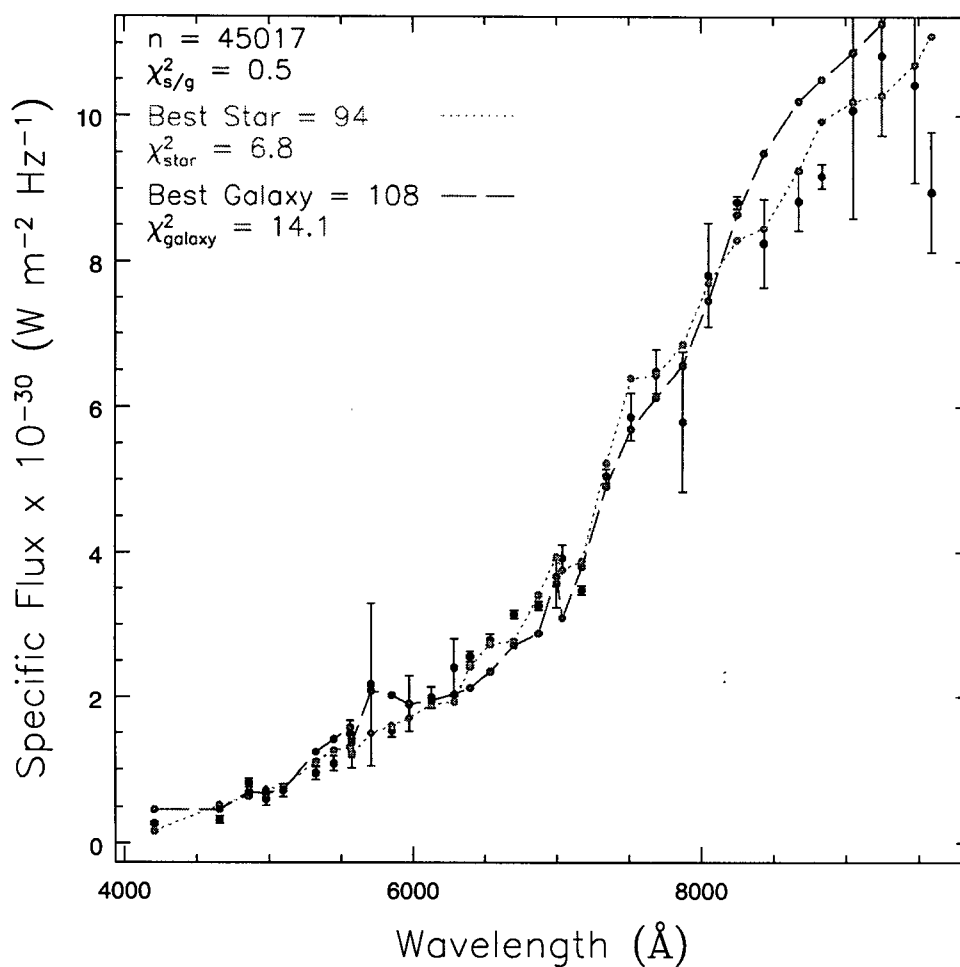


Figure 3.4 A sample stellar SED that was correctly classified by the least-squares (χ^2) program. The dotted lines show the best fitting stellar template and the dashed lines show the best fitting galaxy template. See Fig. 3.6 for the corresponding image.

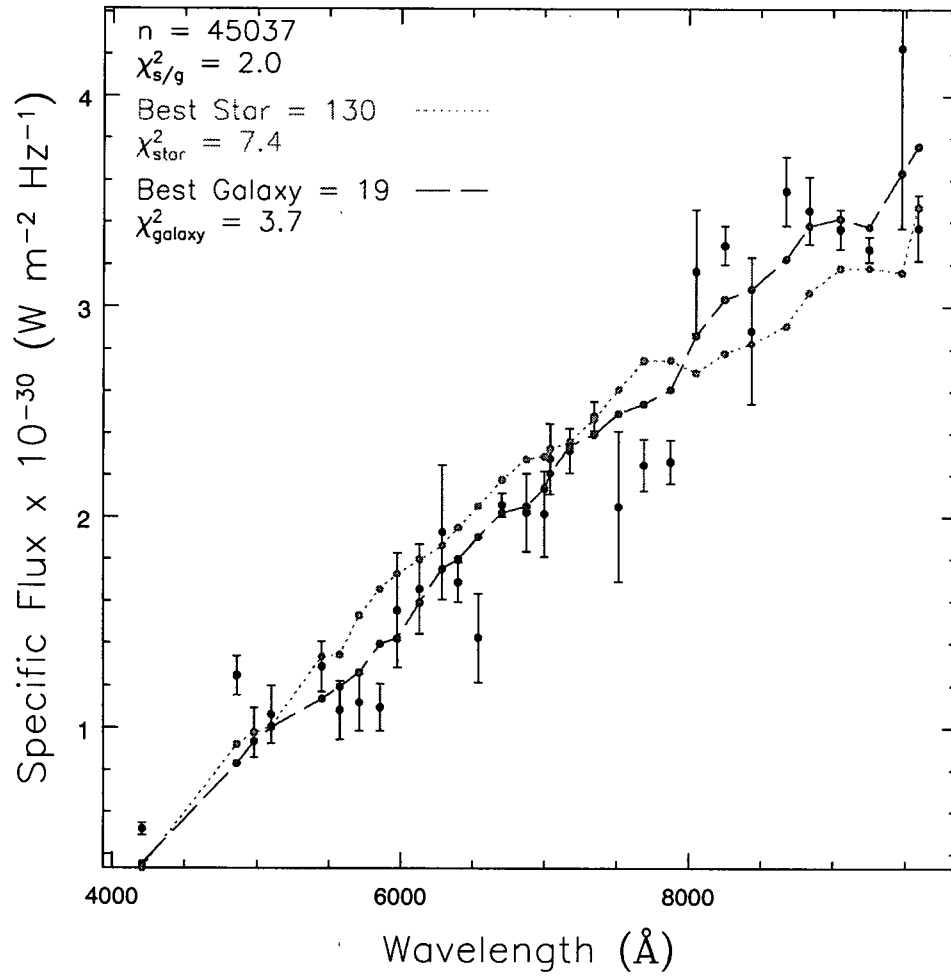


Figure 3.5 A sample galaxy SED that was correctly classified by the least-squares (χ^2) program. The dotted lines show the best fitting stellar template and the dashed lines show the best fitting galaxy template. See Fig. 3.6 for the corresponding image.

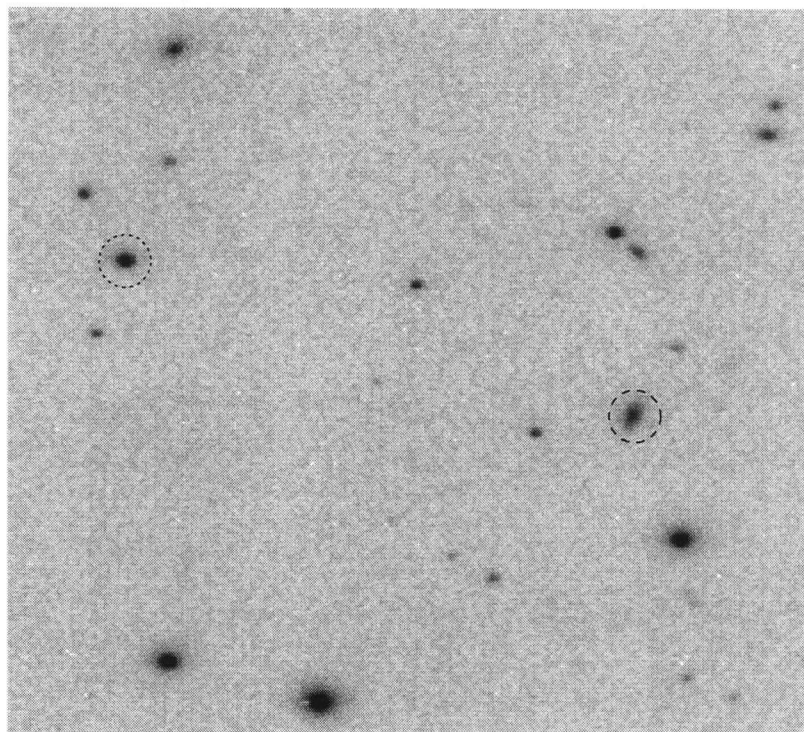


Figure 3.6 A sample *Tdi* image. The star and galaxy detailed in Figs. 3.4 and 3.5 are shown (dotted and dashed) respectively.

functions with 2, 3, 4 and 5 pixel diameters. The Gaussian mask optimized the search for stars or small dim galaxies and the top hat functions served to highlight larger lower surface brightness sources. For each pass the detection threshold was set to 2σ and the minimum number of contiguous pixels for something to be considered a source to 3. Each resulting photometry file provided an object number, X and Y image coordinates, corrected isophotal magnitude, aperture magnitude, the size of the isophotal area, the semi-major and minor axes, the eight isophotal areas used in the neural network and the star-galaxy classifier index. The X and Y image coordinates

Table 3.2. Description of Equations 3.5 and 3.6

| Symbol | Value |
|----------------|-----------------------------------|
| c_{δ}^1 | Pixel scale in R.A. |
| c_o^1 | Reference point in R.A. |
| c_{δ}^2 | Pixel scale in Declination. |
| c_o^2 | Minimum declination of the image. |

were transformed into declination and right ascension by the following formulae:

$$Dec = yc_{\delta}^2 + c_o^2 \quad (3.5)$$

$$R.A. = \frac{1}{15} \left(\frac{(x - 512)c_{\delta}^1}{\cos(Dec)} + 512c_{\delta}^1 + c_o^1 \right) \quad (3.6)$$

where Table 3.2 describes the symbols.

3.3 Cataloging and Final Classification

After the appropriate coordinate transformations, all the photometry files produced by SExtractor from each band and convolution pass were merged. Objects were matched to a positional uncertainty of 3 arcseconds. The resulting merged catalog contained ~ 70000 detections that were detected in at least the V , R and I bands.

The system throughput is exceptionally low in the B band and hence information from the 3 other filters was the main focus for the catalog.

Sources that were within 10 pixels from the edges, brighter than $m_R=14$, and/or within a certain distance from a bright star ($m_R < 12$) were clipped from the catalog. All point sources suffered from an image defect, but the affect became appreciable at any magnitude brighter than $m_R = 12$. In addition, bright stars, bled appreciable over a large area. Fig. 3.7 shows a saturated star and its effect on neighbouring pixels. The sources near saturated stars were clipped from the final catalog. All the resulting sources were merged into a catalog containing positional, magnitude and stellarity parameters.

The final stellarity index attributed to a source was a combination of stellarities from the V , R and I analyses. To account for image inconsistencies and errors the final stellarity of a source was calculated in the following way.

- 3 stellarities are sorted
 - 2 differences are taken (Δ_1, Δ_2)
 - IF (Δ_1 is $> 2 \times \Delta_2$) OR (Δ_2 is $> 2 \times \Delta_1$) then
 - The 1 outlier is rejected and the reduced stellarity is the average of the two remaining values
- ELSE
- The average of the 3 values was taken as the reduced stellarity

Sources with a final stellarity of less than 0.5 were treated as galaxies and passed into the χ^2 galaxy classifying program in order to be classified with higher resolution

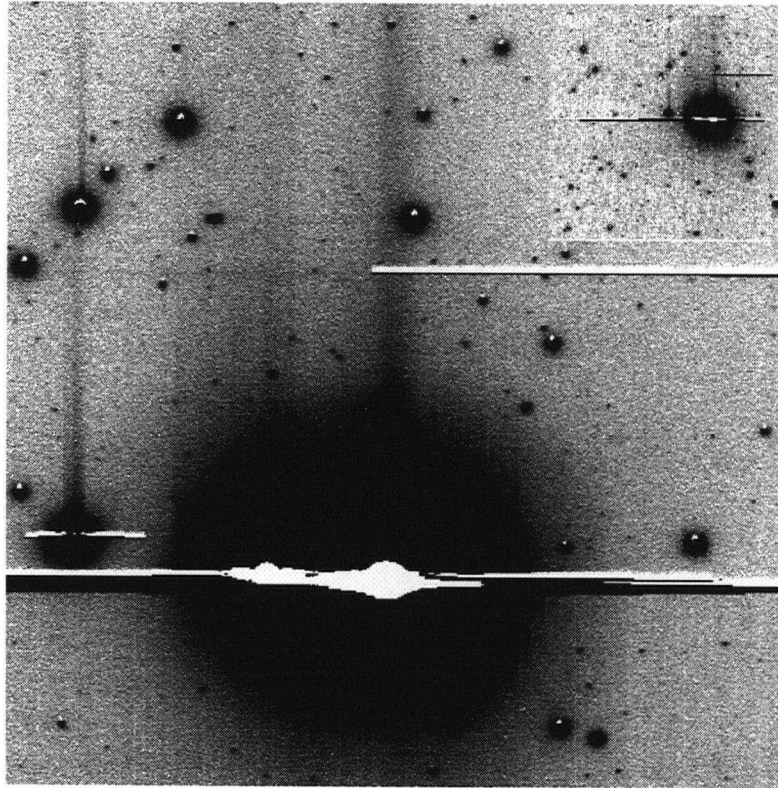


Figure 3.7 A sample image of a bright star which caused surrounding image problems. Regions like this were clipped from the data.

redshift bins. The classification scheme is identical to that used previously except that only galaxy templates were fit and the resolution in redshift of the galaxy templates was increased to 0.01.

Chapter 4

Results and Discussion

The resulting classification catalog will be compared here before describing the redshift distribution of sources found in the data.

To quantify the distinction between stars and galaxies, a ratio of the χ^2 value for the best fitting stellar template to the χ^2 value for the best fitting galaxy template was taken. Sources best fit by a stellar template have $\chi_{s/g}^2$ values less than 1 and those best fit by a galaxy template have $\chi_{s/g}^2$ values greater than 1. Fig. 4.1 shows a histogram of the $\chi_{s/g}^2$ ratio. A large fraction of the sources are distributed around 1. This could be a result of degenerate spectral templates, which arise from degrading the spectra to the narrowband resolution used here, and uncertainties of the data. It should be noted that since the stars can only occupy the region $0 < \chi_{s/g}^2 < 1$ and galaxies can have $1 < \chi_{s/g}^2 < \infty$, the horizontal axis does not represent a linear distribution in this parameter space. Despite this, a bimodal distribution representing stars and galaxies is clearly not evident. This does not suggest that the classification scheme is flawed, only that questionable sources will not be easily picked out with this technique.

A plot of ellipticity versus stellarity (Fig. 4.2) shows the clear separation of populations that the stellarity index provides. Galaxies, which scatter vertically in this diagram, are more evenly distributed whereas the stars are more concentrated around the mean ellipticity. Few galaxies are found with $e > 0.6$ because faint edge-on galaxies are harder to detect. The majority of sources have $e \sim 0.15$ and this is expected

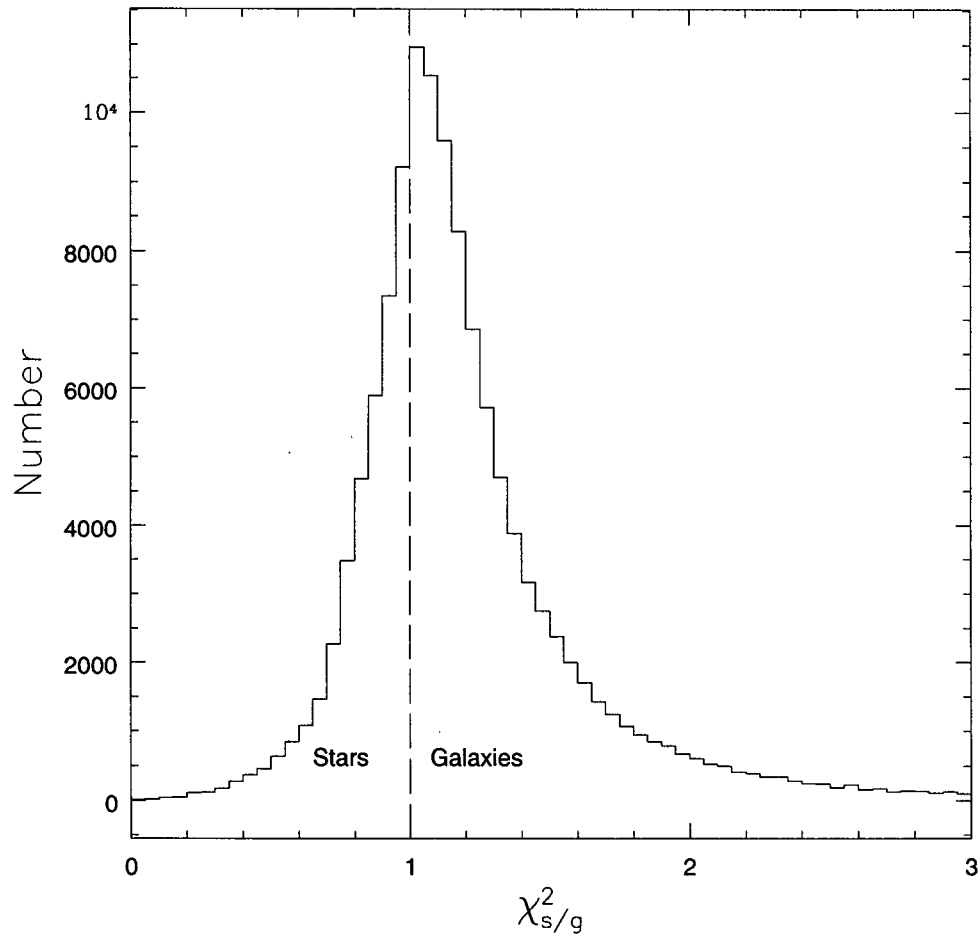


Figure 4.1 The distribution of $\chi^2_{s/g}$ values of the cataloged sources. If the best fitting template is a stellar template the $\chi^2_{s/g}$ value is less than 1 and if a galaxy template provided the best fit the value is greater than 1 .

with this data. Even if sources have an intrinsic ellipticity of 0, the discrete shifting of charges in the CCD matched to the continuous drift of the sky results in an elongation in the direction of motion. Fig. 4.3 illustrates the effect of magnitude on the ability of SExtractor to confidently classify sources. The uncertainties arise when $m \gtrsim 18.5$.

Before testing the two classification schemes, the resulting distributions were compared. Plotted in Fig. 4.4 is the $\chi^2_{s/g}$ index against stellarity. The plot shows no real correlation, but only if sources that were classified as galaxies by SExtractor are considered, the fraction of those sources that were also classified as galaxies by the χ^2 routine is 80%. The source of the discrepancy arises at the stellar end where the χ^2 routine classifies many stellar sources as galaxies. It should also be noted again that while the observed area of sky is the same, the χ^2 program reduced data that were taken in 1996 and 1997 and suffered from a high read noise CCD. Therefore the photometric errors for that data are greater than the data taken in 1999 and 2000. The images examined by SExtractor were recorded with the more efficient CCD in 1999 and 2000.

We were able to verify galaxy identification from *TDI* and SExtractor by cross-correlating the two samples with the NASA/IPAC Extra-Galactic Database (NED). The search was based on the positions of the sources. All sources that were matched within 0.1 arcminutes from the NED galaxy search were considered extra-galactic; the corresponding classification indices are plotted in Figs. 4.5 and 4.6. The NED database is not complete over the area of interest and only 3% of the sources and 10% of the galaxy candidates passed into the NED search returned a match. Just as the $\chi^2_{s/g}$ -stellarity comparison showed no correlation while the sample of "galaxies" did, the significance of these results must be considered. In Fig. 4.5, we find that 80% of the sources were correctly classified as galaxies by the χ^2 fitting routine. The

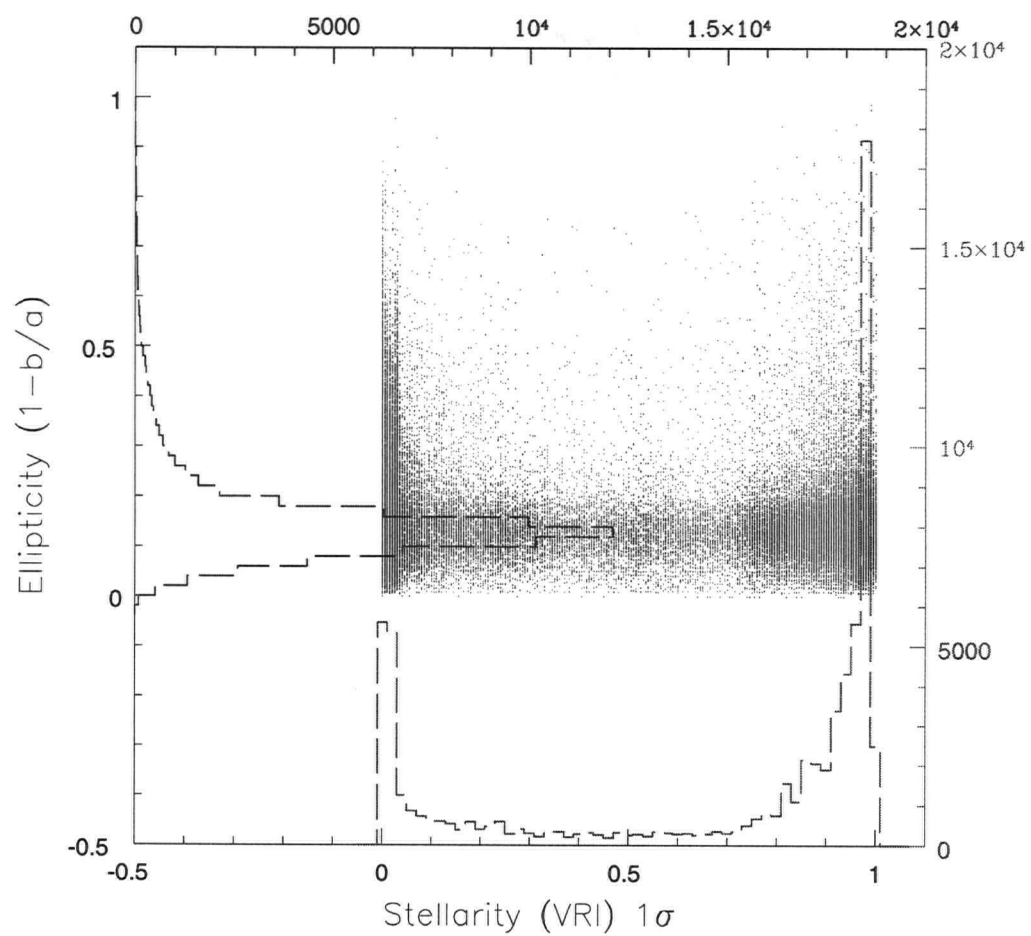


Figure 4.2 Ellipticity vs stellerity for SExtractor extracted sources. The stellerity indices 0 and 1 are confidently classified galaxies and stars respectively.

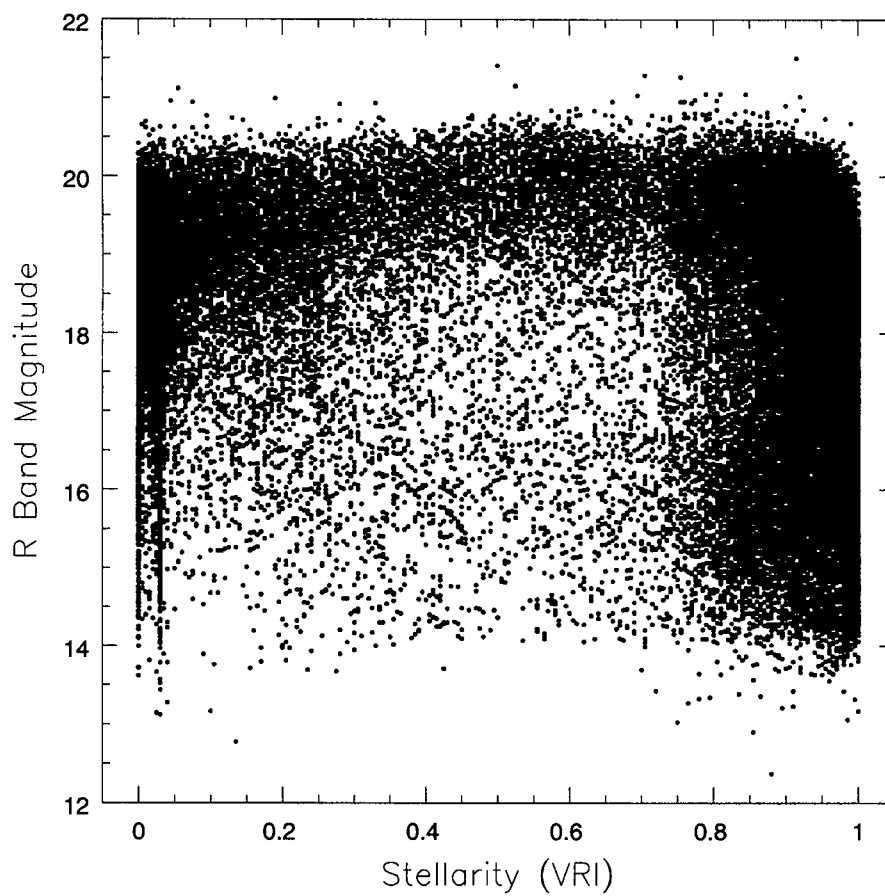


Figure 4.3 m_R versus stellerity. This shows the effect of magnitude on the ability of SExtractor to confidently classify sources. Larger uncertainties arise when $m \gtrsim 18.5$.

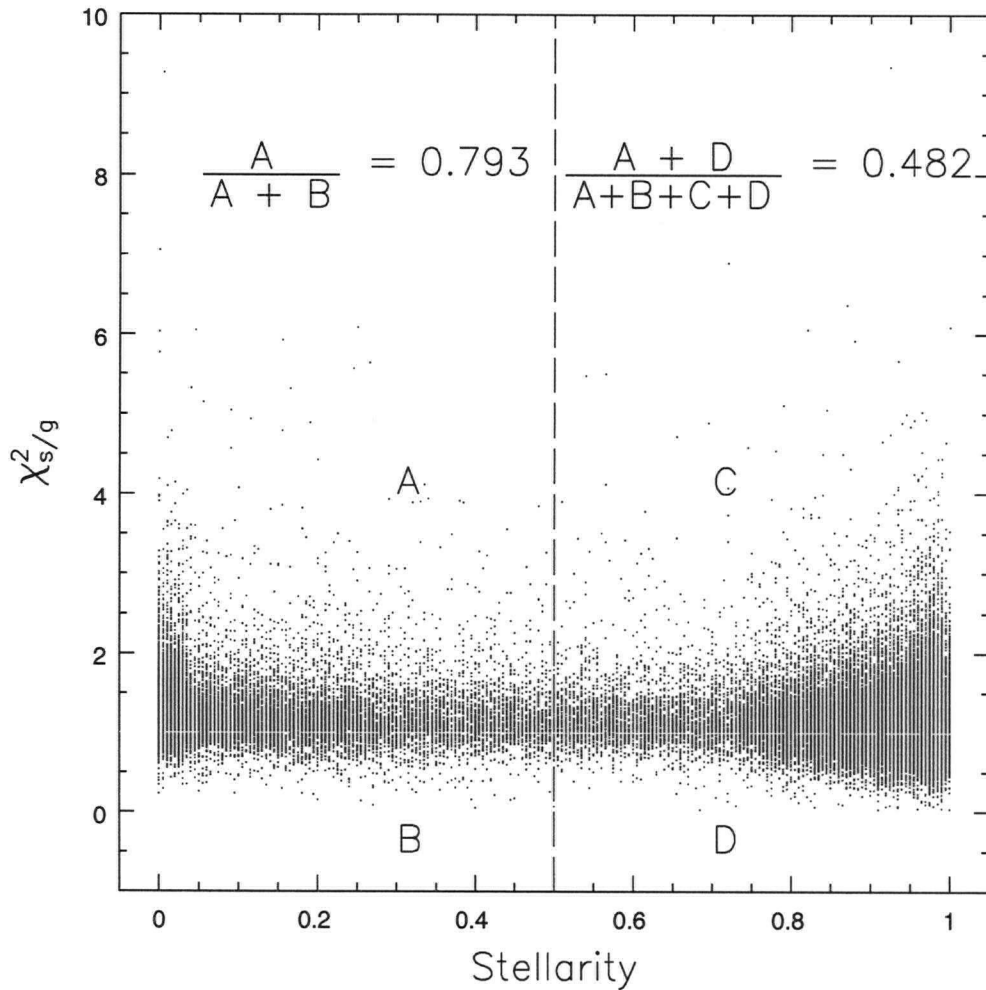


Figure 4.4 $\chi^2_{s/g}$ versus stellarity. There is no correlation between the two methods since the percentage of sources that were classified in the same manner by both methods is 48.2%. The comparison suffers from the large group of sources that $\chi^2_{s/g}$ classifies as galaxies while SExtractor classifies as stars. The percentage of SExtractor galaxies that were also $\chi^2_{s/g}$ galaxies is 79.3%.

stellarity index matched 90% of the sources (Fig. 4.6). The sources classified as stellar by SExtractor include Quasi-Stellar Objects (QSOs) and faint ($R > 19$) galaxies.

Sources with a stellarity < 0.5 were taken as galaxies candidates because of the better match with NED-confirmed galaxies and the more apparent bimodal distribution. These sources were carried over to the second χ^2 routine which only classified the sample into Hubble type and higher resolution redshift bins. Sources from the NED search also contained redshift information. For those sources, we compare the known spectroscopic redshift with our estimated photometric redshift, from the χ^2 fitting technique as shown in Fig. 4.7 and in Table 4.1. The SEDs of the 19 NED sources with redshift information are shown in Figs. 4.9 - 4.27. The redshift comparison is disappointingly poor. SEDs 10831, 13369, 19066, 30480 and 60542 yield best matches and it can be seen that their SEDs show a smooth continuum with at least 1 or 2 emission features. The SEDs that lack noticeable emission features and those with significant noise are fit quite poorly.

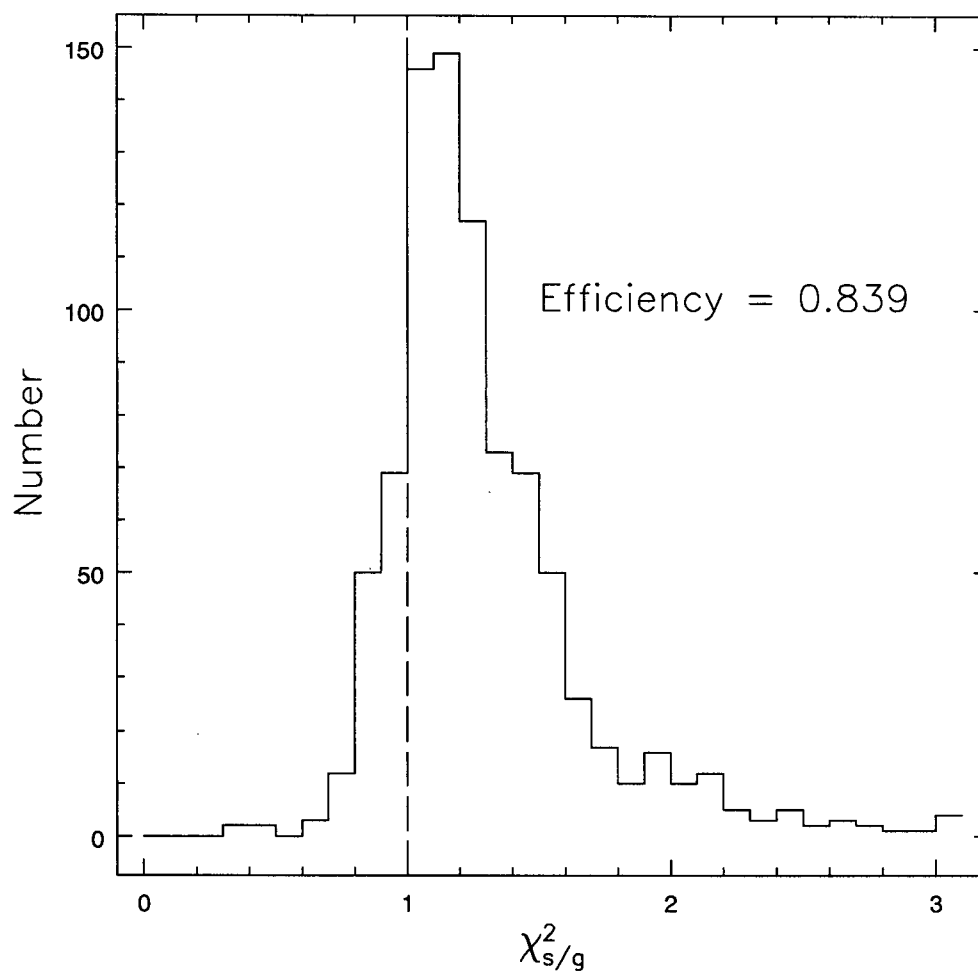


Figure 4.5 NED-confirmed galaxies plotted against their respective $\chi^2_{s/g}$ values.

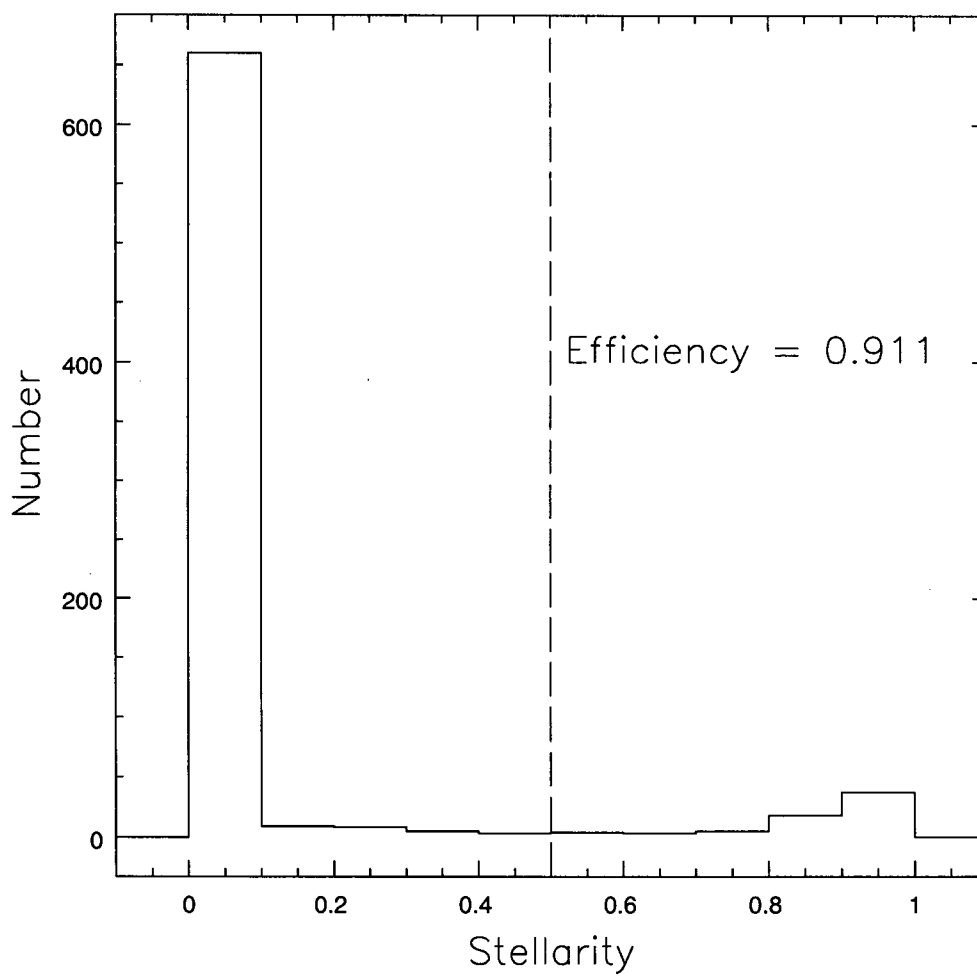


Figure 4.6 NED-confirmed galaxies plotted against their respective stellarity values.

Table 4.1. NED Sources with Redshift Information

| $N_{\text{source}}^{\text{a}}$ | $N_{\text{det}}^{\text{b}}$ | $z_{\chi^2}^{\text{c}}$ | $z_{\text{NED}}^{\text{d}}$ | Δz^{e} | Mag^{f} | χ^2^{g} |
|--------------------------------|-----------------------------|-------------------------|-----------------------------|-----------------------|-------------------------|---------------------|
| 10831 | 32 | 0.04 | 0.0371 | 0.00 | 18.2502 | 4.8 |
| 11290 | 36 | 0.35 | 0.1210 | 0.23 | 16.2780 | 9.8 |
| 11578 | 36 | 0.36 | 0.0177 | 0.34 | 14.9335 | 1171.3 |
| 13369 | 31 | 0.05 | 0.0515 | 0.00 | 18.5721 | 12.8 |
| 13511 | 38 | 0.11 | 0.1261 | 0.02 | 17.0989 | 21.9 |
| 14736 | 38 | 0.32 | 0.0357 | 0.28 | 14.4539 | 595.4 |
| 15496 | 39 | 0.06 | 0.0465 | 0.01 | 14.9432 | 250.2 |
| 19066 | 38 | 0.02 | 0.0158 | 0.00 | 16.9995 | 82.7 |
| 21916 | 38 | 0.33 | 0.0484 | 0.28 | 14.5412 | 5232.6 |
| 29298 | 27 | 0.39 | 0.4160 | 0.03 | 18.5732 | 34.6 |
| 29628 | 30 | 1.01 | 0.0143 | 1.00 | 15.3799 | 184.7 |
| 30480 | 34 | 0.04 | 0.0369 | 0.00 | 18.4308 | 13.6 |
| 31711 | 35 | 0.28 | 0.0123 | 0.27 | 16.5055 | 28.1 |
| 58428 | 36 | 0.95 | 0.0510 | 0.90 | 15.9861 | 257.8 |
| 60542 | 36 | 0.10 | 0.0970 | 0.00 | 15.9821 | 253.6 |
| 71899 | 36 | 0.09 | 0.0311 | 0.06 | 14.1542 | 238.7 |
| 90682 | 36 | 0.18 | 0.1020 | 0.08 | 15.7190 | 34.9 |

Note. — continued on next page

Table 4.1. NED Sources with Redshift Information Continued

| $N_{\text{source}}^{\text{a}}$ | $N_{\text{det}}^{\text{b}}$ | $z_{\chi^2}^{\text{c}}$ | $z_{\text{NED}}^{\text{d}}$ | Δz^{e} | Mag ^f | $\chi^{2\text{g}}$ |
|--------------------------------|-----------------------------|-------------------------|-----------------------------|-----------------------|------------------|--------------------|
| 111720 | 33 | 0.34 | 0.0757 | 0.26 | 14.7379 | 117.7 |
| 113145 | 37 | 0.18 | 0.0457 | 0.13 | 14.0371 | 1056.2 |

^aSource number

^bNumber of filters the source was detected in

^cCalculated redshift using the χ^2 routine

^dRedshift from the NED database

^eAbsolute difference between the 2 redshifts

^fR-band magnitude

^gReduced χ^2 value of the best fitting template

Fig. 4.8 shows the redshift histograms for the final catalog of galaxies. The distributions generally match those discussed in the introduction (Figs. 1.9, 1.10 and 1.11), but again our results are not robust as confirmed by the poor match with NED redshifts. The deficit of sources past a redshift of 0.5 is inconsistent with any model or previous work. The peak of our redshift distributions at ~ 0.3 does not match with data presented in Figs. 1.9, 1.10 and 1.11. The relatively equal numbers of early and late type galaxies is not observed in this data set.

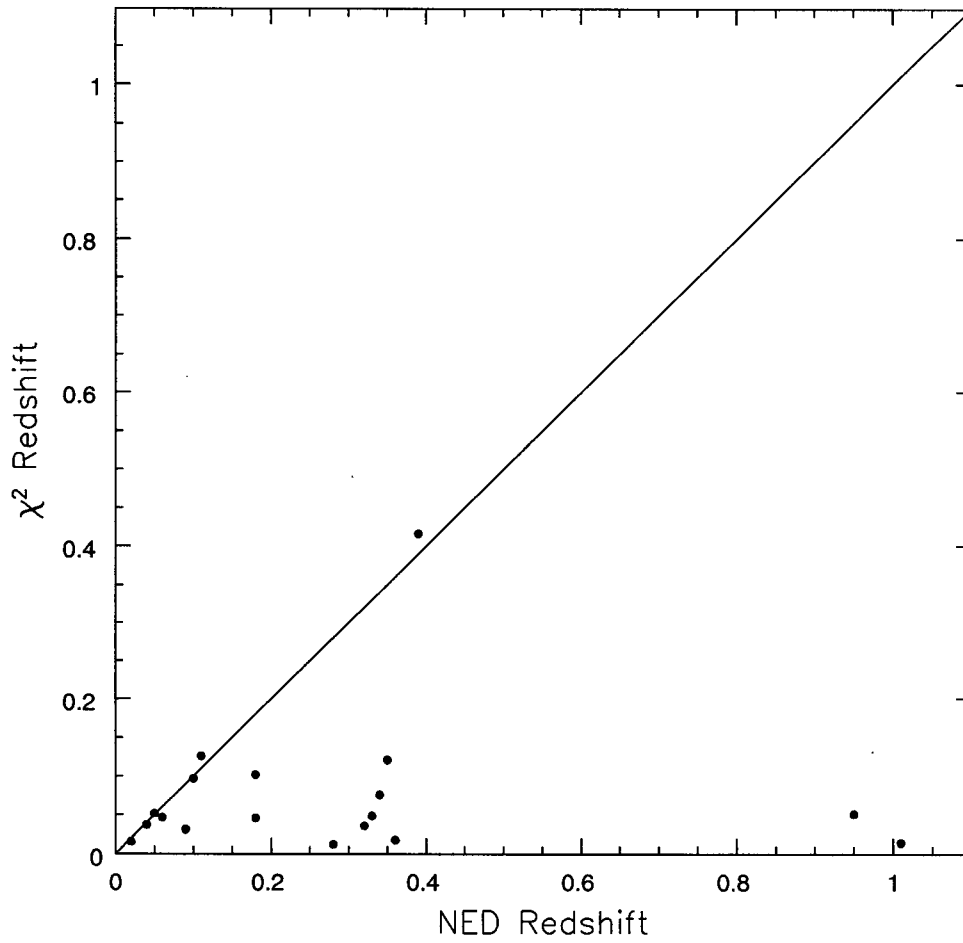


Figure 4.7 Comparison of photometrically and spectroscopically determined redshifts from our χ^2 fitting technique and NED respectively.

One future consideration is the testing of the neural network used in the SExtractor source classification. While the χ^2 fitting routine was developed and tested here, the neural network was used with fewer tests. While the weights used in the neural network were robust for data the program was tested on, the weights might not be appropriate for the type of drift-scan data used here. Producing simulated images based on the survey may help refine the neural network weights and provide a more reliable classification scheme.

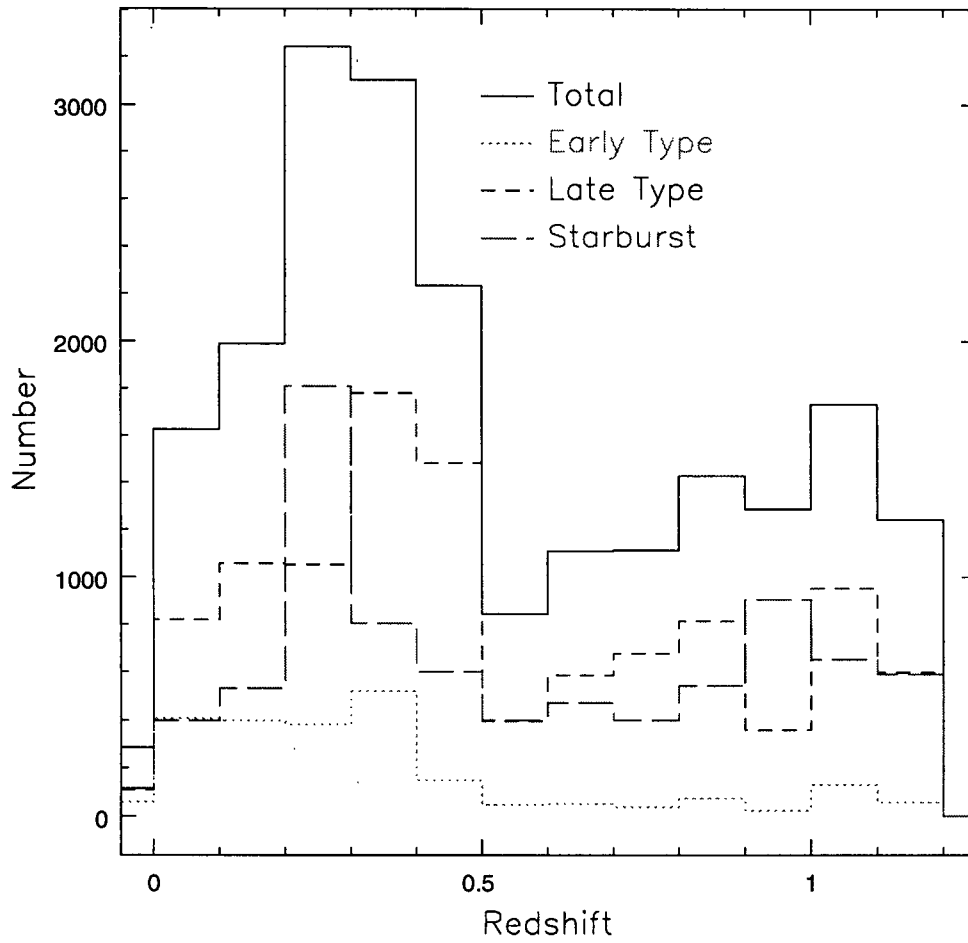


Figure 4.8 Redshift distribution of galaxies in the final catalog.

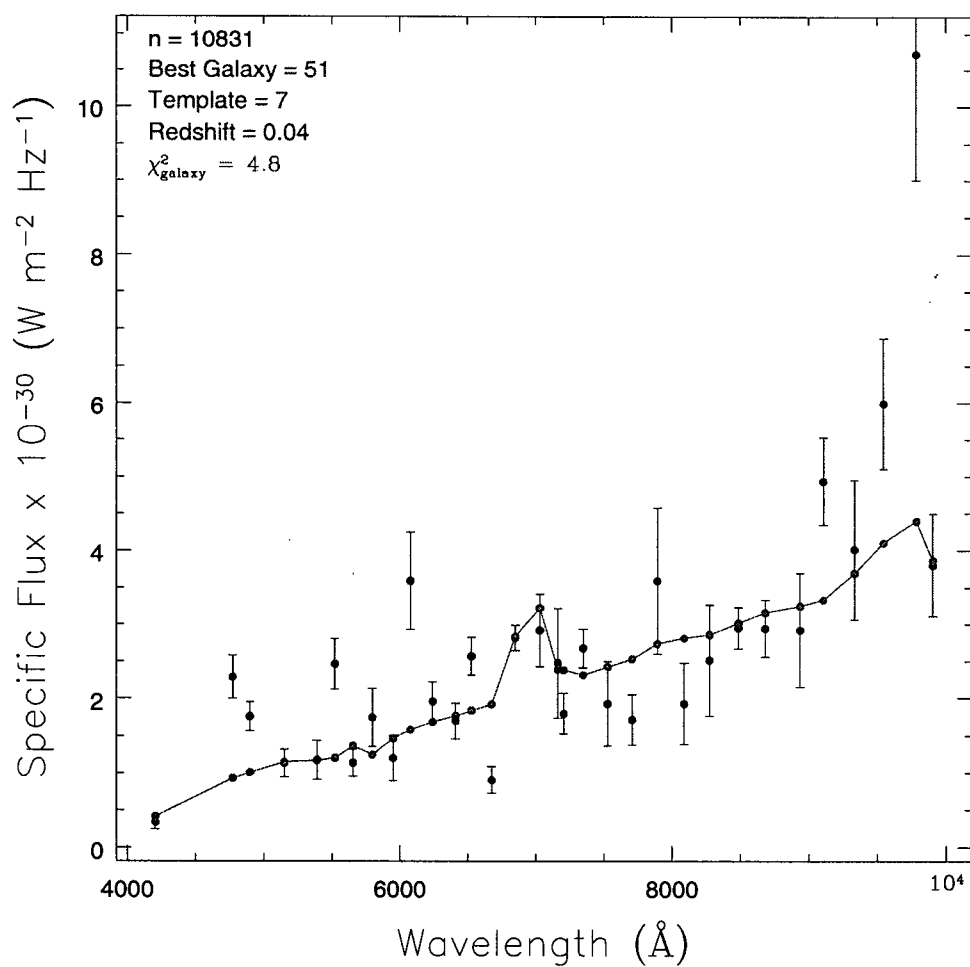


Figure 4.9 SED of NED confirmed galaxy 10831. The relatively smooth distribution of points and one spectral feature provided an accurate redshift estimate.

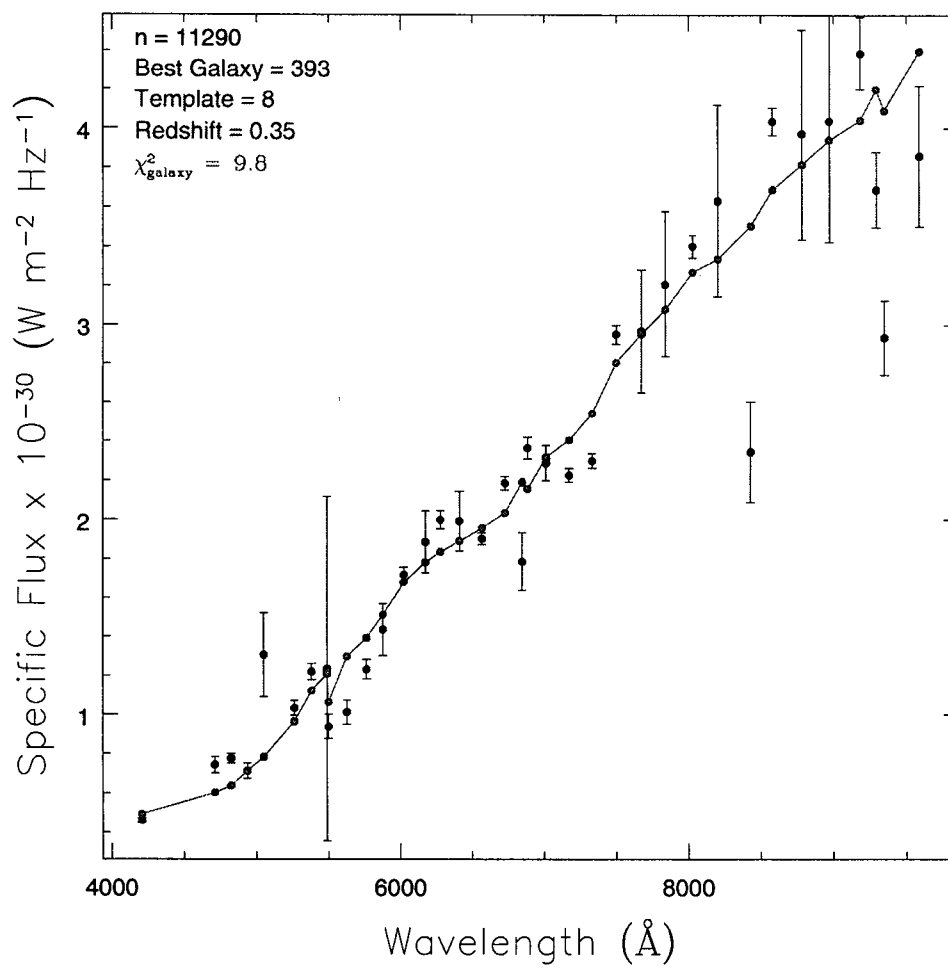


Figure 4.10 SED of NED confirmed galaxy 11290. A smooth SED, but an absence of any spectral features makes the fit difficult and results in an inconsistent fit for redshift.

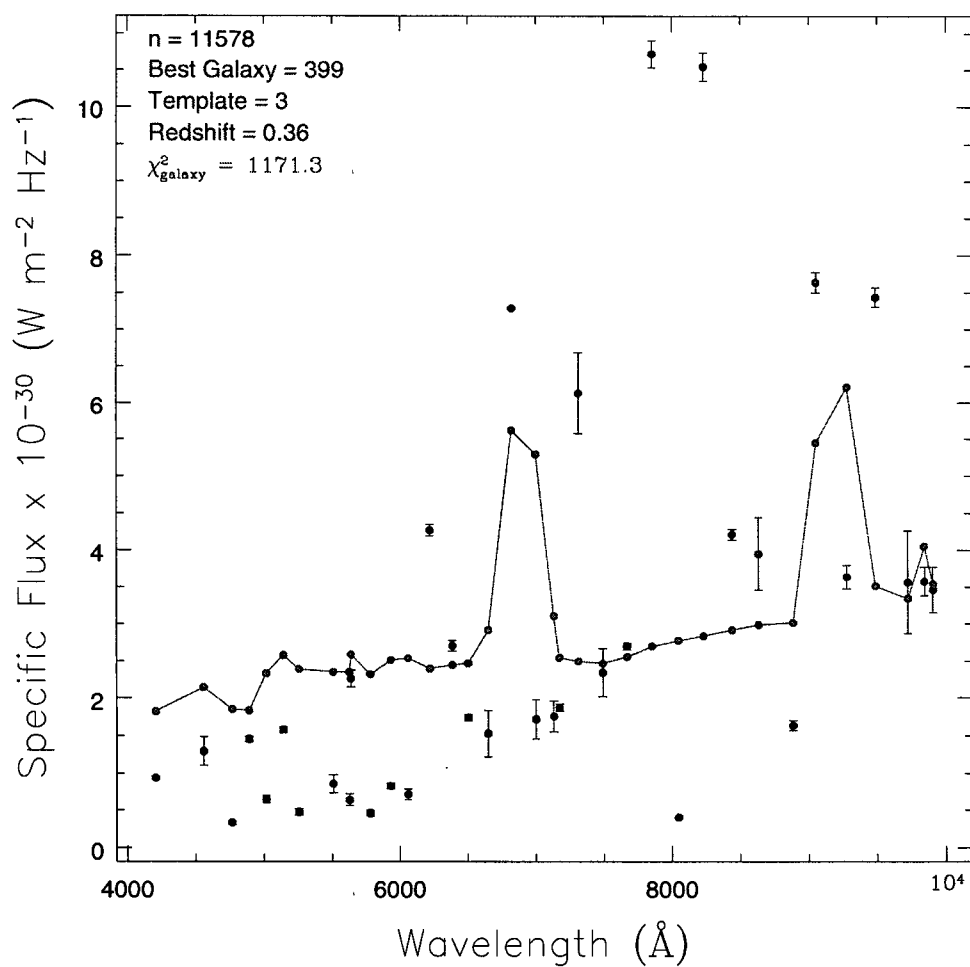


Figure 4.11 SED of NED confirmed galaxy 11578. Small error bars on very scattered points resulted in an inconsistent fit for redshift.

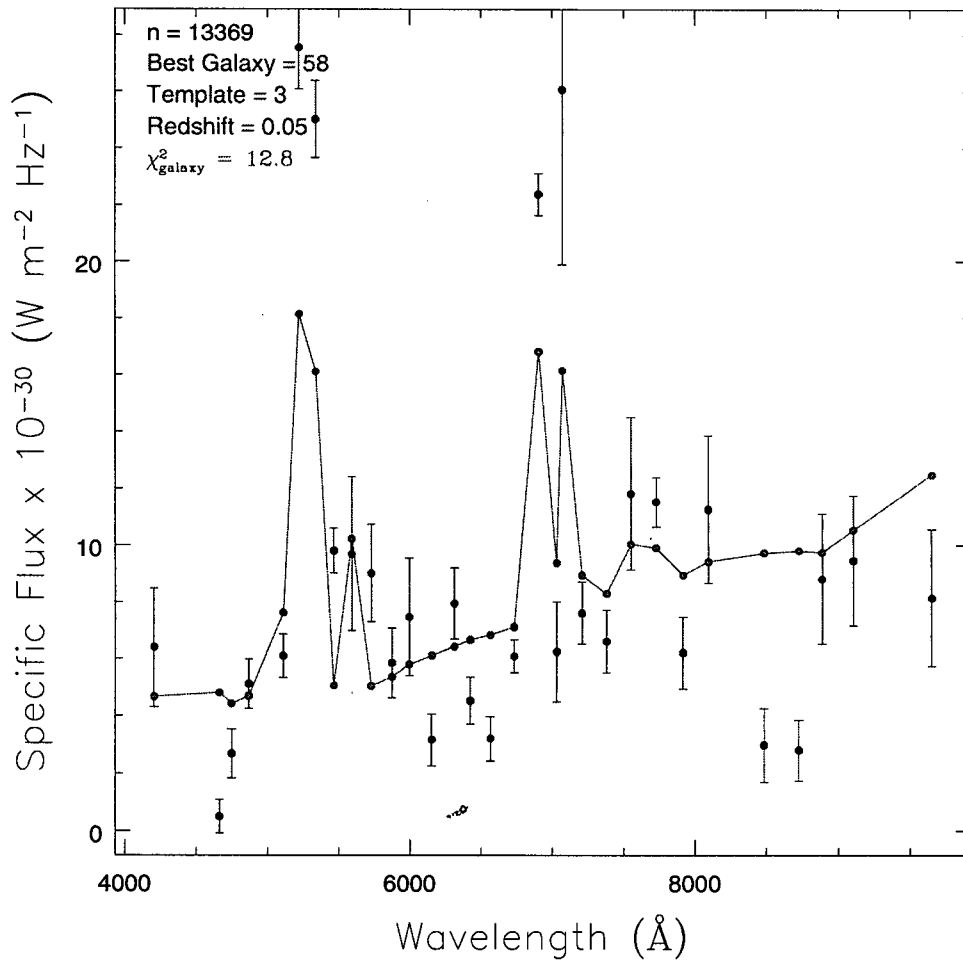


Figure 4.12 SED of NED confirmed galaxy 13369. Three strong spectral features were correctly matched and provided an accurate redshift estimate.

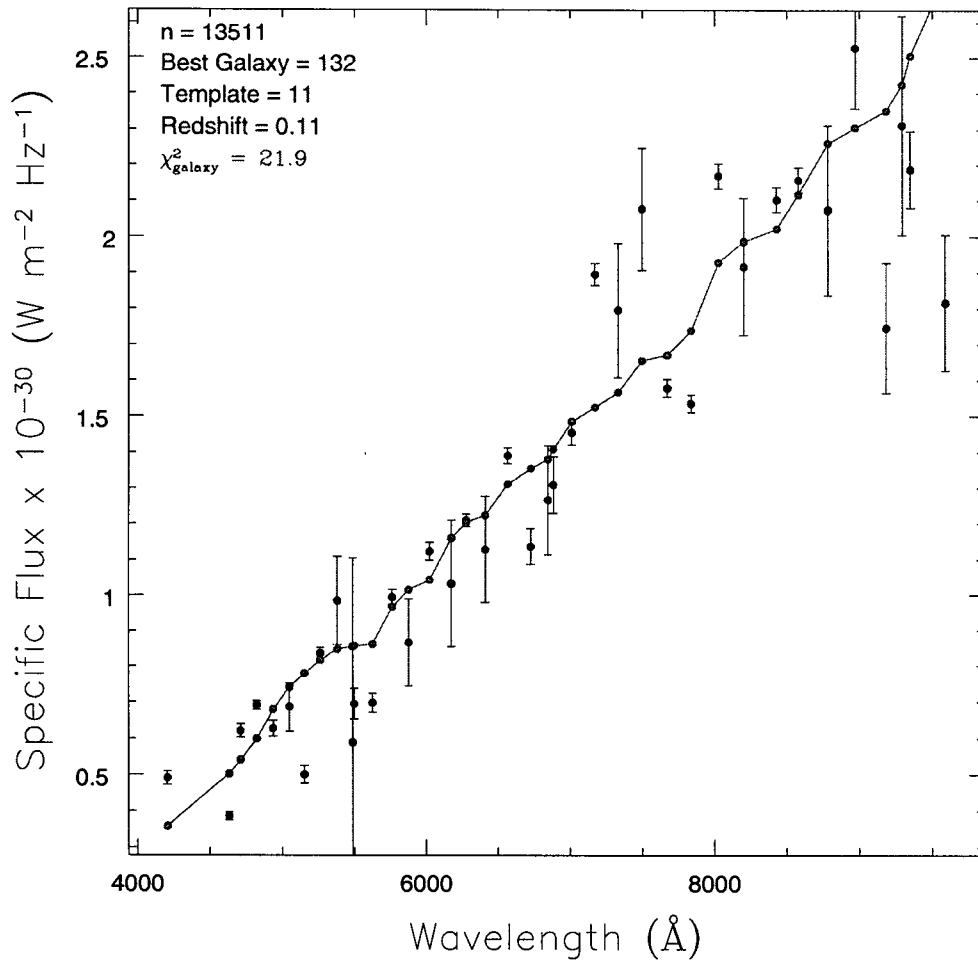


Figure 4.13 SED of NED confirmed galaxy 13511. This featureless spectrum provided a difficult fit.

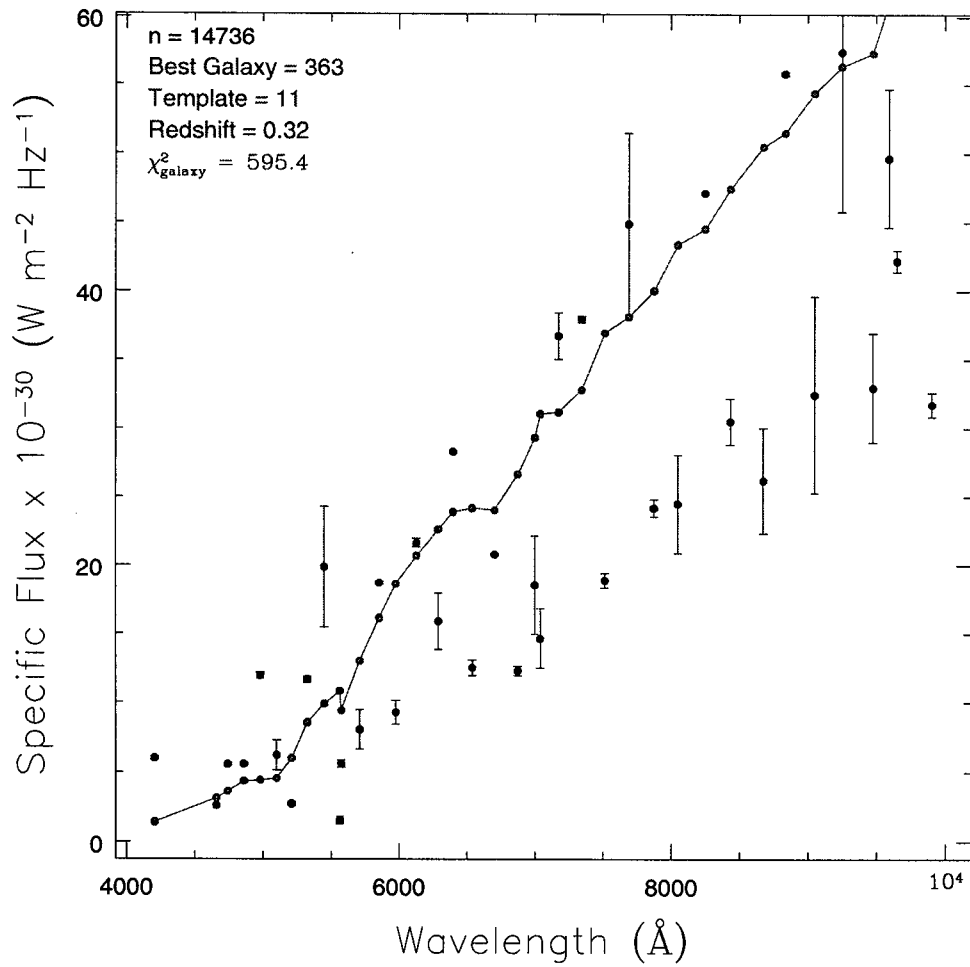


Figure 4.14 SED of NED confirmed galaxy 14736. This appears as 2 distribution of points or many spectral features making a fit difficult.

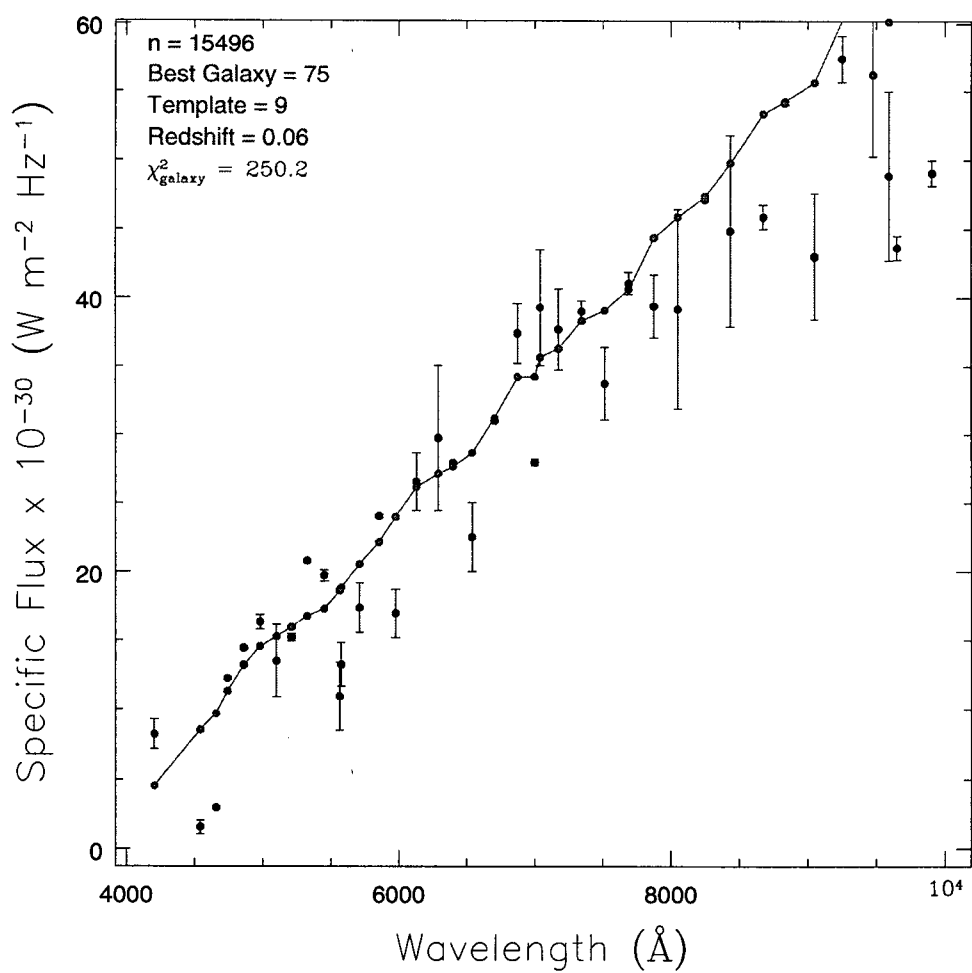


Figure 4.15 SED of NED confirmed galaxy 15496. This featureless spectrum provided a difficult fit.

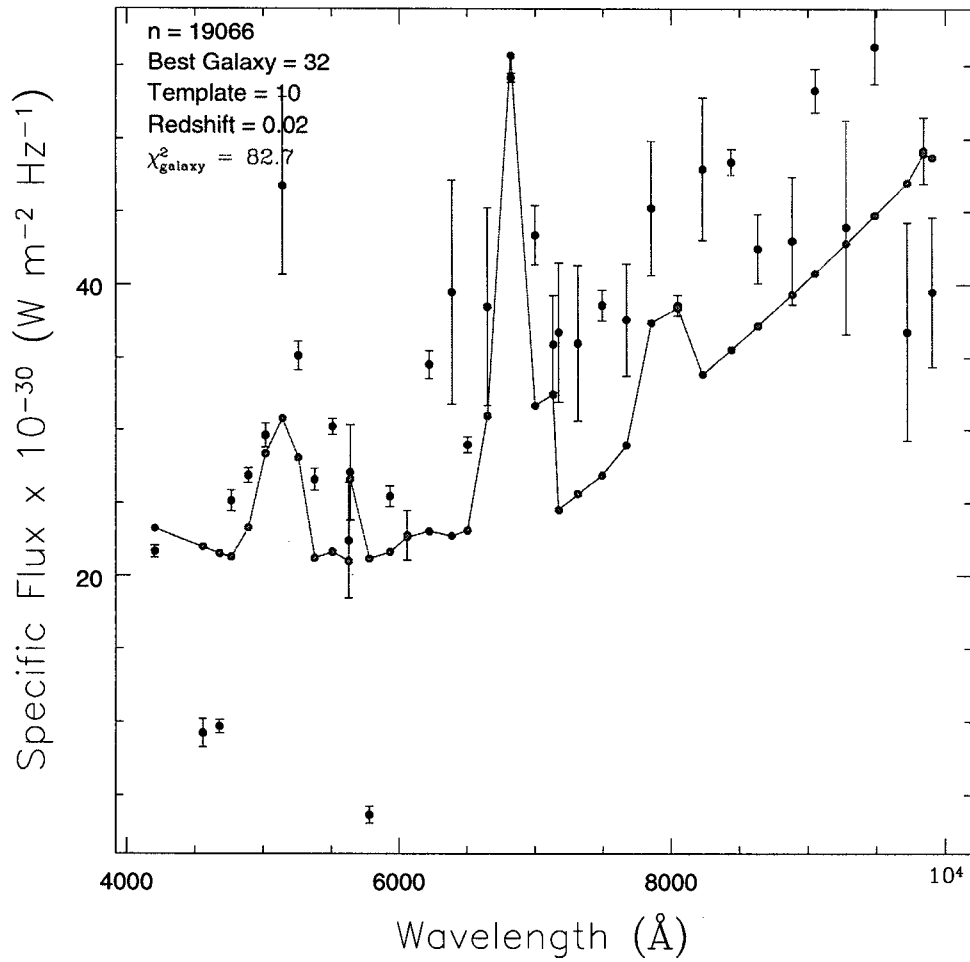


Figure 4.16 SED of NED confirmed galaxy 19066. Two well matched spectral features provide an accurate redshift estimate.

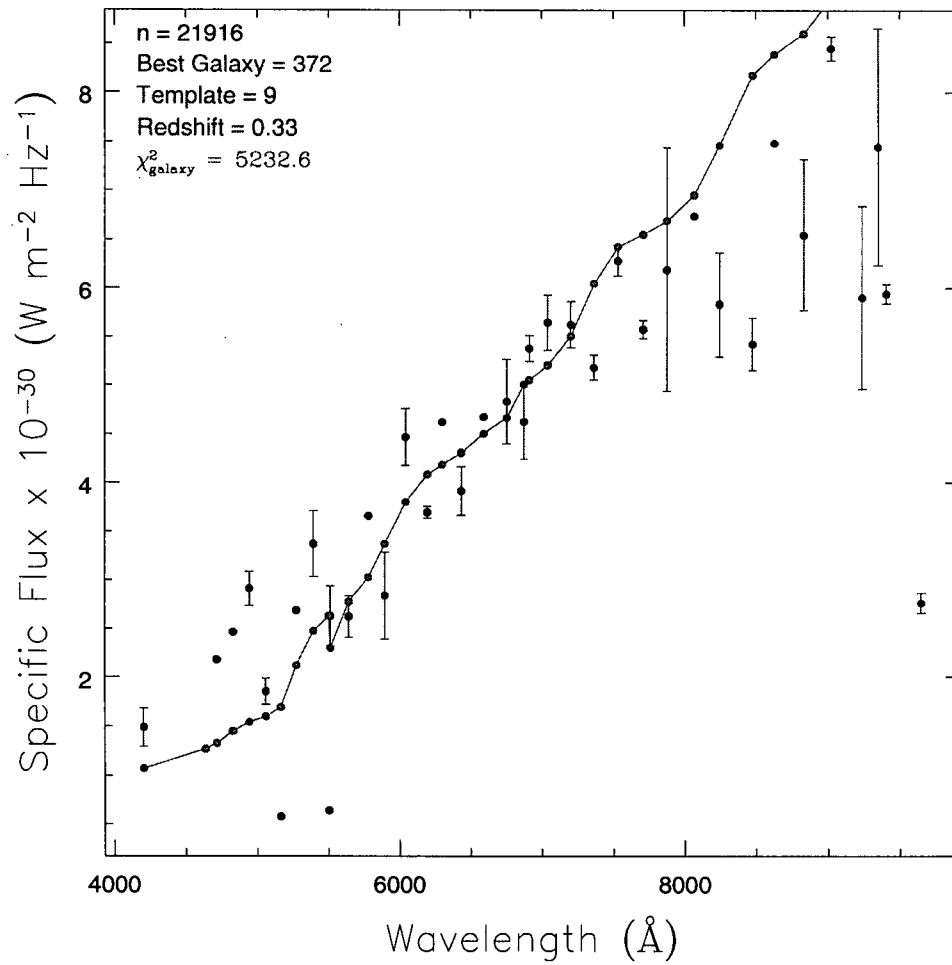


Figure 4.17 SED of NED confirmed galaxy 21916. This featureless spectrum provided a difficult fit.

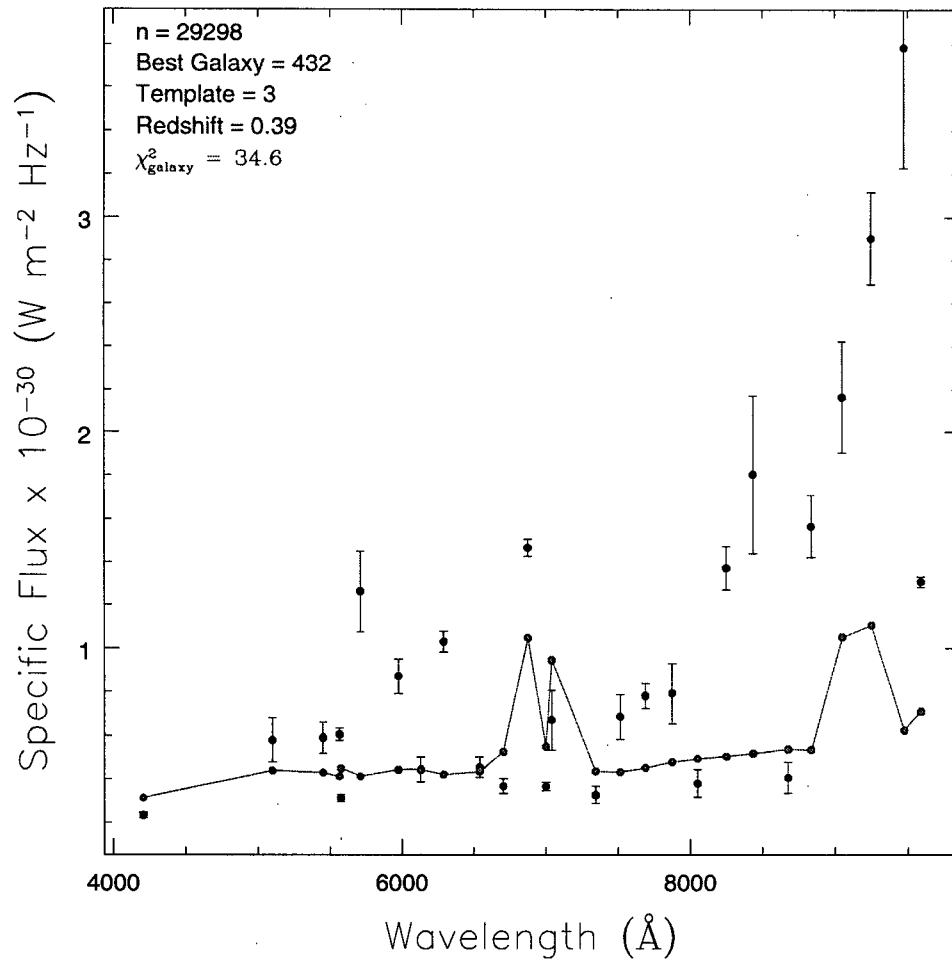


Figure 4.18 SED of NED confirmed galaxy 29298. A poorly fit spectral features due to the points with smaller error bars gave an inconsistent redshift.

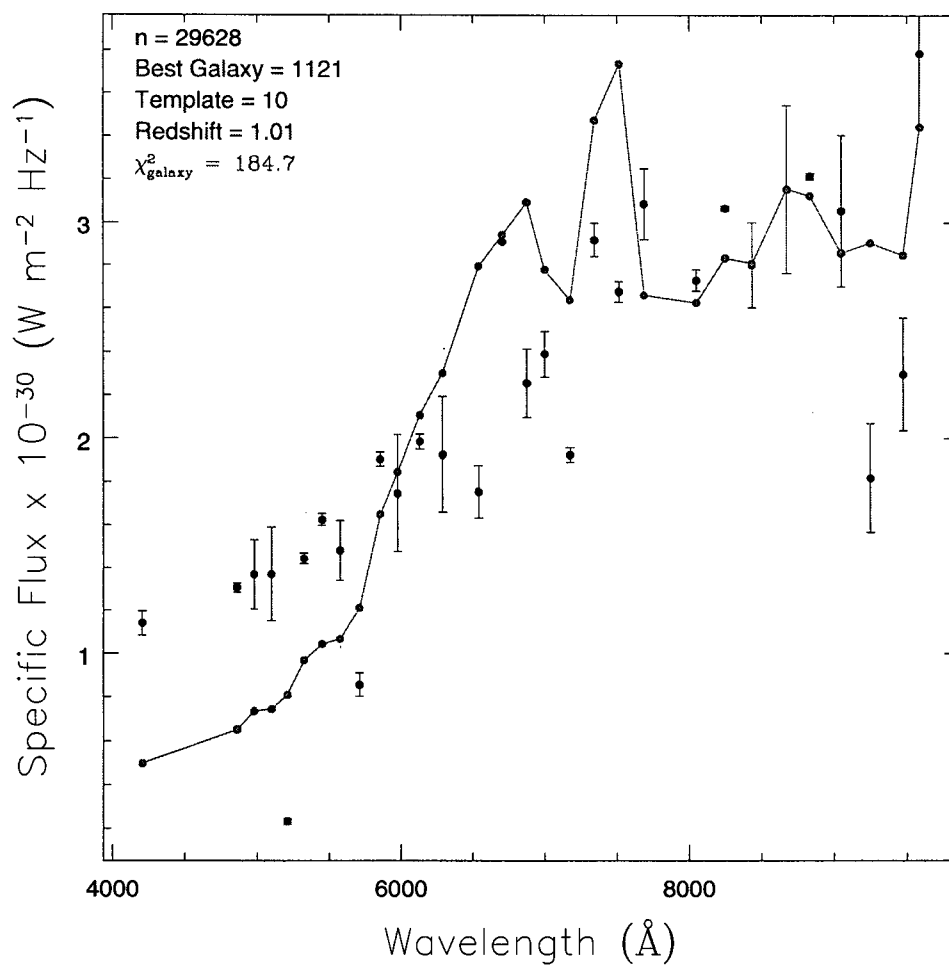


Figure 4.19 SED of NED confirmed galaxy 29628. The best fitting template did not fit well.

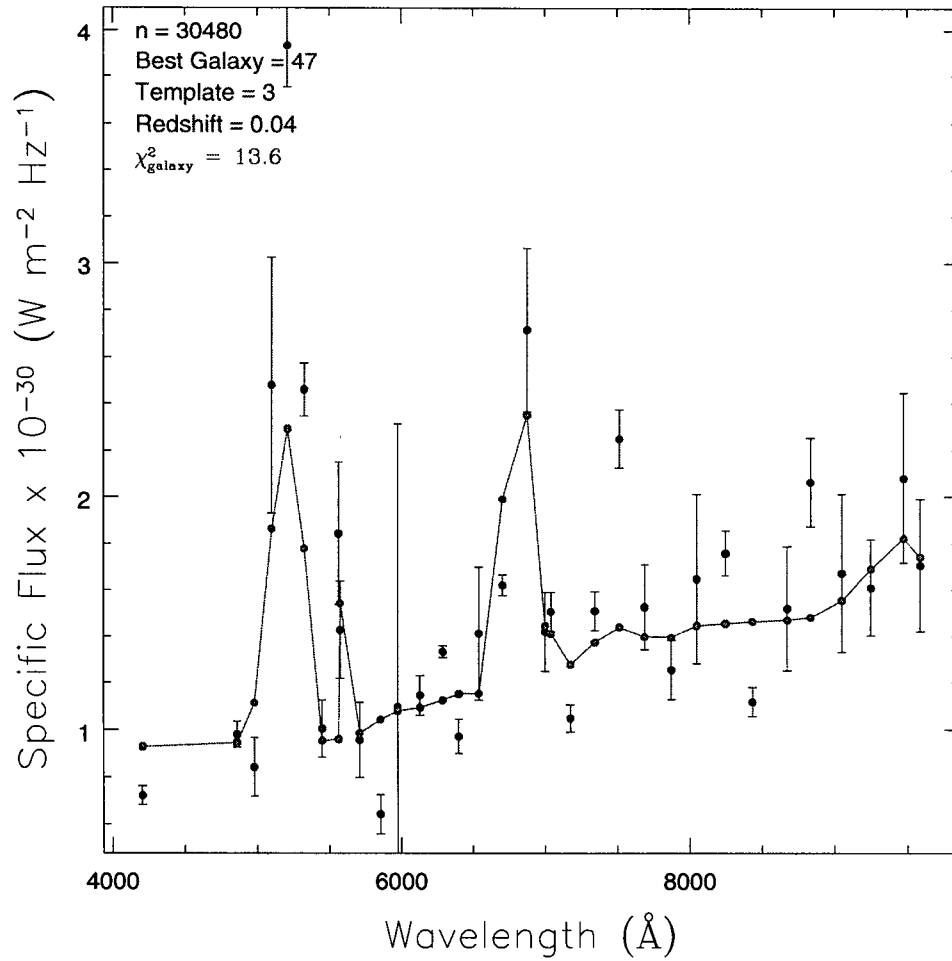


Figure 4.20 SED of NED confirmed galaxy 30480. Two well fit spectral features provided an accurate redshift estimate.

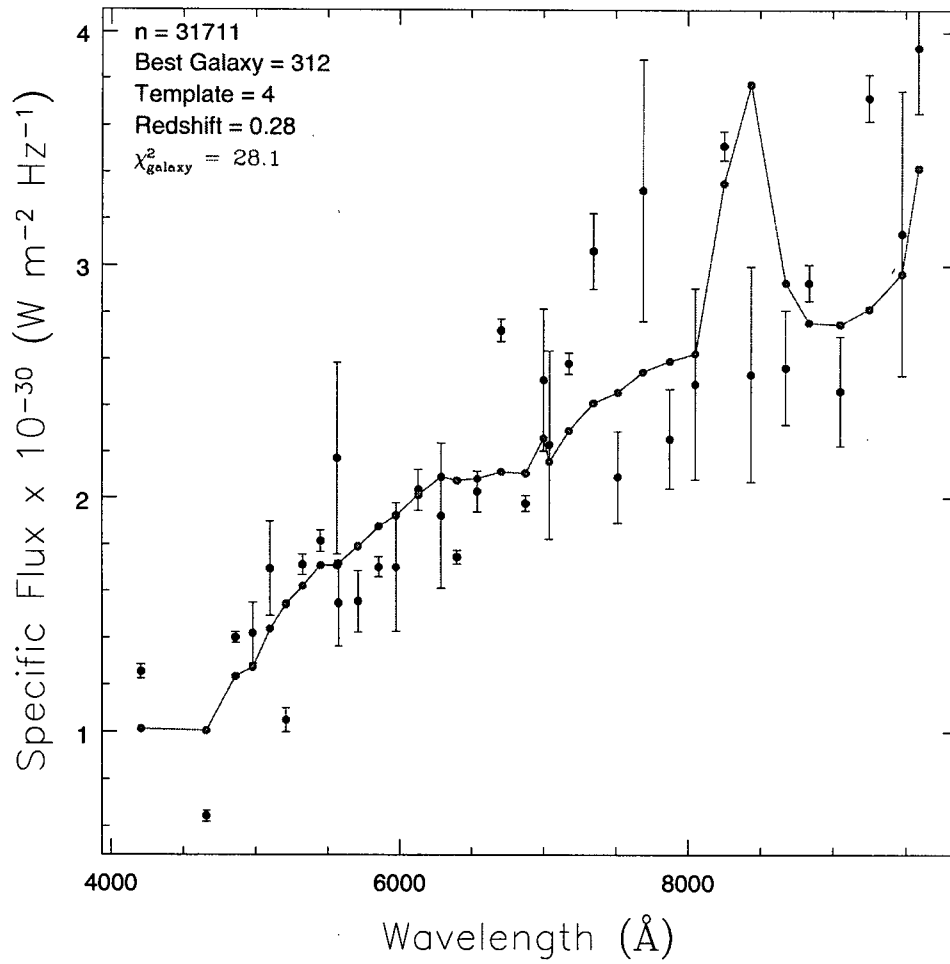


Figure 4.21 SED of NED confirmed galaxy 31711. A poorly fit spectral feature gave an inconsistent fit for redshift.

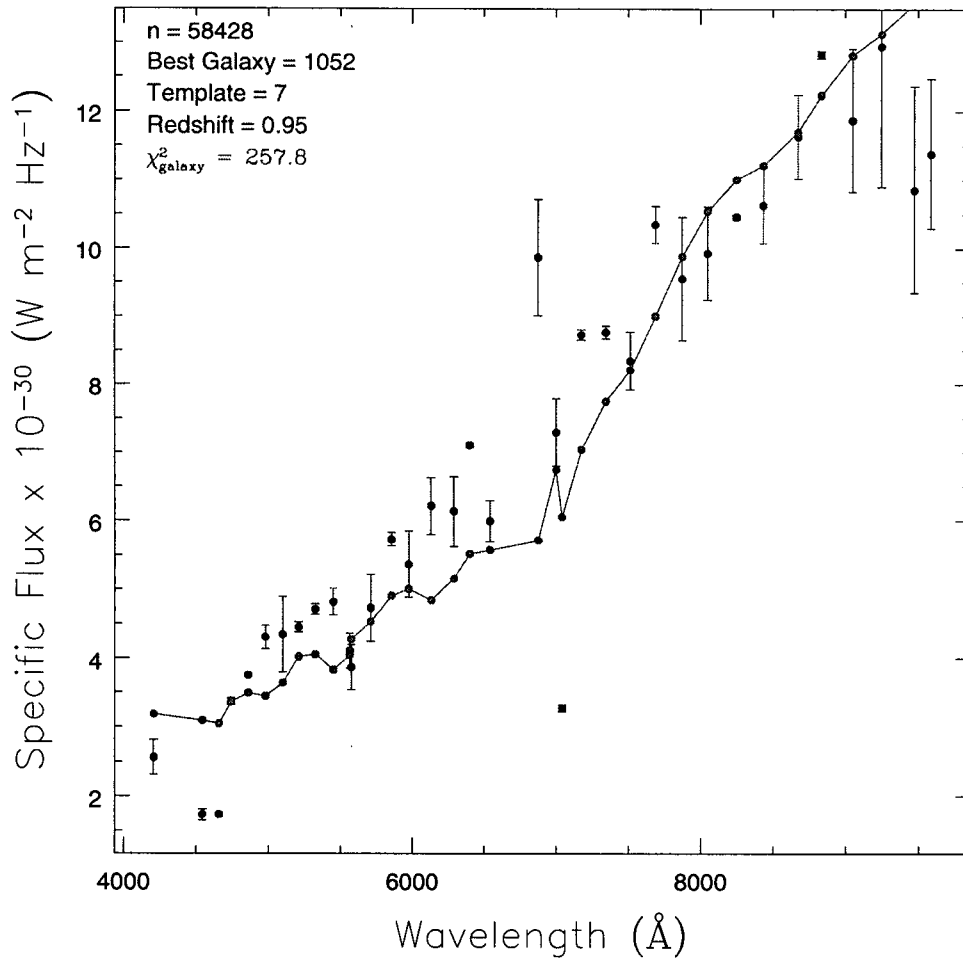


Figure 4.22 SED of NED confirmed galaxy 58428. No matching spectral features made for a difficult fit.

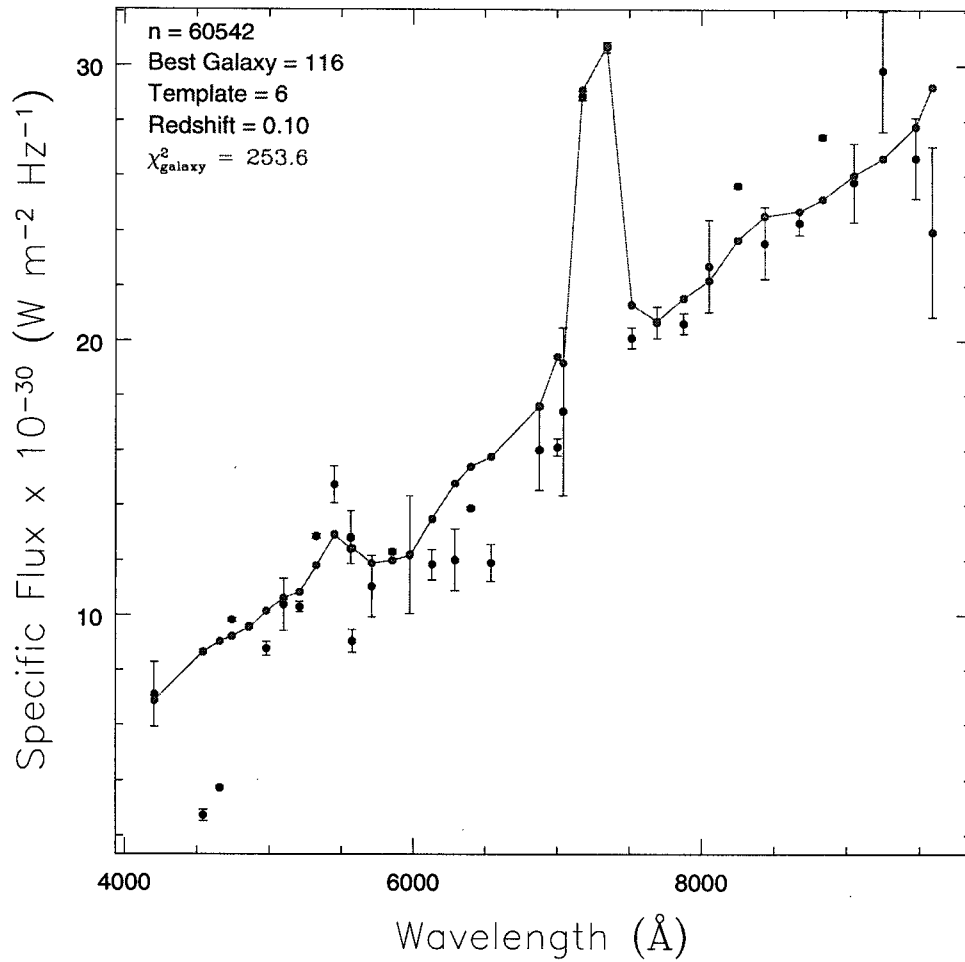


Figure 4.23 SED of NED confirmed galaxy 60542. A very well fit spectral feature gave an accurate redshift.

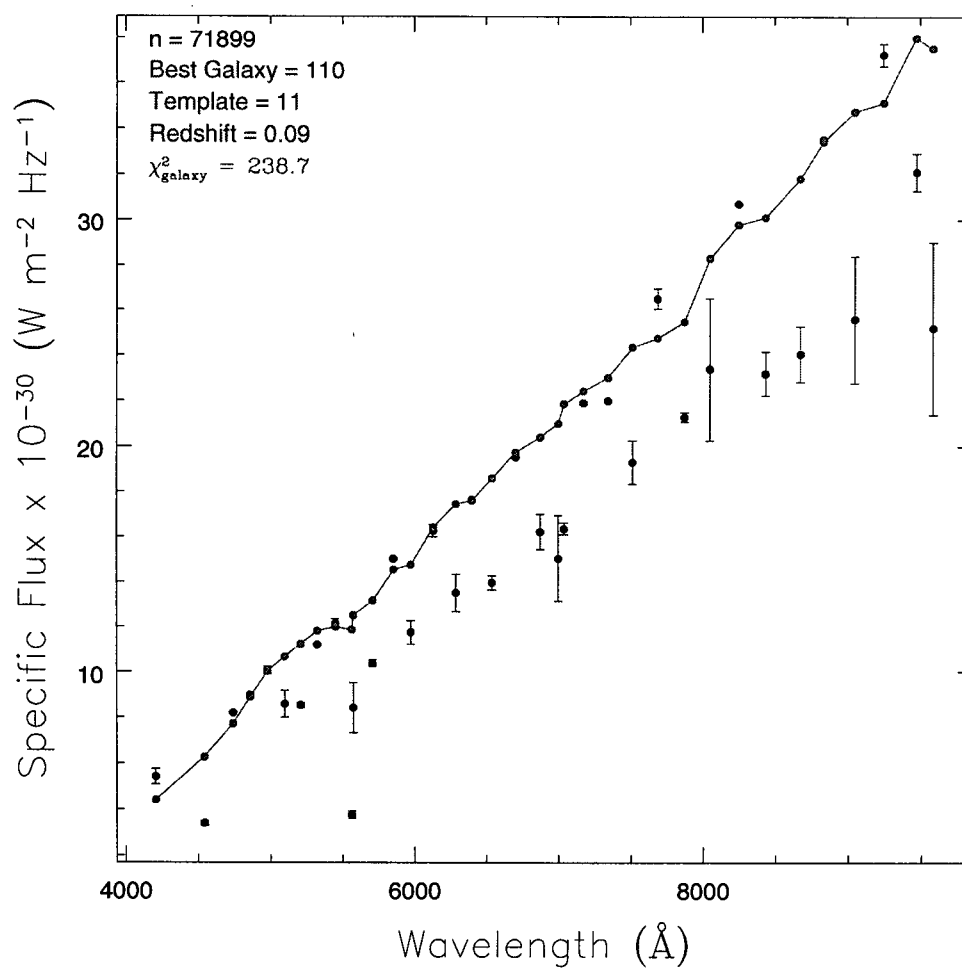


Figure 4.24 SED of NED confirmed galaxy 71899. The best fitting template did not fit well.

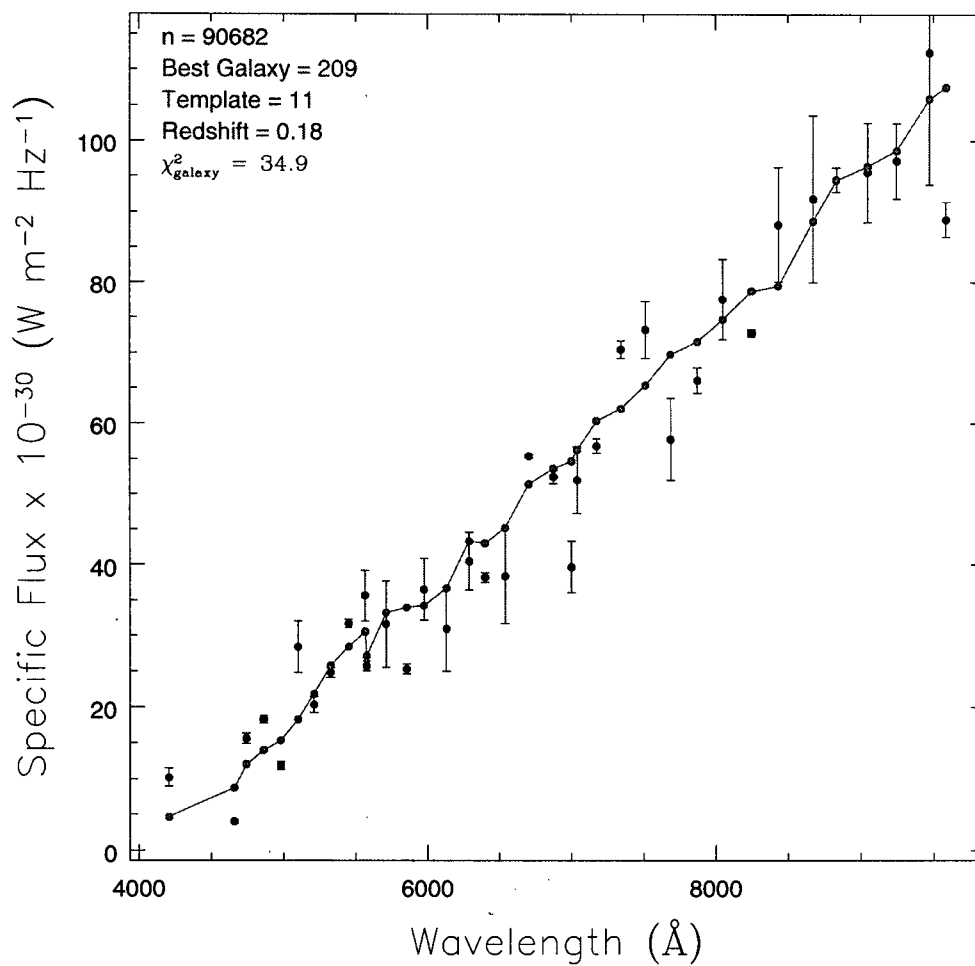


Figure 4.25 SED of NED confirmed galaxy 90682. Featureless spectrum provided a difficult fit.

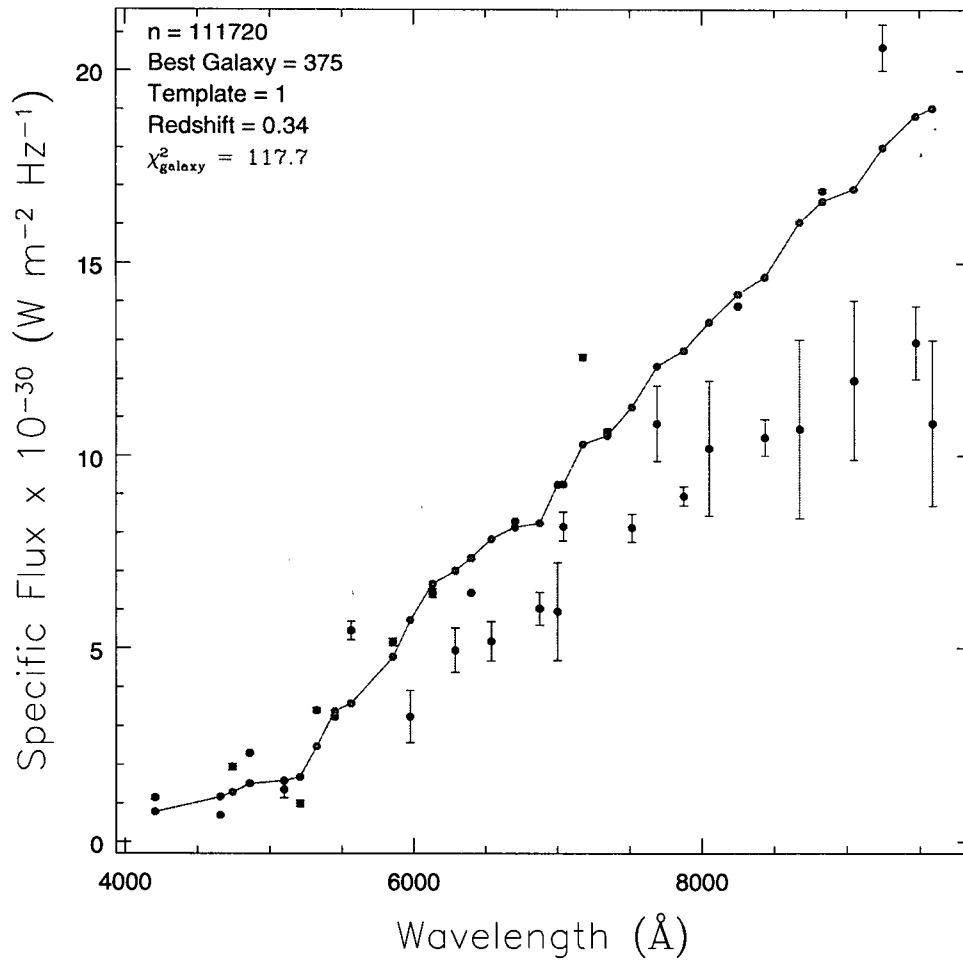


Figure 4.26 SED of NED confirmed galaxy 111720. Best fitting template did not fit well.

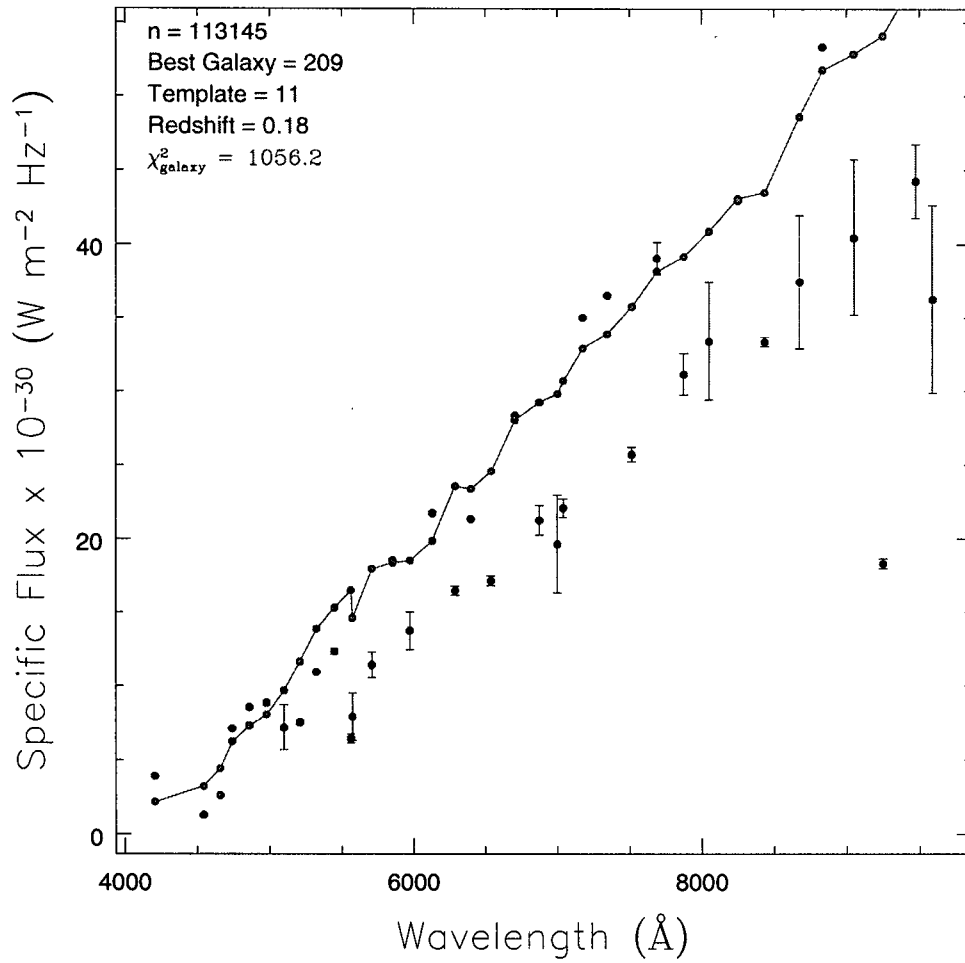


Figure 4.27 SED of NED confirmed galaxy 113145. Best fitting template did not fit well.

Chapter 5

Conclusions and Future Work

This thesis investigated the classification of sources and in particular the identification of galaxies in drift-scan data. Galaxies were classified into Hubble type and redshift bins with the goal of deriving a redshift distribution of galaxies in the survey.

The data examined here are unique in that a maximum of 39 bands of information can be available for any source in the area of observation. In principle, especially for faint object searches, the drift-scan mode of observation allows faint objects to be more easily detected as CCD non-uniformities are reduced. While this is the case for drift-scan observations, the CCD used to obtain the narrowband photometric information was optimized for quick read out and hence suffered from high noise.

Two independent classification schemes were implemented and compared. One used the photometric information from all the filters available (χ^2 fitting routine) and the other based the classification on a neural network with isophotal shape parameters as inputs (SExtractor). Since the index for the χ^2 fitting routine is a ratio of the χ^2 value of the best fitting stellar template to the χ^2 value of the best fitting galaxy template, the distribution of sources in this parameter space is concentrated around 1. This concentration could also be due to the degeneracy of certain templates and the ability of the uncertainties in the photometry to break the degeneracies. The bimodal distribution of sources is clearer with SExtractor's stellarity index, which is based upon a robust neural network. The classification efficiency of galaxies based on NASA/IPAC Extra-galactic Database-confirmed galaxies were 80% and 90% for the

χ^2 routine and stellarity index respectively, even though the comparison between the two methods was poor.

The fitted photometric redshifts were compared with spectroscopically-determined redshifts from NED. This resulted in tight matches for only a few galaxies, while roughly half of those sources had redshifts that did not agree at all. The SEDs of the galaxies with matching redshifts are smooth with at least 1 or 2 emission features. The discrepant galaxies had noisy, featureless SEDs. Based on the poor redshift comparison, more detailed analyses, such as luminosity functions, were not carried out.

Fig. 4.8 shows the redshift histograms for the final catalog of galaxies. The deficit of sources past redshift 0.5 is inconsistent with any model or previous work. The redshift distributions peak at ~ 0.3 whereas in other surveys (see Figs. 1.6, 1.7 and 1.8) the peak occurs at ~ 0.45 . The relatively equal numbers of early and late type galaxies is also not observed in our data set. The inconsistencies in redshift estimates are due to the poor template fits.

Future data with better S/N from the UBC 6-m Large Zenith Telescope (LZT) may help to resolve these issues. The LZT will be able probe galaxies to fainter magnitudes and greater depth and produce photometric data with greatly reduced noise. Methods used in this work can be then applied in much the same way to future data sets obtained with the LZT. In addition, the principal component analysis of Cabanac et al. [10] can help with determining accurate photometric redshifts, galaxy luminosity functions and distributions of stars and QSOs.

Bibliography

- [1] E. Bertin and S. Arnouts. SExtractor: Software for source extraction. *A&AS*, 117:393–404, June 1996.
- [2] B. Binggeli, A. Sandage, and G. A. Tammann. The luminosity function of galaxies. *ARA&A*, 26:509–560, 1988.
- [3] B. Binggeli, M. Tarenghi, and A. Sandage. The abundance and morphological segregation of dwarf galaxies in the field. *A&A*, 228:42–60, February 1990.
- [4] M. R. Blanton et al. The Luminosity Function of Galaxies in SDSS Commissioning Data. *AJ*, 121:2358–2380, May 2001.
- [5] E. F. Borra. The liquid-mirror telescope as a viable astronomical tool. *JRASC*, 76:245–256, August 1982.
- [6] E. F. Borra, R. Content, L. Girard, S. Szapiel, L. M. Tremblay, and E. Boily. Liquid mirrors - Optical shop tests and contributions to the technology. *ApJ*, 393:829–847, July 1992.
- [7] E. F. Borra and A. R. Ritcey. Tilttable liquid mirror telescopes. In *Proc. SPIE Vol. 4003, p. 331-336, Optical Design, Materials, Fabrication, and Maintenance, Philippe Dierickx; Ed.*, volume 4003, pages 331–336, July 2000.

-
- [8] G. D. Bothun, C. D. Impey, and D. F. Malin. Extremely low surface brightness galaxies in the Fornax Cluster - Properties, stability, and luminosity fluctuations. *ApJ*, 376:404–423, August 1991.
- [9] B. C. Bromley, W. H. Press, H. Lin, and R. P. Kirshner. Spectral Classification and Luminosity Function of Galaxies in the Las Campanas Redshift Survey. *ApJ*, 505:25–36, September 1998.
- [10] R. A. Cabanac, V. de Lapparent, and P. Hickson. Classification and redshift estimation by principal component analysis. *A&A*, 389:1090–1116, July 2002.
- [11] G. D. Coleman, C.-C. Wu, and D. W. Weedman. Colors and magnitudes predicted for high redshift galaxies. *ApJS*, 43:393–416, July 1980.
- [12] J. J. Dalcanton, D. N. Spergel, J. E. Gunn, M. Schmidt, and D. P. Schneider. The Number Density of Low-Surface Brightness Galaxies with $23 < \mu_0 < 25$ V Mag/arcsec². *AJ*, 114:635–654, August 1997.
- [13] J. I. Davies, S. Phillipps, M. G. M. Cawson, M. J. Disney, and E. J. Kibblewhite. Low surface brightness galaxies in the Fornax Cluster - Automated galaxy surface photometry. III. *MNRAS*, 232:239–258, May 1988.
- [14] Andrew E. Firth, Ofer Lahav, and Rachel S. Somerville. Estimating photometric redshifts with artificial neural networks. 2002.
- [15] B. K. Gibson and P. Hickson. Time-delay integration CCD read-out technique - Image deformation. *MNRAS*, 258:543–551, October 1992.
- [16] B.K. Gibson. An experimental 2.7-metre liquid mirror telescope. Master's thesis, University of British Columbia, 1990.

-
- [17] L. Girard and E. F. Borra. Optical tests of a 2.5-m-diameter liquid mirror: behavior under external perturbations and scattered-light measurements. *Appl. Opt.*, 36:6278–6288, September 1997.
- [18] P. Hall and C. D. Mackay. Faint galaxy number-magnitude counts at high galactic latitude. I. *MNRAS*, 210:979–992, October 1984.
- [19] P. Hickson, E. F. Borra, R. Cabanac, R. Content, B. K. Gibson, and G. A. H. Walker. UBC/Laval 2.7 meter liquid mirror telescope. *ApJ*, 436:L201–LL204, December 1994.
- [20] P. Hickson and M. K. Mulrooney. A Series of Faint Spectrophotometric Standard Stars at +33 deg Declination. *ApJ*, 506:191–204, October 1998.
- [21] P. Hickson and M. K. Mulrooney. University of British Columbia-NASA Multi-Narrowband Survey. I. Description and Photometric Properties of the Survey. *ApJS*, 115:35–+, March 1998.
- [22] C. D. Impey, D. Sprayberry, M. J. Irwin, and G. D. Bothun. Low Surface Brightness Galaxies in the Local Universe. I. The Catalog. *ApJS*, 105:209–+, August 1996.
- [23] J. F. Jarvis and J. A. Tyson. FOCAS - Faint Object Classification and Analysis System. *AJ*, 86:476–495, March 1981.
- [24] H. Jenkner, B. M. Lasker, C. R. Sturch, B. J. McLean, M. M. Shara, and J. L. Russel. The Guide Star Catalog. III - Production, database organization, and population statistics. *AJ*, 99:2082–2154, June 1990.

-
- [25] A. L. Kinney, D. Calzetti, R. C. Bohlin, K. McQuade, T. Storchi-Bergmann, and H. R. Schmitt. Template Ultraviolet to Near-Infrared Spectra of Star-forming Galaxies and Their Application to K-Corrections. *ApJ*, 467:38–+, August 1996.
- [26] D. C. Koo and R. G. Kron. Evidence for evolution in faint field galaxy samples. *ARA&A*, 30:613–652, 1992.
- [27] B. M. Lasker, C. R. Sturch, B. J. McLean, J. L. Russell, H. Jenkner, and M. M. Shara. The Guide Star Catalog. I - Astronomical foundations and image processing. *AJ*, 99:2019–2058, June 1990.
- [28] S. J. Lilly, O. Le Fevre, D. Crampton, F. Hammer, and L. Tresse. The Canada-France Redshift Survey. I. Introduction to the Survey, Photometric Catalogs, and Surface Brightness Selection Effects. *ApJ*, 455:50–+, December 1995.
- [29] H. Lin, H. K. C. Yee, R. G. Carlberg, S. L. Morris, M. Sawicki, D. R. Patton, G. Wirth, and C. W. Shepherd. The CNOC2 Field Galaxy Luminosity Function. I. A Description of Luminosity Function Evolution. *ApJ*, 518:533–561, June 1999.
- [30] J. Loveday, B. A. Peterson, G. Efstathiou, and S. J. Maddox. The Stromlo-APM Redshift Survey. I - The luminosity function and space density of galaxies. *ApJ*, 390:338–344, May 1992.
- [31] J. T. McGraw, J. R. P. Angel, and T. A. Sargent. A charge-coupled device transit-telescope survey for galactic and extragalactic variability and polarization. In *Conference on Applications of Digital Image Processing to Astronomy, Pasadena, Calif., August 20-22, 1980, Proceedings. (A81-25962 10-35) Bellingham, Wash.*

-
- Society of Photo-Optical Instrumentation Engineers, 1980, p. 20-28.*, volume 264, pages 20–22, 1980.
- [32] M. Mulrooney. *A 3.0 meter Liquid Mirror Telescope*. PhD thesis, Rice University, 2000.
- [33] H. J. Newberg, G. T. Richards, M. Richmond, and X. Fan. Catalog of Four-Color Photometry of Stars, Galaxies, and QSOS Using SDSS Filters. *ApJS*, 123:377–435, August 1999.
- [34] N. M. Ninane and C. A. Jamar. Parabolic liquid mirrors in optical shop testing. *Appl. Opt.*, 35:6131–6139, November 1996.
- [35] S. C. Odewahn, R. M. Humphreys, G. Aldering, and P. Thurmes. Star-galaxy separation with a neural network. 2: Multiple Schmidt plate fields. *PASP*, 105:1354–1365, November 1993.
- [36] J. B. Oke. Absolute Spectral Energy Distributions for White Dwarfs. *ApJS*, 27:21–+, February 1974.
- [37] A. J. Pickles. A Stellar Spectral Flux Library: 1150-25000 Å. *PASP*, 110:863–878, July 1998.
- [38] M. Postman, L. M. Lubin, J. E. Gunn, J. B. Oke, J. G. Hoessel, D. P. Schneider, and J. A. Christensen. The Palomar Distant Clusters Survey. I. The Cluster Catalog. *AJ*, 111:615–+, February 1996.
- [39] J. L. Russell, B. M. Lasker, B. J. McLean, C. R. Sturch, and H. Jenkner. The Guide Star Catalog. II - Photometric and astrometric models and solutions. *AJ*, 99:2059–2081, June 1990.

-
- [40] P. Schechter. An analytic expression for the luminosity function for galaxies. *ApJ*, 203:297–306, January 1976.
- [41] H. Skey. *Trans. New Zealand Inst.*, 5:119, 1872.
- [42] D. Sprayberry, C. D. Impey, M. J. Irwin, and G. D. Bothun. Low Surface Brightness Galaxies in the Local Universe. III. Implications for the Field Galaxy Luminosity Function. *ApJ*, 482:104–+, June 1997.
- [43] R. W. Wood. The Mercury Paraboloid as a Reflecting Telescope. *ApJ*, 29:164–+, March 1909.